EVALUATION OF SPECIALTY FIBERS AND WAVEGUIDES FOR ULTRASHORT LASER PULSE PROPAGATION

By

MICHAEL N. NGUYEN

Bachelor of Science in Electrical Engineering

Oklahoma State University

Stillwater, OK

2000

Submitted to the Faculty of the
Graduate College of the
Oklahoma State University
in partial fulfillment of
the requirements for
the Degree of
DOCTOR OF PHILOSOPHY
May, 2008

EVALUATION OF SPECIALTY FIBERS AND

WAVEGUIDES FOR ULTRASHORT LASER PULSE

PROPAGATION

Dissertation Approved:

Kenneth H. Church

Dissertation Adviser

R. Alan Cheville

Paul A. Westhaus

James P. Wicksted

A. Gordon Emslie

Dean of the Graduate College

Acknowledgements

First and foremost, I would like to thank my advisor, Dr. Kenneth Church, for encouraging me to pursue my Ph.D. This dissertation would not have been completed were it not for his tireless efforts to acquire projects and funding. I am eternally grateful for the opportunity to work with him and the first-rate staff at Scipeiro on the many diverse projects over the years. It turned out to be a long road, but his support and guidance kept me on track.

To my committee members, Dr. Alan Cheville, Dr. James Wicksted and Dr. Paul Westhaus, I would like to thank you all for your valuable time, suggestions and advice. The discussion with Dr. Cheville on building the interferometric autocorrelator was especially helpful.

I would like to thank Dr. Vladimir Pelekhaty for the many long discussions and unique insight only he can provide. I would also like to thank everyone at VaxDesign for their support and friendship. I am especially grateful to Dr. William Warren for granting me the opportunity to conduct my research at his facilities and to Dr. Robert Parkhill for taking a genuine interest in my research and always making sure I had everything needed to complete the work.

I would like to thank my mom for teaching me the value of hard work, persistence and patience and my dad for teaching me to make the most of what is given and to find utility in even the smallest of things. I am also grateful to my grandparents and friends

and family for all of their support through the years.

Last, but certainly not least, I would like to dedicate this dissertation to my wife, Megan and my son, William, for enduring the long days, longer nights and even longer weekends when I was away in the lab.

Table of Contents

Chapter Page

Chapter **Page**

List of Symbols

3-D	three dimensional
B_j	oscillator strength
c	speed of light in vacuum, 3×10^8 m/s
COP	cyclic olefin polymer
CW	continuous wave
D	dispersion parameter
E	electric field, V/m
f	focal length, m
FIR	far infrared
GVD	group velocity dispersion
HAZ	heat affected zone
j	unit imaginary number, $\sqrt{-1}$
k	wavevector amplitude (wavenumber), 1/m
k_x	x-component of wavevector, 1/m
k_y	y-component of wavevector, 1/m
k_z	z-component of wavevector, 1/m
KLM	Kerr-Lens Mode-locked

L	propagation distance or fiber length, m
L_D	dispersion length
LMA	large mode area
M	*ABCD* matrix
n	refractive index
n_g	group index
OCT	optical coherence tomography
P	polarization
P_L	linear polarization
P_{NL}	nonlinear polarization
PCF	photonic crystal fiber
q	Gaussian complex beam parameter
R	inverse of phase curvature
t	time (s)
Tb	terabit
TOD	third order dispersion
u	scalar field in paraxial approximation
UV	ultraviolet
v_g	group velocity
w	beam radius
(x,y,z)	Cartesian coordinates
z_R	Rayleigh range (confocal parameter)
ZDW	zero-dispersion wavelength

α	attenuation coefficient
β	propagation constant
β_2	group velocity dispersion parameter
ΔT	temporal broadening
$\Delta\omega$	spectral width
ε	permittivity of free space
λ	wavelength, m
μ	permeability of free space
∇^2	Laplacian
∇_T^2	transverse Laplacian
χ_e	electric susceptibility
ψ	scalar field
$\tilde{\psi}$	complex amplitude of scalar field
ω	angular frequency

List of Tables

Table **Page**

List of Figures

Figure **Page**

Figure **Page**

Figure **Page**

Figure **Page**

Figure **Page**

1 Introduction

In 1930, Heinrich Lamm reported the first demonstration of light guidance in optical fibers when he used a short bundle of glass fibers to transmit the image of a light bulb filament. The simple, unclad optical fibers guided light based on the principle of total internal reflection, but it was not until 1953 that a cladding layer was added, providing considerable improvement in transmission. By 1960, the first working laser was reported by Theodore Maiman and losses for glass-clad optical fibers were about 1 dB/m. During the 1960s and 1970s, both optical fibers and laser sources saw considerable advances in performance. Significant progress in the fabrication of optical fibers was made in the 1970s and the losses were reduced to 0.2 dB/km by 1979. The process of Q-switching was reported in 1962, making laser pulses in the nanosecond regime and kW peak powers possible for the first time [1]. Peak powers grew even more with the invention of mode-locking, which produced picosecond (10^{-12} s) and eventually femtosecond (10^{-15} s) pulses of light. By 1982, mode-locked and amplified lasers were producing peak powers in the multi-gigawatt regime [2].

The combination of high power laser sources and optical fibers has enabled many technologies such as *in vivo* laser surgery, laser welding and laser machining. However,

as applications demand shorter and more energetic pulses be delivered to the target, the limits of standard step-index fibers are quickly being reached. Nowhere is this more apparent than in the delivery of amplified femtosecond laser pulses, which routinely reach peak powers in the gigawatt regime. Maintaining the properties of a femtosecond pulse as it traverses an optical waveguide is complicated by extremely high intensity, which can lead to beam deteriorating nonlinear effects and waveguide damage from optical breakdown. The following sections discuss some of these limitations as well as the utility of femtosecond pulses and how fiber delivery of femtosecond pulses could benefit numerous applications.

1.1 Overview of Femtosecond Lasers and Applications

The first femtosecond regime laser pulses were demonstrated by Ippen *et al.* in 1974 using a passively mode-locked CW dye laser [3]. Over the following decades, femtosecond pulses were obtained from mode-locked semiconductor and eventually rare-earth doped crystalline lasers. Kerr-lens mode-locked (KLM) Ti:Sapphire lasers have now produced pulses as short as 5fs [4].

Today, femtosecond regime lasers are commercially available and finding widespread use in applications such as materials processing, microscopy, spectroscopy, communications and nonlinear optics. A wide range of materials including metals, semiconductors, polymers, glasses and ceramics can be precisely micro-machined using femtosecond laser pulses due to the ability to deposit energy efficiently and rapidly. Heat diffusion is significantly reduced compared to long pulse lasers and therefore the ablation thresholds are well defined and the heat affected zone (HAZ) is minimized, resulting in

precise, well-defined microstructures. Microscopy techniques such as two-photon microscopy and optical coherence tomography (OCT) also benefit from femtosecond laser pulses. Two-photon microscopy makes use of the quadratic dependence of two-photon absorption on the pump intensity for highly localized reactions, while OCT makes use of the large coherent spectral bandwidth associated with femtosecond pulses to achieve high spatial resolution. Femtosecond optical spectroscopy applications such as femtosecond-stimulated Raman spectroscopy and other pump-probe arrangements are being used to dissect the dynamics of molecular interactions on an ultrafast timescale. Communications systems employing temporal solitons of femtosecond pulses could reach bitrates of multiple Tb/s. The high intensities associated with femtosecond pulses also make them key sources for exploring nonlinear optics. Processes such as supercontinuum generation are now easily achieved by passing femtosecond laser pulses through nonlinear media.

1.2 Waveguiding Femtosecond Laser Pulses

All of the applications in Section 1.1 would benefit from optical fibers or waveguides that could deliver a high quality beam of high intensity femtosecond pulses in a compact and robust package. However, while many systems exist that can deliver nanosecond pulses with significant peak power, the extreme intensities associated with femtosecond pulses makes them prohibitively difficult to deliver using conventional fibers and waveguides due to nonlinear optical effects, temporal dispersion and optically induced damage [5].

When femtosecond pulses interact with transparent dielectric materials, such as the glasses that comprise the cores and claddings of conventional fiber optics, a host of

different physical phenomena can occur. These phenomena are dependent on the properties of the laser pulse (wavelength, energy, temporal duration and spectral bandwidth) as well as the properties of the material (refractive index, nonlinear and absorption coefficients). As femtosecond pulses of even moderate energy have peak powers in the kW regime, coupling these pulses into single-mode fibers with cores < 10 μm diameter can easily reach intensities on the order of GW/cm^2. At these intensities, the intensity dependent refractive index can distort and spectrally broaden the pulse through self-phase modulation. Combined with chromatic dispersion in the normal dispersion regime, the pulse can be significantly broadened temporally at the fiber output. Furthermore, *amplified* femtosecond pulses focused to a 10 μm spot size can reach intensities of TW/cm^2, sufficient to cause bulk damage.

A number of different specialty fibers have been developed for the purpose of delivering high power laser radiation. Most of these fibers rely on either increasing the mode field area (thereby decreasing the intensity), guiding in a region of low third-order nonlinearity such as air, or a combination of both. Some examples that are investigated in this dissertation are large mode area (LMA) photonic crystal fibers, hollow silica waveguides and waveguide arrays. A brief discussion of each of these fibers follows; a more detailed explanation of their guiding properties will be given in Chapter 4.

The photonic crystal fiber (PCF) was introduced by Knight *et al.* in 1996 [6]. In contrast to the solid, low refractive index cladding in conventional fibers, the cladding of a PCF is comprised of a periodic arrangement of air holes that run the entire length of the fiber, the size and spacing of which determine the guiding properties. Photonic crystal fibers can be classified into several groups, depending on the core type and guiding

mechanism. Two LMA-PCFs are investigated in this dissertation. The first has a solid 23 μm core diameter and guides light based on modified total internal reflection; it also exhibits a remarkable property of single-mode guidance that is independent of core size and wavelength. The second photonic crystal fiber has a hollow core and guides light in air using a kagome lattice cladding. Air guidance significantly reduces nonlinear effects, since air has a nonlinear coefficient 1000 times smaller than that of fused silica.

Another specialty fiber, hollow silica waveguide, with inner thin-film coatings of silver and dielectric, was developed by Miyagi *et al.* for delivery of infrared light [7]. These waveguides were originally used to deliver CO_2 and Er:YAG laser energy although similar waveguides have more recently been used to deliver ultraviolet, visible and near-infrared light [8, 9]. Matsuura *et al*. have also recently demonstrated the delivery of high power femtosecond regime pulses using a cyclic olefin polymer (COP) coated hollow waveguide [10]. Femtosecond pulse delivery in four hollow silica waveguides with bore diameters of 300, 500, 750 and 1000 μm is investigated in this dissertation.

Multicore fibers, which contain multiple evanescently-coupled single-mode cores were introduced by Glas et al. in 1998 [11]. Originally developed for increasing the power handling in fiber lasers and amplifiers, these fibers support eigenmodes that are a combination of the individual guided modes of each core, the so-called supermodes. The number and degeneracy of the supermodes is dependent on the number of cores and the geometric symmetry of their positions within the cladding. The utility in multicore fibers for ultrashort pulse delivery is that they are scalable to very large mode-areas by simply adding more cores. With the proper array design and supermode discrimination, multicore fibers could be capable of handling relatively high power with high-brightness

output. This dissertation investigates femtosecond direct-written waveguide arrays as a means of examining the supermode behavior of several different array designs. An introduction on the femtosecond direct-write process is given in the following section with a detailed explanation given in Chapter 5.

1.3 Femtosecond Direct-Written Waveguides

An interesting application of femtosecond laser pulses is the ability to direct-write waveguides in transparent materials. In 1996 Davis *et. al.* demonstrated direct-written optical waveguides in the bulk of a fused silica substrate [12]. By focusing femtosecond pulses into a bulk transparent substrate and then translating the substrate with respect to the beam, continuous 'tracks' of high refractive index can be 'written' into the material. When the conditions are properly selected, the tracks can form single-mode optical waveguides.

Many groups have used this technique to fabricate optical waveguides in other substrates such as phosphate glasses, polymers, crystals and rare-earth doped glasses. Complex devices such as splitters, directional couplers, interleavers and waveguide lasers have also been demonstrated. The ability to fabricate complex three-dimensional (3-D) embedded waveguides using this technique provides research opportunities in the field of coupled-mode waveguide devices that were not possible with ion-exchanged waveguides or optical fiber drawing. Understanding the coupling conditions in waveguide arrays, for example, is becoming increasingly important as fiber laser arrays are scaled-up in power with the requirement of maintaining beam quality. In Chapter 5, we show that direct-

written waveguides can be used as a prototyping tool to explore the coupling properties and modal power distributions in novel waveguide arrays.

1.4 Purpose of This Study

The purpose of this dissertation is to investigate ultrashort pulse delivery in specialty fibers and waveguides. Three types of waveguides are evaluated: large mode-area photonic crystal fibers, hollow silica waveguides and multicore waveguides. Advantages and drawbacks of each type of waveguide for ultrashort pulse delivery are determined through numerical and experimental analysis.

Numerical analysis of multicore waveguides is used to design novel arrays with tailored modal power distributions that are dependent on the properties of a single core in the array [13]. These designs are evaluated experimentally by fabricating waveguide arrays using the femtosecond direct-write technique and then testing the as-fabricated arrays for ultrashort pulse delivery [14].

A novel numerical analysis technique for evaluating the guided modes of an actual photonic crystal fiber based on a scanning electron micrograph is presented. The method takes into account manufacturing flaws in the fiber to give a simulated representation of the actual guided mode.

The first systematic study of femtosecond pulse delivery in four different hollow silica waveguides is presented [15]. The loss and temporal dispersion of near-infrared femtosecond pulses as a function of waveguide bore diameter, bend and input polarization are determined. The results are in excellent agreement with a theoretical model of temporal dispersion in hollow silica waveguides [16].

The first reported tissue ablation using Fresnel-lens-focused femtosecond pulses delivered through hollow silica waveguide is presented. The results are found to be identical to those of free-space ablated tissues [15].

1.5 Chapter Overview

Chapter 2 discusses the physical phenomena associated with femtosecond pulse interaction with transparent materials. Section 2.1 discusses focusing a Gaussian beam in free-space into a transparent material with a higher refractive index. Section 2.2 introduces the phenomena of dispersion and nonlinear effects such as self-phase modulation, inelastic scattering and self-focusing. Section 2.3 discusses the processes by which femtosecond pulses are absorbed and ionize transparent materials. Section 2.4 discusses the modifications that can be induced in the bulk of transparent materials by femtosecond laser pulses.

Chapter 3 introduces numerical models that are used to evaluate the modal properties of specialty fibers such as multicore fibers and photonic crystal fibers. Section 3.1 introduces the scattering matrix method, which will be used extensively throughout the dissertation. Section 3.2 discusses numerical modeling of multicore waveguides using the scattering matrix method and coupled mode analysis. Section 3.3 introduces a method for tailoring the modal power distribution of waveguide arrays based on altering the properties of a single core in the array. Section 3.4 describes how the scattering matrix method can be used to model photonic crystal fibers.

Chapter 4 experimentally evaluates the propagation of femtosecond pulses in several different specialty fibers including: photonic crystal fiber, photonic bandgap fiber and hollow silica waveguides. Section 4.1 investigates femtosecond pulse delivery in a large mode-area, solid-core photonic crystal fiber. A method for simulating the modes of the photonic crystal fiber is presented and the results are compared to experimental guided modes. Section 4.2 investigates femtosecond pulse delivery in a large mode-area, hollow-core photonic crystal fiber. Section 4.3 examines femtosecond pulse delivery in hollow silica waveguides with four different bore diameters. Measured temporal dispersion values are compared to a recently developed model.

Chapter 5 discusses direct-writing of optical waveguides in glass. An overview of the process and process variables are given in Section 5.1. Section 5.2 discusses the experimental setup that was used for direct-writing waveguides. Waveguide arrays that test concepts of supermode tailoring that were introduced in Chapter 3 are presented in Sections 5.3 and 5.4. Section 5.3 discusses waveguides and arrays written in soda-lime glass, while Section 5.4 discusses waveguides and arrays written in high purity fused silica.

Chapter 6 summarizes the main findings of the dissertation and discusses applications and future directions for the research. A summary of the specialty fibers and waveguides tested is given in Section 6.1 along with a table describing their properties and performance. Section 6.2 demonstrates an application in which hollow silica waveguides were used to deliver ultrashort pulses for the ablation of porcine tissues. Diffractive optic

focusing of the hollow silica waveguide output is discussed in Section 6.2.2. Finally, future research directions are discussed in Section 6.3.

2 Ultrashort Pulse Interaction with Transparent Materials

The interaction of laser light with transparent materials has been studied extensively in the development of high power lasers. Ultrashort laser pulses with relatively low nanojoule pulse energies, when moderately focused in the bulk of transparent materials, can have sufficient intensity to cause nonlinear optical effects to occur, leading to refractive index variation and changes in the amplitude, phase and frequency of the exciting pulse. Given high enough intensity, ultrashort pulses can induce morphological changes such as color center formation and densification which can lead to permanent refractive index modification in transparent materials. In order to predict the response of transparent materials to ultrashort pulse excitation, several factors must be taken into account, namely the focusing conditions, the nonlinear propagation of the pulses in the material, the electron-phonon-lattice dynamics in the vicinity of the beam waist and the mechanisms and morphology responsible for refractive index modification.

2.1 Gaussian Beam Focusing in Transparent Materials

The interaction of femtosecond pulses with a transparent medium is highly dependent on the focusing conditions. The propagation characteristics of a focused Gaussian beam can be determined using either geometrical (ray) optics or wave optics in the paraxial approximation. The paraxial wave treatment using the Huygens-Fresnel-Kirchoff integral will be applied in this section to the analysis of focusing a Gaussian beam into a transparent medium.

2.1.1 Focusing in the Paraxial Limit

Consider the scalar field,

$$\psi(x,y,z,t) = \tilde{\psi}(x,y,z)e^{j\omega t} \tag{2.1}$$

whose complex amplitude, $\tilde{\psi}$ satisfies the scalar wave equation

$$\left(\nabla^2 + k^2\right)\tilde{\psi}(x,y,z) = 0 \tag{2.2}$$

where $k = \omega^2\mu\varepsilon$. A general solution to (2.2) is given by a summation of plane waves $e^{-jk_x x}e^{-jk_y y}e^{-jk_z z}$. By assuming the k-vectors are approximately in the k_z direction (*i.e.* taking $\frac{\sqrt{k_x^2 + k_y^2}}{k} << 1$), then k_z can be written as $k_z \approx k - \frac{k_x^2 + k_y^2}{k}$. The fast k_z dependence is thereby factored out of ψ. This is the so-called *paraxial approximation*. In this case, the scalar field can be written as

$$\psi(x,y,z,t) = u(x,y,z)e^{-jkz} \tag{2.3}$$

where u is a slowly varying function. Substituting (2.3) into (2.2) gives the paraxial wave equation

$$\nabla_T^2 u - 2jk\frac{\partial u}{\partial z} = 0 \tag{2.4}$$

with $\nabla_T^2 = \left(\partial^2/\partial x^2\right) + \left(\partial^2/\partial y^2\right)$. In addition to this differential form, u can also be derived from the integral form known as the Huygens-Fresnel-Kirchoff integral in the Fresnel approximation, given by

$$u(x,y,z) = \frac{j}{\lambda z}\iint_s u_0(x_0,y_0,z_0)e^{\left\{-jk\left[\frac{(x-x_0)^2+(y-y_0)^2}{2z}\right]\right\}}dx_0dy_0\,. \tag{2.5}$$

This integral is completely equivalent to (2.4), but offers a more intuitive approach because it explicitly states the beam shape $u(x,y,z)$ with propagation, given an initial beam shape $u_0(x_0,y_0,z_0)$.

In order to simplify the analysis of a beam propagating through an optical system comprising multiple elements, an ABCD matrix is used. This 2×2 element matrix $\left(M = \begin{bmatrix} A & B \\ C & D \end{bmatrix}\right)$ completely describes an optical system within the paraxial approximation. By considering a general optical system with an infinite aperture (i.e. no field limiting apertures in the transverse plane) and applying Huygens principle, (2.5) can be written in the following form:

$$u(x,y,z) = \frac{j}{B\lambda}\iint_s u_0(x_0,y_0,z_0)e^{\left\{-jk\left[\frac{A\left(x_0^2+y_0^2\right)+D\left(x^2+y^2\right)-2x_0x-2y_0y}{2B}\right]\right\}}dx_0dy_0\,. \tag{2.6}$$

An eigensolution to (2.6) is obtained when the double integral is taken between $-\infty$ and ∞, giving

$$u(x,y,z) \propto e^{\left\{-jk\left[x^2+y^2/2q\right]\right\}}. \tag{2.7}$$

The variable q is called the Gaussian complex beam parameter. Taking the initial beam shape as

$$u_0(x_0,y_0,z_0) \propto e^{\left\{-jk\left[x_0{}^2+y_0{}^2/2q_0\right]\right\}} \tag{2.8}$$

and substituting back into (2.6), again evaluating the double integral between $-\infty$ and ∞, gives

$$u(x,y,z) = \frac{1}{A+B/q_0} e^{\left\{-jk\left[x^2+y^2/2q\right]\right\}} \tag{2.9}$$

The complex beam parameters q and q_0 are related by the ABCD law,

$$q = \frac{Aq_0+B}{Cq_0+D}. \tag{2.10}$$

A Gaussian beam can be physically interpreted as a spherical wave of complex beam parameter q. Separating q into its real and imaginary components gives

$$\frac{1}{q} = \frac{1}{R} - j\left(\frac{\lambda}{n\pi w^2}\right) \tag{2.11}$$

where w and 1/R are the beam radius and phase curvature respectively. Using (2.10) and (2.11), the transformation of a Gaussian beam by an optical system can be determined.

The q-parameter formalism will now be applied to evaluating the focusing of a Gaussian beam into a transparent material of refractive index n_1. A collimated $\left(R=\infty\right)$ beam is

assumed incident on a lens, so $q_0 = j\left(\frac{n\pi w^2}{\lambda}\right)$. The ABCD matrices of the focusing lens, free-space propagation, interface and bulk dielectric are given by:

$$M_{lens+propagation} = \begin{bmatrix} 1-\frac{L}{f} & L \\ -\frac{1}{f} & 1 \end{bmatrix},\ M_{\text{int}erface} = \begin{bmatrix} 1 & 0 \\ 0 & \frac{n_0}{n_1} \end{bmatrix} \text{ and } M_{dielectric} = \begin{bmatrix} 1 & z \\ 0 & 1 \end{bmatrix}$$

Multiplying these terms to obtain the ABCD parameters and substituting the result into (2.10) along with q_0, yields the q-parameter inside the dielectric medium. The result is illustrated in Figure 2-1. Several features are obvious from this plot and can be generalized via algebraic manipulation of the calculated q-parameter. Notably, refraction causes the beam to focus at $z = f' = n_1 f$, where n_1 is the refractive index of the dielectric and f is the lens focal length. The beam waist, w_0, is unchanged from the beam waist in air, however, the Rayleigh range, $z_R = \pi w_0^2 / \lambda$ (a.k.a. confocal parameter) is extended to $n_1 z_R$.

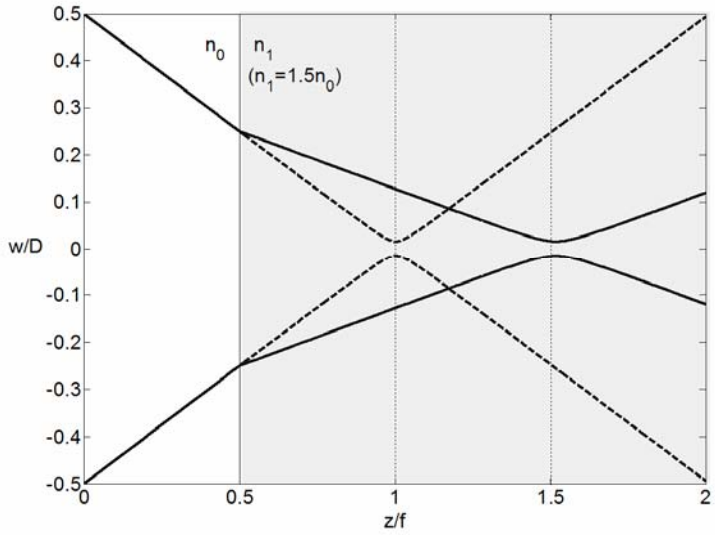

Figure 2-1. Gaussian beam focusing through an air/dielectric interface. A Gaussian beam of diameter D passes through a lens of focal length f at z = 0 and is incident on a dielectric interface at $z = 0.5f$ (shaded area). The case of focusing a Gaussian beam in air is also illustrated (dashed line).

The paraxial approximation is valid for focusing lenses with numerical apertures < 0.45 and generally within 20% for numerical apertures up to 0.65 [17]. The experiments performed within this dissertation use lenses with numerical apertures < 0.45, therefore the paraxial approximation is assumed when examining the focusing conditions.

2.2 Propagation of High Intensity Femtosecond Pulses in Transparent Waveguides

The previous section described focusing a beam across an air/dielectric interface into the bulk of a transparent material. Once the laser pulses are in the material, they are subject to the properties of the material such as dispersion, nonlinear refractive index and vibrational modes. This section discusses each these phenomena and describes their consequences on femtosecond pulse propagation in optical waveguides.

2.2.1 **Dispersion**

Temporal pulse broadening in transparent optical waveguides is the result of dispersion, which may be either intermodal or intramodal. Intermodal (a.k.a multi-path or modal delay) dispersion occurs in multimode optical fibers due to the time difference between the shortest and longest paths a ray may take through the fiber. In the modal picture, this is associated with the difference in group delay for each of the modes in the fiber. For a step-index fiber, this time difference is given by:

$$\Delta T = \frac{n_1}{c}\left(\frac{L}{\sin\phi_c} - L\right) = \frac{L}{c}\frac{n_1^{\,2}}{n_2}\Delta \tag{2.12}$$

where n_1 and n_2 are the refractive indices of the core and cladding respectively, c is the speed of light in vacuum, L is the fiber length, $\Delta \approx (n1 - n2)/n1$ is the normalized index difference between the core and the cladding and $\phi_c = \cos^{-1}\left(\frac{\sqrt{n_1^{\,2} - n_2^{\,2}}}{n_1}\right) = \cos^{-1}\left(\frac{NA}{n_1}\right)$ is the critical angle required for total internal reflection from the cladding [18]. Intermodal dispersion can be reduced in graded index fibers where the oblique rays travel in a lower refractive index than the rays in the core. This makes up for the path length time difference, allowing all of the rays to reach the output at nearly the same time. Single-mode fibers eliminate intermodal dispersion completely, since there is only a single group delay associated with the fundamental mode.

Intramodal dispersion, or Group-Velocity Dispersion (GVD), is present even in single-mode fibers and consists of both chromatic and waveguide dispersion. Chromatic

dispersion is the wavelength dependence of the refractive index experienced by a pulse as it passes through a material. Its origin lies in the atomic and molecular resonances that are present in the material. Far away from these resonances, the refractive index can be approximated by the Sellmeier equation:

$$n^2(\omega) = 1 + \sum_{j=1}^{M} \frac{B_j \omega_j^{\,2}}{\omega_j^{\,2} - \omega^2} \tag{2.13}$$

where, $\omega_j = 2\pi \cdot c / \lambda_j$ is the oscillator frequency and B_j is the oscillator strength [18-20]. In practice, these terms are typically obtained by fitting the measured dispersion curves to the Sellmeier equation. For silica, a three term Sellmeier equation (M = 3) is typically used, accounting for the resonances in the ultraviolet and infrared [19]. Material dependent coefficients can be used to solve the Sellmeier equation and determine the group index given by [18-20]:

$$n_g = n + \omega\left(\frac{dn}{d\omega}\right) \tag{2.14}$$

The group index is the refractive index experienced by a spectral component at frequency ω as it propagates through a medium. The corresponding velocity of the spectral component in the medium is called the group velocity and is given by [18-20]:

$$v_g = \left(\frac{d\beta}{d\omega}\right)^{-1} = \frac{c}{n_g} \tag{2.15}$$

where β is the propagation constant for a particular eigenmode. $\beta(\omega)$ can be expanded in a Taylor series about the carrier frequency ω_o given by [18]:

$$\beta(\omega) = \beta_0 + (\omega - \omega_0)\beta_1 + \frac{1}{2}(\omega - \omega_0)^2 \beta_2 + \frac{1}{6}(\omega - \omega_0)^3 \beta_3 + \ldots, \tag{2.16}$$

where,

$$\beta_m = \left(\frac{d^m \beta}{d\omega^m} \right)_{\omega=\omega_0} \qquad (m = 1,2,3,....) \tag{2.17}$$

Chromatic dispersion in fused silica has two regimes, normal and anomalous, which result from the group index behavior for the material. The minimum value for the group index occurs at a wavelength called the zero-dispersion wavelength (ZDW), which is approximately 1270-1290 nm for fused silica, depending on the presence of dopants and their concentration. At wavelengths shorter than the ZDW, the group index increases with decreasing wavelength, implying that the longer wavelength spectral components have a higher group velocity than the shorter wavelength spectral components. This is called the normal dispersion regime. The anomalous dispersion regime occurs at wavelengths longer than the ZDW, where the group index increases with increasing wavelength, implying that the longer wavelength spectral components have a lower group velocity than the shorter wavelength components. A pulse propagating in either of these regimes will undergo a temporal broadening of

$$\Delta T = \frac{dT}{d\omega}\Delta\omega = \frac{d}{d\omega}\left(\frac{L}{v_g}\right)\Delta\omega = L\beta_2\Delta\omega = DL\Delta\lambda \tag{2.18}$$

where β_2 is the Group Velocity Dispersion (GVD) parameter, L is the fiber length, $\Delta\omega$ is the spectral width of the input pulse and $D = \left(\frac{-2\pi c}{\lambda^2}\right)\beta_2$ is the dispersion parameter.

Since the propagation constant, β, is dependent on both material and waveguide properties, the dispersion parameter D, which contains β, can be written as a sum of two terms D_M and D_W to represent the material and waveguide contributions respectively. These are given by:

$$D_M = -\frac{2\pi\Delta}{\lambda^2}\frac{dn_{2g}}{d\omega} = \frac{1}{c}\frac{dn_{2g}}{d\lambda} \quad \text{and,} \tag{2.19}$$

$$D_W = -\frac{2\pi\Delta}{\lambda^2}\left[\frac{{n_{2g}}^2}{n_2\omega}\frac{Vd^2(Vb)}{dV^2} + \frac{dn_{2g}}{d\omega}\frac{d(Vb)}{dV}\right] \tag{2.20}$$

where n_{2g} is the group index of the cladding, V is the fiber V-parameter and b is the fiber b-parameter [18, 19]. Unlike D_M, which is negative below and positive above the ZDW, D_W is negative for all wavelengths. This property allows the creation of dispersion shifted and dispersion flattened fibers by varying the magnitude of D_W by simply altering the fiber parameters.

Third Order Dispersion (TOD) must be considered when the wavelength is near the ZDW or when the pulse width is < 1ps. It results in an oscillatory structure on either the leading or trailing edge of the pulse, depending on whether β_3 is negative or positive respectively. For β_2 = 0, the oscillations cause the intensity to go to zero between the peaks and for small β_2 the oscillations are damped and a long continuous tail is formed.

The dispersion length $L_D = T_0^2/|\beta_2|^2$, where T_0 is the initial temporal half-width at the 1/e intensity point, provides a length scale over which dispersive effects become important for pulse evolution in a dielectric medium. For TOD, $L_D' = T_0^3/|\beta_3|$. If L_D is on the order of the medium length L, dispersive effects must be considered. If $L_D' \le L_D$, then TOD effects must also be considered.

2.2.2 **Nonlinear Effects**

Nonlinear effects in optical waveguides arise from nonlinear contributions to the polarization P, which is physically the dipole moment per unit volume and originates from atomic and molecular resonances present in materials. In the classical model of light interaction with matter, an electron or atom can be made to oscillate when displaced from its equilibrium position. The time-varying electric field of the incident light provides the driving force while the restoring forces arise from adjacent atoms or the nucleus in the case of a single electron. The resonant frequency is determined by the magnitude of the restoring forces and the mass of the oscillating body. The periodic charge displacement caused by the oscillation produces a dipole moment that varies sinusoidally in time with the oscillation. The sum of all these induced dipole moments gives the polarization. The contributions of the atomic and molecular resonances to the refractive index, dispersion and absorption are through the electric susceptibility, $\chi_e = \chi_e' + j\chi_e''$ which defines the complex refractive index given by $n = (1 + \chi_e' + j\chi_e'')^{1/2} = n' + jn''$. The propagation constant and attenuation coefficient are then given by $\beta = n'k_o$ and $\alpha = n''k_o$ respectively [19].

The polarization is related to the electric field E through $P = \varepsilon_0 \chi_e E = P_L + P_{NL}$, where χ_e is the electric susceptibility function and P_L and P_{NL} are the linear and nonlinear contributions to P [18-21]. This may also be written as $P = \varepsilon_o\left(\chi^{(1)} \cdot E + \chi^{(2)} \cdot EE + \chi^{(3)} \cdot EEE + \ldots\right)$, where $\chi^{(j)}$(j=1,2,…) is the jth order susceptibility and $\chi^{(j)}$ is a tensor of rank j+1 [18]. The linear (and dominant)

contribution to P is given by $\chi^{(1)}$. The nonlinear contribution to P is given by the higher-order susceptibilities, with the lowest order nonlinear effects originating from $\chi^{(3)}$. For silica, the second-order susceptibility is zero since SiO_2 has inversion symmetry [19, 21]. In a linear, homogeneous, isotropic media, χ_e is independent of field strength, position within the material and field orientation

Nonlinear effects originating from the third-order susceptibility, $\chi^{(3)}$ include third-harmonic generation (THG), four-wave mixing (FWM), and effects due to nonlinear refraction such as self-phase modulation (SPM) and cross-phase modulation (XPM). THG and FWM require special phase matching techniques to be efficient and can be neglected for most cases. Other nonlinear effects are caused by inelastic scattering which results from the exchange of energy from the high intensity pulse to the material. This scattering is related to the vibrational excitation modes of the silica molecules and can be classified as either Stimulated Raman Scattering (SRS) or Stimulated Brillouin Scattering (SBS). SRS and SBS are discussed in more detail in Section 2.2.4.

A useful term in characterizing the extent of nonlinear propagation in optical fibers is the nonlinear length, $L_{NL} = 1/(\gamma \cdot P_0)$ where $\gamma = k_0 n_2 / A_{eff}$, A_{eff} is the effective mode cross section, P_0 is peak power of the incident pulse and n_2 is the nonlinear index coefficient [18, 20]. If the medium length, L << L_{NL}, then nonlinear effects can be neglected. However, for L on the order of or larger than L_{NL}, nonlinear effects must be considered.

The refractive index of fused silica has a nonlinear dependence on the intensity of the applied field. This nonlinear refractive index can be written as [18-21]:

$$n = n_o + \bar{n}_2 \left\langle \tilde{E}^2 \right\rangle = n_o + 2\bar{n}_2 \left| E(\omega) \right|^2 = n_o + n_2 I \tag{2.21}$$

where n_o is the weak field refractive index, E is the electric field, I is the intensity of the field in the material and n_2 is the nonlinear index coefficient. The relation between n_2 and $\bar{n}_2$ is given by:

$$n_2 = \frac{4\pi}{n_o c} \bar{n}_2 \tag{2.22}$$

and the dependence of n_2 on the third order susceptibility is given by:

$$n_2 = \frac{12\pi^2}{n_o^2 c} \chi^{(3)} \tag{2.23}$$

If the optical field is assumed to be linearly polarized so that only the $\chi^{(3)}_{xxxx}$ component contributes to the refractive index, then

$$n_2 \approx \frac{3}{8n_o} \mathrm{Re}\left(\chi^{(3)}_{xxxx}\right) \tag{2.24}$$

For fused silica, $n_2 \approx 3 \times 10^{-16}\, cm^2/W$ [18-20].

2.2.3 **Self-Phase Modulation**

The intensity dependence of the refractive index introduced through the nonlinear index coefficient leads to a phenomenon called self-phase modulation (SPM). An optical field in a fiber will undergo a self-induced phase shift whose magnitude is given by:

$$\phi = nk_o L = (n_o + n_2 \left| E \right|^2) k_o L = \phi_L + \phi_{NL} \tag{2.25}$$

where $k_o = 2\pi/\lambda$ and L is the fiber length [18-20]. The nonlinear phase-shift $\phi_{NL} = n_2 k_o L|E|^2$ is due to SPM. The effect of SPM on the shape and frequency spectrum of a propagating pulse can be described by considering a plane wave propagating in the *z* direction with a linearly polarized electric field given by [19]:

$$\tilde{E} = \frac{1}{2} E_0(z,t) e^{-j(nk_0 z - \omega_0 t)} + c.c. \tag{2.26}$$

where $E_o(z,t)$ is the pulse envelope, ω_o is the center frequency and c.c. is the complex conjugate. Including the nonlinear refractive index gives:

$$\tilde{E} = \frac{1}{2} E_0(z,t) e^{-j(n_o k_0 z)} e^{-j(\delta\phi(t) + \omega_0 t)} + c.c. \tag{2.27}$$

where $\delta\phi(t) = n_2 k_0 |E_0(z,t)|^2 z$. By differentiating the time dependent terms, the instantaneous frequency can be found:

$$\omega = \frac{\partial}{\partial t}(\omega_0 t - \delta\phi(t)) = \omega_0 + \delta\omega(t) \tag{2.28}$$

where $\delta\omega(t) = -n_2 k_0 z \frac{\partial}{\partial t}|E_0(z,t)|^2$. Qualitatively, SPM introduces new frequency components to the pulse through $\delta\omega(t)$. This added frequency content is distributed over the pulse envelope in a positively chirped fashion (i.e. the leading edge of the pulse is red shifted and the trailing edge is blue shifted). The maximum phase shift occurs at the pulse center (T = 0) and is given by $\phi_{\max} = L_{eff}/L_{NL} = \gamma \cdot P_0 L_{eff}$, where $L_{eff} = [1 - e^{-(\alpha L)}]/\alpha$ is the effective medium length which takes into account the loss α. The maximum frequency shift occurs at the positions where the slope of the pulse is of maximum magnitude (the inflection points) and is proportional to $\phi_{\max}/T_0$.

For cases where the dispersion length L_D is on the order of the fiber length L, the combined effects of SPM and GVD must be considered [18]. In the normal dispersion regime, SPM enhances temporal broadening because of its positive frequency chirp. This in turn causes ϕ_{max} to decrease due to the drop in peak power, reducing spectral broadening compared to the case with zero GVD. In the anomalous dispersion regime, the positive chirp due to SPM is nearly cancelled by the negative chirp due to GVD. This interplay between SPM and GVD can lead to the propagation of undistorted, chirp free pulses called solitons.

2.2.4 Inelastic Scattering

Two types of inelastic scattering that occur silica glasses are stimulated Raman scattering (SRS) and stimulated Brillouin scattering (SBS). The spontaneous Raman scattering effect can be viewed as an inelastic collision between an incident photon and a molecule that slightly excites the material resonances and causes the vibrational or rotational energy to change by an amount $\Delta E = h\upsilon_i - h\upsilon_s$ where υ_i is the frequency of the incident photon and υ_s is the frequency of the scattered photon. For $\upsilon_s < \upsilon_i$, the scattered light is called a Stokes wave and for $\upsilon_s > \upsilon_i$ the scattered light is called an anti-Stokes wave. In silica glasses, the Stokes process dominates and propagates in the same direction as the incident wave. As the Stokes wave increases in intensity, it can interact with the incident wave (pump) to further excite the material resonances, enhancing the Raman process by increasing the rate of frequency conversion. This enhanced interaction is called SRS.

An approximate threshold power, defined as the input pump power at which the Stokes power becomes equal to the pump power at the fiber output is given by:

$$P_{SRS} \approx \frac{16 \cdot K_{SRS} \cdot A_{eff}}{g_R L_{eff}} \tag{2.29}$$

where K_{SRS} = 1 if the polarization is preserved in the fiber and K_{SRS} = 2 if the polarization is completely scrambled, A_{eff} is the effective core area, g_R is the Raman gain coefficient and L_{eff} is the effective fiber length [21].

When ultrashort pulses (< 100ps) of significant power propagate in the normal dispersion regime of a dispersive medium, the combined effects of GVD, SPM, XPM, pulse walkoff and pump depletion must be taken into account. Pulse walkoff results from the difference in group velocity between the pump and Raman pulses. The Raman pulse builds up after one walkoff length, $L_W = T_o / \left(v_{g1} - v_{g2} \right)$ and causes pump depletion. After $\sim 3\, L_W$, the transfer of energy from the pump to the Raman pulse is nearly complete. The resulting spectra are broadened and asymmetric due to SPM and XPM. For pulses < 1ps, the Raman gain does not vary linearly over the entire bandwidth of the pulse and intrapulse Raman scattering must be considered.

SBS is inelastic scattering that results from the annihilation of a pump photon, creating a Stokes photon and an acoustic phonon simultaneously. It manifests itself through a backward propagating Stokes wave that carries most of the input energy when the Brillouin threshold is reached. However, since the spectral width of the Brillouin gain spectrum is very small, SBS can be neglected in the case of short pump pulses (< 10ns).

In the case of intense ultrashort pulses, the spectrum can be broadened to 100nm or more due to a combination of SPM and other nonlinear effects such as SRS and FWM occurring simultaneously. The resulting spectrum is called a supercontinuum.

2.2.5 **Self-Focusing**

Self-focusing occurs due to the intensity dependence of the refractive index. When a propagating pulse reaches a critical power, the beam can collapse due to the formation of a positive (Kerr) lens in the material. This occurs because the intensity is higher on-axis and creates a region of higher refractive index through the nonlinear index coefficient compared to the lower intensity wings. This lensing results in large intensities in the material and can lead to damage. The expression for the critical power for self-focusing is given by

$$P_{cr} = \frac{\alpha \lambda^2}{4\pi n_0 n_2} \tag{2.30}$$

where $\alpha \approx 1.83$, λ is the wavelength, n is the refractive index of the material and n_2 is the nonlinear index coefficient [22]. The critical power for self-focusing in silica glass is approximately 1.7 MW for $\lambda = 775nm$. A Gaussian beam with power P_0 greater than P_{cr} will self-focus after propagating a distance of

$$L = \frac{2\pi n_0 r_0^2}{\lambda}\left(\frac{P_0}{P_{cr}} - 1\right)^{-1/2} \tag{2.31}$$

where r_0 is the minimum waist radius of the beam [22].

2.2.6 **Self-Steepening**

Self-steepening results from the intensity dependence of the group velocity and causes the peak of a pulse to travel slower than the wings. This results in the trailing edge of a pulse becoming steeper as it propagates in the *z* direction. The spectrum is affected by

also becoming asymmetric and experiencing more spectral broadening on the short-wavelength side. The self-steepening parameter is given by [18]

$$s = \frac{1}{\omega_0 T_0}. \tag{2.32}$$

Self-steepening can eventually lead to an optical shock as the trailing edge approaches vertical. This occurs at a distance of

$$z_s \approx 0.39\left(L_{NL} / s\right) \tag{2.33}$$

for Gaussian pulses.

2.3 Femtosecond Pulse Ionization Mechanisms in Transparent Materials

The optical bandgap of transparent dielectrics is wide in the visible and near-infrared. For example, fused silica has a bandgap of 9 eV, while a 775 nm photon has an energy of 1.6 eV. Therefore, in order ionization to occur, an electron must either absorb multiple photons simultaneously (multiphoton ionization) or it must be collisionally ionized by conduction band electrons accelerated in the optical field (impact ionization). Initial conduction band electrons must be produced by the process of multiphoton ionization or through defects and impurities in the material. Multiphoton ionization is the dominant mechanism for ultrashort pulse ablation, since it contributes substantially more electrons than are initially present due to defects [23]. Multiphoton ionization also has no threshold and can contribute so-called "seed" electrons to the conduction band even at low (< 10^{12} W/cm^2) intensities. For incident pulse intensities between 10^{12} and 10^{14} W/cm^2, subsequent impact ionization of these seed electrons then promotes other valence electrons into the conduction band. The process goes as follows: the seed electrons gain

energy from the incident laser field much faster than it can be transferred from the electrons to the lattice since the electron-ion transfer time in a dense plasma is on the order a few picoseconds [24]. Eventually, these electrons are accelerated to energies greater than the ionization potential and can collisionally ionize (impact ionization) neighboring atoms, thereby producing more free electrons. This avalanche continues until a critical density plasma is created where energy deposition from the laser is greatly reduced due to reflection from the critical surface [23]. For incident pulse intensities > 10^{14} W/cm^2, multi-photon ionization alone is sufficient to reach the critical plasma density and cause damage. Once ionization is complete, the free electron density is comparable to the ion density, approximately $10^{19} – 10^{23}$ cm^{-3}. At this point, the material no longer has the properties of a dielectric; in fact, all materials are similar in this state. The ensuing dynamics can then be expressed through the two-temperature diffusion model which describes the transition of the energy deposited in the electrons to the lattice [25].

2.4 Femtosecond Pulse Induced Modifications in Transparent Materials

The mechanisms responsible for the modification of the refractive index of materials exposed to femtosecond pulses have been under much debate in recent years. Typical modifications in transparent materials include the formation of color centers, densification, thermo-mechanical stress and void formation. This section describes how some of the most common morphological changes can occur as a result of femtosecond pulse-material interaction.

2.4.1 Color Center Formation

Femtosecond lasers pulses are capable of producing defects that render transparent dielectrics photosensitive. The creation of color centers has been observed for glasses such as high-purity borosilicate, alkali silicate and soda-lime silicate (soda-lime glass). Coloration is due to the creation of metastable vacancies and interstitial defects induced during femtosecond laser pulse irradiation. The threshold intensity for such defects is typically on the order of 10^{12} W/cm^2, lower than the threshold for bulk damage. For soda-lime glass, which is considered in section 5.3, the defects are attributed to trapped hole centers which link non-binding oxygen holes and neutral Na atoms [26]. These color centers have absorption peaks at 420 and 620 nm.

Although some groups have attributed an increase in refractive index to color center formation [27], others have shown that post-process annealing of samples can remove the color centers, while the increased refractive index persists [28, 29]. A more likely mechanism for at least part of the refractive index increase in glasses exposed to femtosecond pulses is densification, as discussed in the following section.

2.4.2 Densification and Compaction

Densification of fused silica exposed to near-infrared femtosecond pulses has been verified by Raman spectroscopy [30]. The Raman spectra obtained by Chan *et al.* show a large increase in the peaks at 490 and 605 cm^{-1} (the D1 and D2 bands respectively) as a function of the irradiating pulse energy. These peaks correspond to the breathing modes of 4- and 3-membered ring structures in the silica network. Since bond angle decreases with an increase in the number of rings, it follows that density is increased [30]. Another

study by Streltsov *et al.* also included the 1060 and 1200 cm^{-1} lines in addition to the D1 and D2 lines. They concluded that the fictive temperature was constant and that the shift of the 1060 cm^{-1} line combined with the behavior of the D1 and D2 lines was in fact due to densification and compaction of the femtosecond-pulse-exposed glass [31].

2.4.3 **Induced Stress**

Stresses can form in areas surrounding material exposed to femtosecond pulses as a direct consequence of volumetric changes or densification in the exposed region. These stresses can be evaluated through birefringence pattern analysis using polarization microscopy. By measuring the retardance of light through the sample from given birefringence data, Streltsov *et al.* have shown that induced stresses from densification can account for a portion of the refractive index increase [32].

2.4.4 **Void Formation**

Void formation is associated with high energy pulses producing micro-explosions in the focal volume that result in rapid expansion of hot electrons and ions into the surrounding material [33]. This represents an upper threshold for femtosecond-written waveguides and can result in significant power loss in fibers subjected to high energy pulses, as significant scatter occurs from regions which contain voids.

3 Numerical Modeling of Multicore and Photonic Crystal Waveguides

The propagation of light in a specialty fibers such as a multicore fiber or a photonic crystal fiber can be described by Maxwell's equations and is subject to the properties of the fiber such as the refractive indices of the core and cladding, the core (or hole) diameter and the core (or hole) spacing. A number of numerical methods exist for determining the eigenmodes that are supported by waveguide arrays and specialty fibers such as photonic crystal fiber. Photonic crystal fibers have been modeled using methods such as the plane wave expansion method, the effective index method, the beam propagation method and the finite-element method, among others. Multicore waveguides and fibers have been extensively modeled using coupled mode theory [34]. Bochove *et al.* and Huo *et al.* have recently used coupled mode theory with gain to more accurately predict the performance of multicore fiber lasers with 7- and 19-cores respectively [35, 36]. Yamashita *et al.* have applied a point matching method to analyze multicore waveguides [37]. This method, originally developed by Goell [38] is based on expansion of the electromagnetic fields in terms of circular harmonics. Wijngaard [39] and later

Huang and Chang [40] have also used circular harmonics expansion to analyze coupled waveguides.

Another method that is particularly useful in analyzing specialty fibers comprising multiple parallel cylinders, whether they are of high or low refractive index, is the Scattering Matrix Method. In the following sections, we apply the Scattering Matrix Method (SMM) to solve for the propagation constants of two different types of specialty fibers. The first type has high refractive index dielectric cores embedded in a low refractive index medium, similar to the cases studied by Lo *et al.* [41] and Felbacq *et al.* [42]. The resulting supermodes are used directly in coupled mode analysis to determine the power exchange as a function of distance along the waveguides. The next type is a photonic crystal fiber with low index inclusions that support leaky modes as in references [43-45].

3.1 The Scattering Matrix Method

Consider the two-dimensional system composed of N cylindrical parallel waveguides illustrated in Figure. 3-1. Each waveguide core j has a refractive index n_j and a local coordinate system (x_j, y_j). The waveguides share a common origin, O in a global Cartesian coordinate system with axes xyz and their centroids are located at position (r_j, θ_j). The distance between waveguides i and j is given by r_{ij}. In general, the cores can have arbitrary cross-sections [42], however, the waveguides discussed in this paper are assumed to be circular and invariant along the z-axis. The medium outside the cylinders is homogeneous and infinite with refractive index n_c.

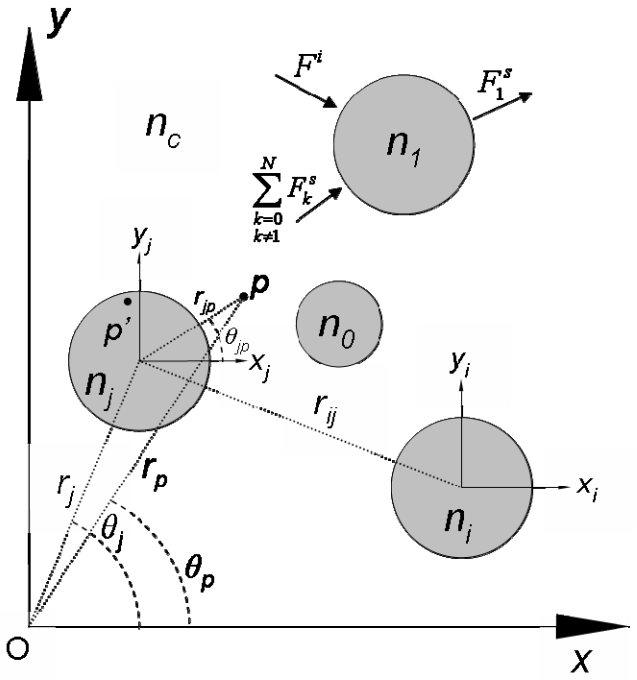

Figure. 3-1. General system geometry for the Scattering Matrix Method

In a locally homogeneous region, the longitudinal electric and magnetic fields of the structure, E_z and H_z respectively, satisfy the Helmholtz equation $\left(\nabla_\perp^2 + k_o^2 n_i^2 - \beta^2\right) F_z = 0$, where $F_z = E_z$ or H_z, $\nabla_\perp^2$ is the transverse Laplacian, $k_o = 2\pi/\lambda$ is the free-space wavenumber, λ is the wavelength, β is the propagation constant and n_i is the refractive index with $i = 1$ in the core and $i = 2$ in the cladding.

The longitudinal fields may be expanded about a point, p in the vicinity of core j in a Fourier-Bessel series [46]. For point p in the cladding,

$$F_z(r_p, \phi_p) = F_z^i(r_p, \phi_p) + F_z^s(r_p, \phi_p) \tag{3.1}$$

where,

$$F_z^s(r_p, \phi_p) = \sum_{j=1}^{N} \sum_{m=-\infty}^{\infty} b_{jm}^{E,H} H_m^{(1)}(k_2 r_{jp}) \times \exp\left(im\phi_{jp}\right) \exp\left(i\beta z_p\right) \tag{3.2}$$

is the scattered field from all cores in the array and

$$F_z^i(r_p,\phi_p)=\sum_{m=-\infty}^{\infty}a_{jm}^{E,H}J_m(k_2r_{jp})\exp\left(im\phi_{jp}\right)\exp\left(i\beta z_p\right) \tag{3.3}$$

is the field incident at p from all external sources. In (3.2), $H_m^{(1)}$ is the Hankel function of the first kind of order m used to describe outward propagating waves [42] and in (3.3) J_m is the Bessel function of the first kind. The terms r_{jp} and ϕ_{jp} are the polar coordinates describing the location of point p with respect to the center of core j in the *x-y* plane. The longitudinal fields within the core are expanded about a point p' according to

$$F_z^c(r_{p'},\phi_{p'})=\sum_{m=-\infty}^{\infty}c_{jm}^{E,H}J_m(k_1r_{jp'})\exp\left(im\phi_{jp'}\right)\exp\left(i\beta z_{p'}\right). \tag{3.4}$$

In (3.2), (3.3) and (3.4) $k_i=\sqrt{k_0^2n_i^2-\beta^2}$ is the transverse wave number, with $i=1$ in the core and $i=2$ in the cladding. The amplitude coefficients, $a_{jm}^{E,H}$, $b_{jm}^{E,H}$ and $c_{jm}^{E,H}$ as well as the modal propagation constants β are determined by applying the electromagnetic boundary conditions at the core cladding interface(s). The boundary conditions require that the tangential E and H field components, ϕ and z, are continuous at the core-cladding boundary, namely: $F_z^i+F_z^s=F_z^c$ and $F_\phi^i+F_\phi^s=F_\phi^c$. Solving these four equations (see Appendix A) leads to a relation between the coefficients of the locally incident field and the scattered field of core j,

$$\hat{b}_j=S_j\hat{a}_j \tag{3.5}$$

where S_j is the infinite square scattering matrix of core j. Equation (3.4) can be expanded as:

$$
\begin{aligned}
F_{zp} &= \sum_{m=-\infty}^{\infty} a_{jm}^{E,H} J_m(k_2 r_{jp}) \exp\left(im\phi_{jp}\right) \\
&+ \sum_{m=-\infty}^{\infty} b_{jm}^{E,H} H_m^{(1)}(k_2 r_{jp}) \exp\left(im\phi_{jp}\right) \\
&+ \sum_{\substack{k=1 \\ k\neq j}}^{N} \sum_{m=-\infty}^{\infty} b_{km}^{E,H} H_m^{(1)}(k_2 r_{kp}) \exp\left(im\phi_{kp}\right).
\end{aligned} \tag{3.6}
$$

In order to express the scattered fields from all N cores in a common coordinate system linked to core j, we use Graf's addition theorem for the Hankel function to obtain

$$
\begin{aligned}
H_m^{(1)}(k_2 r_{kp}) \exp\left(im\phi_{kp}\right) = \sum_{q=-\infty}^{\infty} H_{q-m}^{(1)}\left(k_2 r_{jk}\right) \exp\left(i\left(m-q\right)\phi_{jk}\right) \\
\times J_q(k_2 r_{jp}) \exp\left(iq\phi_{jp}\right).
\end{aligned} \tag{3.7}
$$

Substituting the right-hand side of (3.7) into (3.6) and solving for the coefficients gives

$$
\hat{a}_k = Q_k + \sum_{j\neq k} T_{k,j} \hat{b}_j \,. \tag{3.8}
$$

Here, Q_k is a column matrix determined by the incident field, F_z^i. The square matrix $T_{k,j}$ is given by

$$
T_{k,j,m,q} = \exp\left(i\left(q-m\right)\phi_{kj}\right) H_{m-q}^{(1)}\left(k_i r_{kj}\right). \tag{3.9}
$$

Substituting (3.8) into (3.5) and rearranging leads to the following linear system of equations

$$
\begin{bmatrix}
I & -S_1 T_{1,2} & \cdots & -S_1 T_{1,N} \\
-S_2 T_{2,1} & I & \cdots & -S_2 T_{2,N} \\
\vdots & \cdots & I & \vdots \\
-S_N T_{N,1} & \cdots & \cdots & I
\end{bmatrix}
\begin{bmatrix}
\hat{b}_1 \\ \hat{b}_2 \\ \vdots \\ \hat{b}_N
\end{bmatrix}
=
\begin{bmatrix}
S_1 Q_1 \\ S_2 Q_2 \\ \vdots \\ S_N Q_N
\end{bmatrix}. \tag{3.10}
$$

The propagation constants of the supermodes are found by setting the incident field to zero (i.e. $Q = 0$). Equation (3.10) may then be re-written as $\mathbf{M}(\beta)\cdot\hat{b} = 0$. The

infinite harmonics in the preceding equations are truncated from $(-\infty, -\infty+1, \cdots, \infty)$ to $(-M, -M+1, \cdots, M)$, giving a square matrix $\mathbf{M}(\beta)$ of size $2N(2M+1) \times 2N(2M+1)$. The modes are then determined by numerically searching for the zeros of the determinate of $\mathbf{M}(\beta)$. The resulting values for β are then back substituted into (3.10) to find the $\hat{b}$ coefficients. It is then possible to solve for the remaining coefficients and fields of the array.

3.2 Modeling Multicore Fibers and Waveguide Arrays

3.2.1 Coupling Analysis

Once the supermodes are known, the coupling characteristics are given by the superposition of supermodes as they propagate in the z direction [47]. The transverse electric field distribution of odd modes in the νth core is given by:

$$E_t^{(k)}(z) = \left(a_{r\nu} \sin\frac{2\pi\nu k}{n} + a_{\theta\nu} \cos\frac{2\pi\nu k}{n} \right) e^{-j\beta_k z} \qquad (\nu = 1, 2, \cdots, n) \tag{3.11}$$

and

$$E_t^{(k)}(z) = A_k a_{\theta 0} e^{-j\beta_k z} \qquad (\nu = 0) \tag{3.12}$$

where $a_{r\nu}$ and $a_{\theta\nu}$ are the unit vectors in the r and θ directions in the νth coordinate respectively, k is the mode number, β_k is the propagation constant of mode k and A_k is the ration of the HE_{11} mode vector amplitude in the center core to that in one of the surrounding cores. The field can then be described by the superposition of the eigenmode fields as:

$$E_t(z) = \sum_k \alpha_k E_t^{(k)}(z) \tag{3.13}$$

The α_k coefficients are determined by the coupling conditions, which, for the cases investigated in this dissertation, are for center core $(\nu = 0)$ coupling only. Using the weakly guiding approximation, the transverse magnetic fields are determined from

$$\left|E_t^{(k)}(z)\right| = \sqrt{\mu_0/\varepsilon}\left|H_t^{(k)}(z)\right|. \tag{3.14}$$

3.3 Tailoring modal power distribution in waveguide arrays

In this section, waveguide arrays comprising three, four, five, six and seven cores, as illustrated in Figure 3-2, are analyzed. The arrays are similar in that they all have equally-spaced outer cores with a common central core. We investigate these arrays with the central core as a key parameter of interest; by adjusting its properties we show how the near field mode profile can be tailored. We determine the properties of the central core required to achieve an equal power distribution among all cores of the array – a result particularly interesting to power scaling waveguide arrays. Once the propagation constants are obtained via the SMM, the amplitude coefficients and electromagnetic fields of the supermodes are calculated. The effect of parameters such as core diameter and core spacing on the behavior of the multicore waveguides is determined.

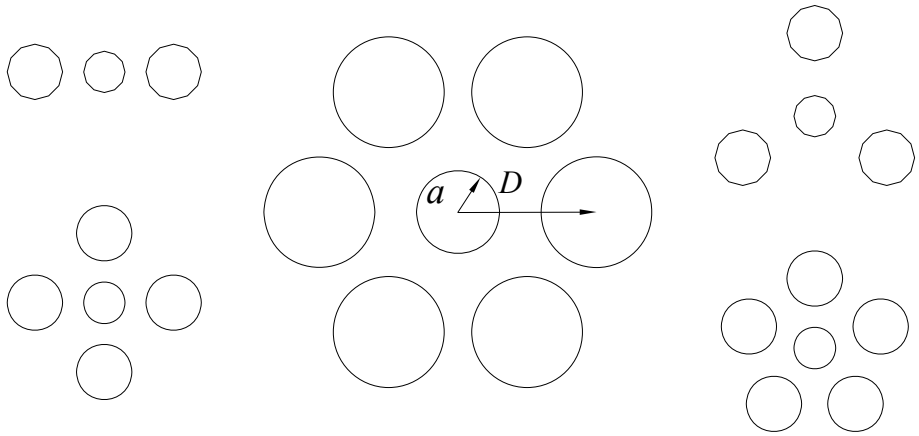

Figure 3-2. Waveguide arrays with common central cores

For all cases, the outer core radius is $a = 3.5\,\mu\text{m}$ and all cores are spaced $D = 10.5\,\mu\text{m}$ (center-to-center) from the center core. The wavelength is λ=1.06 μm and the waveguides have a step-profile refractive index with a core-cladding difference of Δn = 2×10^{-3}. The central core diameter is varied in the simulations to give a central core V-number (V_c) in the range from $V_c = 0.3161$ to 2.3706, where

$$V_i = k_o a_i \left(n_1^2 - n_2^2\right)^{1/2}. \tag{3.15}$$

The V-number of the outer cores was held constant at $V_o = 1.5804$. Since $V_i < 2.405$ for all cores, each of the individual waveguides therefore supports a single guided mode. A total of seven harmonics, $(-M, -M+1, \cdots, M) = (-3, -2, \cdots, 3)$, were used in the calculations.

The normalized propagation constants of the supported supermodes are plotted as a function of V_c in Figure 3-3 through Figure 3-7 for each of the waveguide arrays. Due to the reflection and rotational symmetries of the arrays, the supermodes can all be classified into the C_{nv} point group, where *n=N-1* [48]. The modes they support are

therefore either non-degenerate or doubly degenerate. Furthermore, each array supports n+1 odd and n+1 even coupled HE_{11} modes for a total of 2(n+1) supermodes. For simplicity, we label the modes with their LP_{mn} mode designations and degree of degeneracy in Figure 3-3 through Figure 3-7. As V_c increases, the field in the central core overlaps less with the field in the surrounding cores, resulting in weaker coupling. As a result, the supermode propagation constants tend to increase as the field is more confined to the center core. This effect is most pronounced for the supermodes which have non-zero field in the central core, namely the fundamental, LP_{01} supermode and the LP_{21} (LP_{02}) supermodes in the 3- and 4-core (5-, 6- and 7-core) waveguides. In the case of the 6- and 7-core waveguides, the propagation constants of the LP_{21} (also LP_{31} in the 7-core array) and LP_{02} modes overlap at discrete frequencies as the LP_{02} propagation constant increases with increasing V_c.

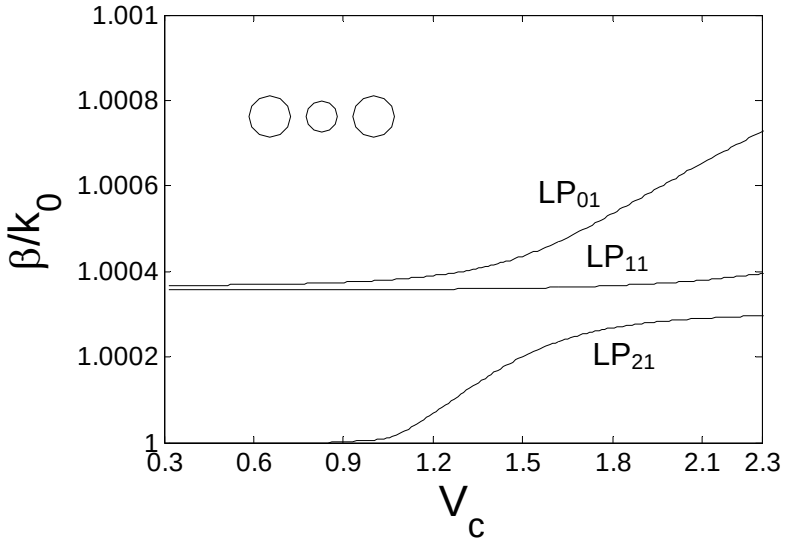

Figure 3-3. Normalized propagation constants as a function of the central core V-number (V_c) for the 3-core waveguide. The V-number of the outer cores is $V_o = 1.5804$

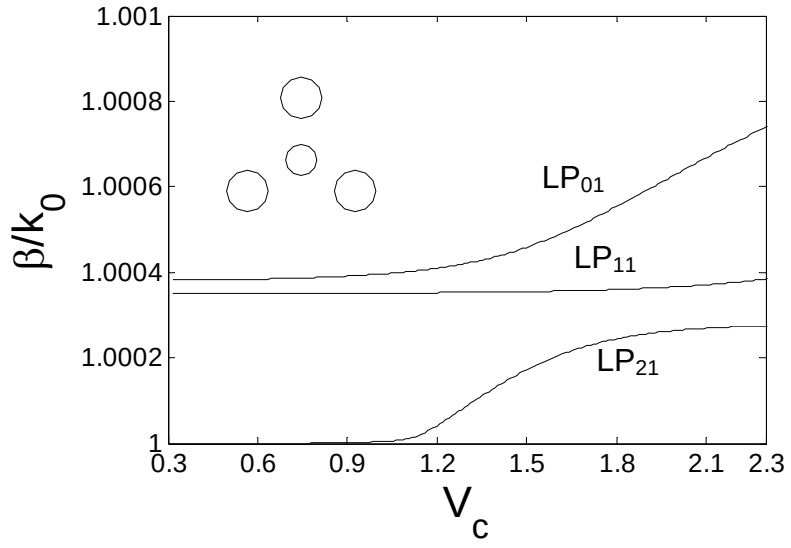

Figure 3-4. Normalized propagation constants as a function of the central core V-number (V_c) for the 4-core waveguide. The V-number of the outer cores is $V_o = 1.5804$

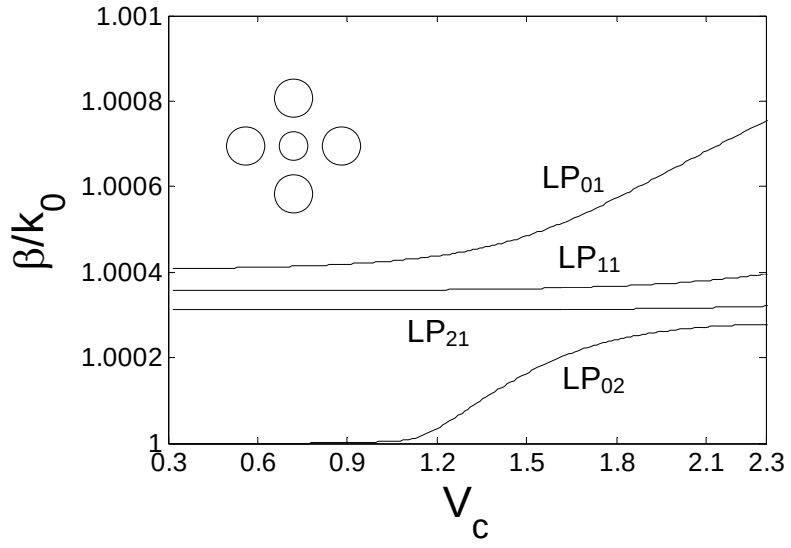

Figure 3-5. Normalized propagation constants as a function of the central core V-number (V_c) for the 5-core waveguide. The V-number of the outer cores is $V_o = 1.5804$

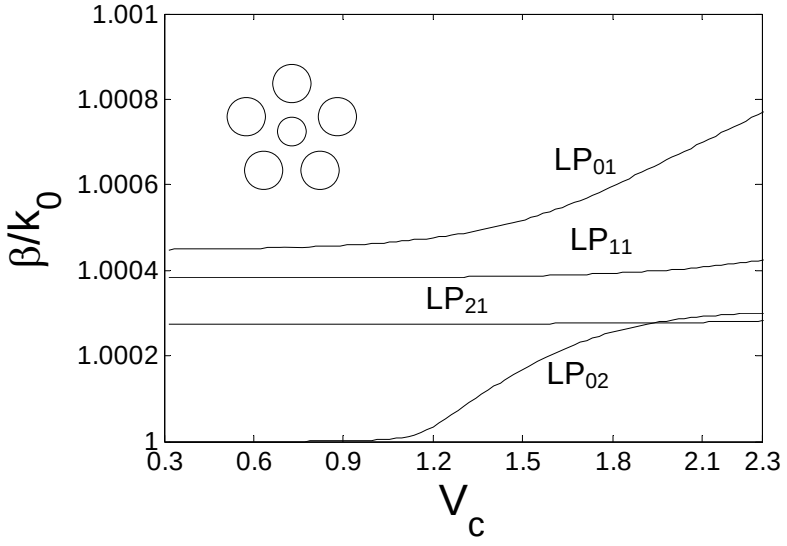

Figure 3-6. Normalized propagation constants as a function of the central core V-number (V_c) for the 6-core waveguide. The V-number of the outer cores is $V_o = 1.5804$

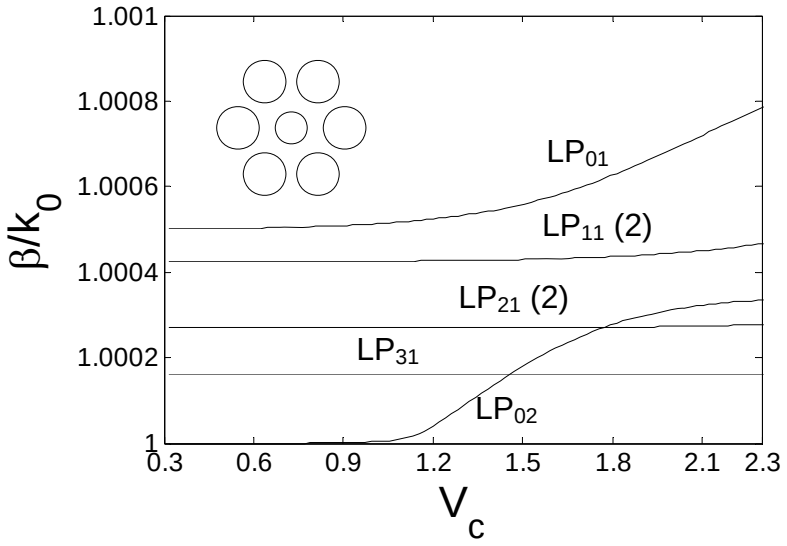

Figure 3-7. Normalized propagation constants as a function of the central core V-number (V_c) for the 7-core waveguide. The V-number of the outer cores is $V_o = 1.5804$

Next, we examine how the power distribution of the array varies with V_c. In order to determine the optimum value of V_c for power scaling, we plot the normalized power in each core against V_c (Figure 3-8) for the LP_{01} mode and locate the V_c value at which all cores have equal power (for equal *intensity* among all cores, the V_c values are slightly smaller due to the smaller center core area.). The crossing points for the 3-, 4-, 5-, 6- and 7-core arrays are V_c = 1.4671, 1.3882, 1.3487, 1.3372 and 1.3576 respectively. As V_c is increased beyond this value, the central core power continues to increase and the power in the outer cores drops. Arrays with all identical cores have V_c to the right of this crossing point and are power limited by the central core. Conversely, arrays with V_c to the left of the crossing point are power limited by the outer cores. The power distributions in supermodes with zero center-core fields are only slightly affected by adjusting V_c.

The effect of V_c on the near-field mode profile is illustrated in Figure 3-9 which shows the normalized LP_{01} mode electric field for each of the waveguide arrays for three values of V_c. In each case, the plot on the left is for $V_c = 0.3161$, the middle plot is for V_c equal to the optimum value required to give an equal power among all cores for the in-phase supermode and the plot on the right is for $V_c = 2.3706$. The outer cores all have $V_o = 1.5804$.

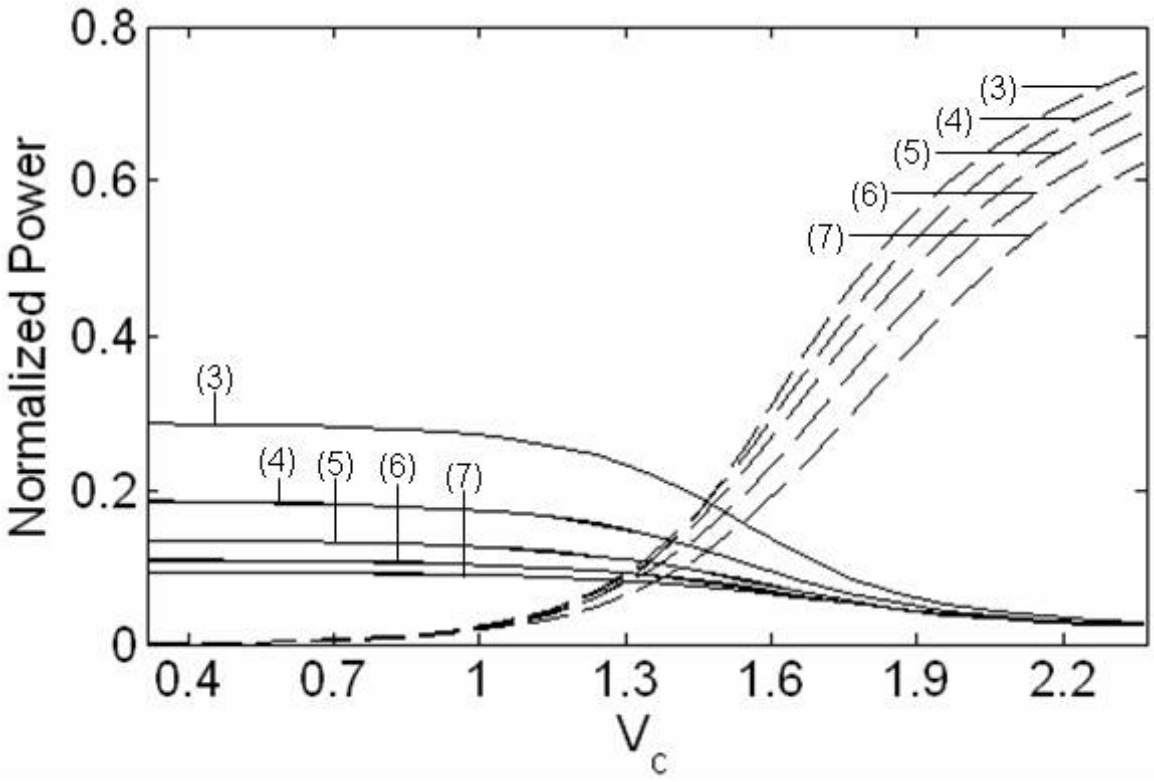

Figure 3-8. LP_{01} supermode normalized power as a function of V_c for the multicore arrays in Figure 3-2. The number of cores is displayed in parentheses. Solid lines represent outer cores, dashed lines represent center cores. All outer cores have V_o=1.5804.

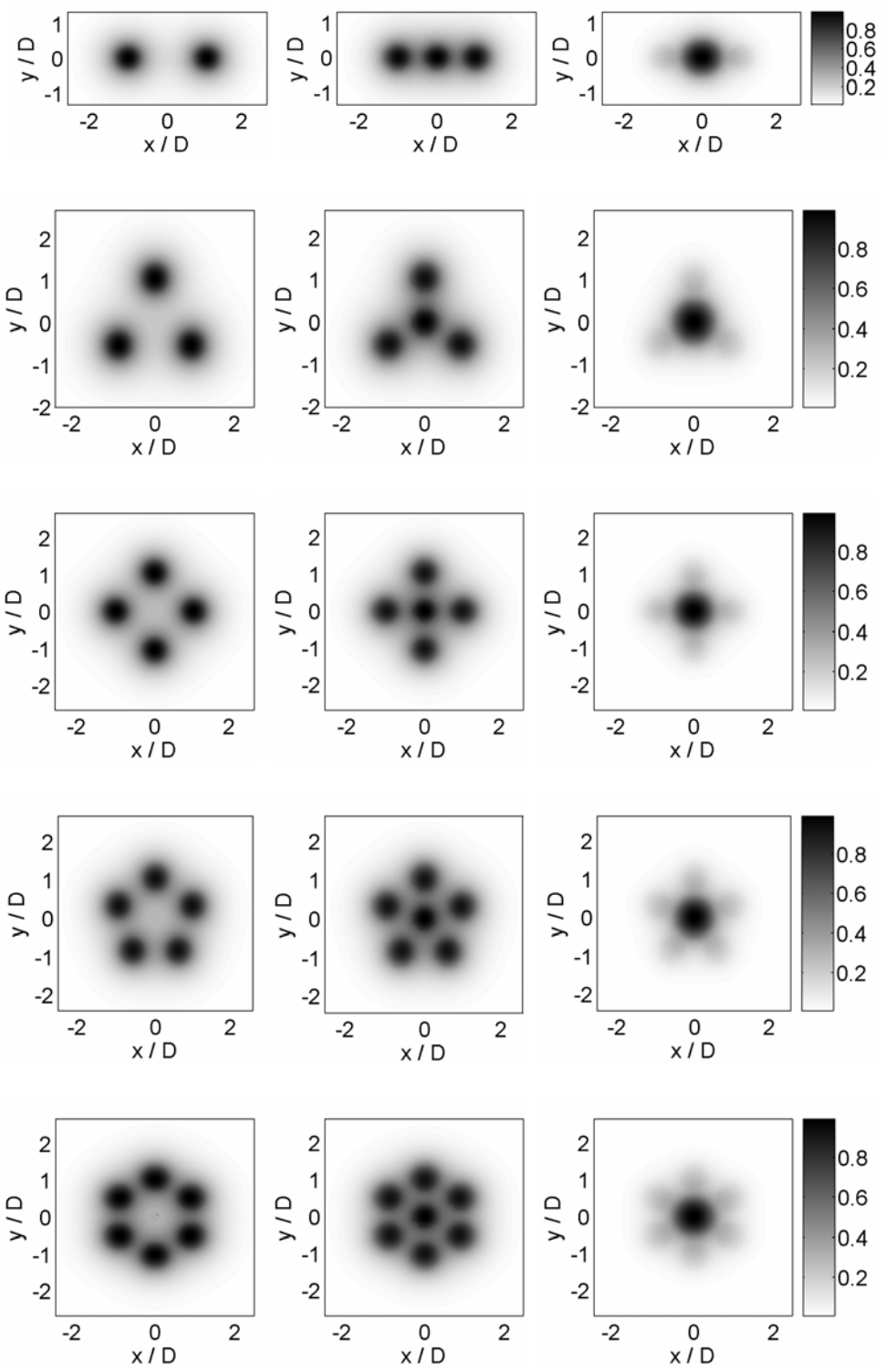

Figure 3-9. Normalized electric field plots of the fundamental, in-phase (LP_{01}) supermode for the waveguides in Fig. 2. From left to right: V_c=0.3161, optimum value and 2.3706 respectively. V_o=1.5804 for all cases.

3.3.1 **Analysis of 7-core Array**

In this section, we analyze the 7-core waveguide in greater detail, including the behavior of all supermodes as a function of V_c. We also investigate the role of core spacing and dispersion properties of the array. The electric fields of the four higher-order supermodes (six LP modes with two degenerate doublets) for the 7-core structure are plotted in Figure 3-10 for the same three cases of V_c as in Figure 3-9. As predicted in Figure 3-7, the field distributions of the LP_{01} and LP_{02} supermodes which have non-zero field in the center core, are sensitive to changes in V_c whereas the remaining supermodes are relatively unaffected.

The effect of core spacing on the supermodes of the 7-core array is plotted in Figure 3-11 for two cases: (1) with all cores identical and (2) with $V_c = 1.3576$ (the crossing point in Figure 3-8). As in Figure 3-10, the supermodes with zero field in the center core are only slightly affected by altering the central core properties and are nearly degenerate with corresponding supermodes in the identical core case. In general, as the core separation increases and evanescent coupling decreases, the propagation constants converge to that of an individual outer-core waveguide. For case (2), however, the LP_{02} mode propagation constant converges to a value equal to that of a single center-core waveguide (β_c), since the field is more confined to the center core with increasing V_c in this case.

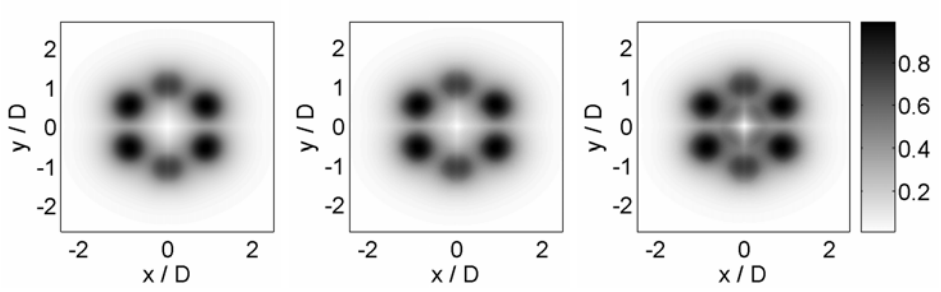

(a)

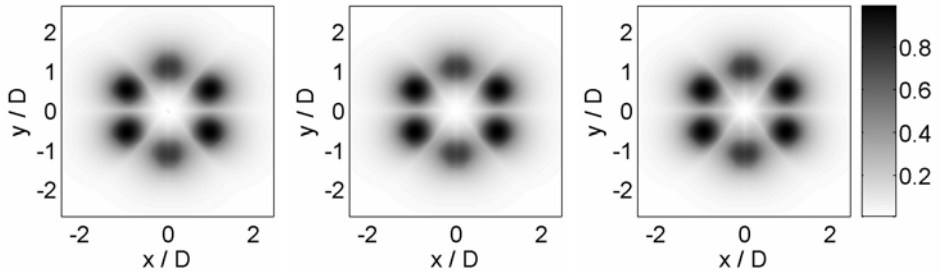

(b)

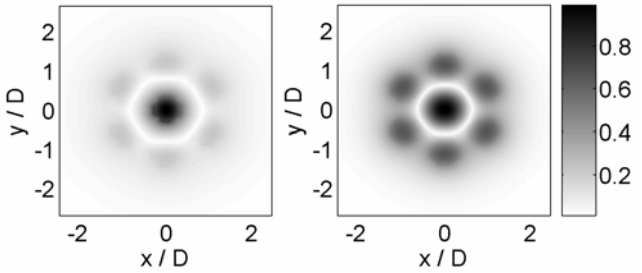

(c)

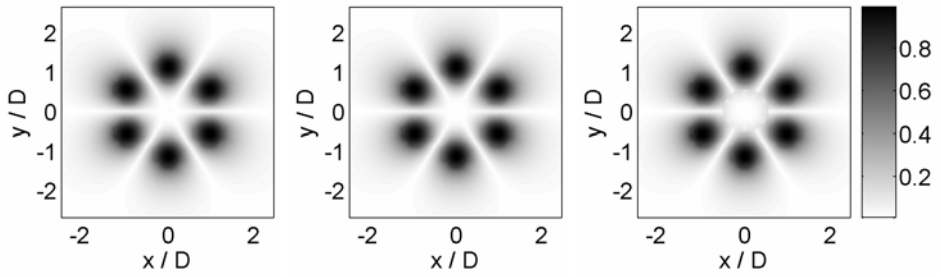

(d)

Figure 3-10. Normalized electric field plots of the higher order supermodes for the 7-core structure; from left to right: V_c=0.3161, 1.3576 and 2.3706 respectively. V_o=1.5804 for all cases. (a) LP_{11} (b) LP_{21} (c) LP_{02} (V_c=0.3161 is beyond the modal cutoff) (d) LP_{31}

The dispersion properties of the 7-core array, for the same two cases: (1) with identical cores and (2) with optimum $V_c = 1.3576$ (at a wavelength of 1.06μm), in the wavelength range from 0.7μm to 1.6μm, are plotted in Figure 3-12. Again, the supermodes with zero field in the center core are nearly degenerate with the identical core case. Also, the supermodes with non-zero center core field, namely the LP_{01} and LP_{02} modes, have reduced propagation constants for case (2) due to the presence of the center core with smaller V-number.

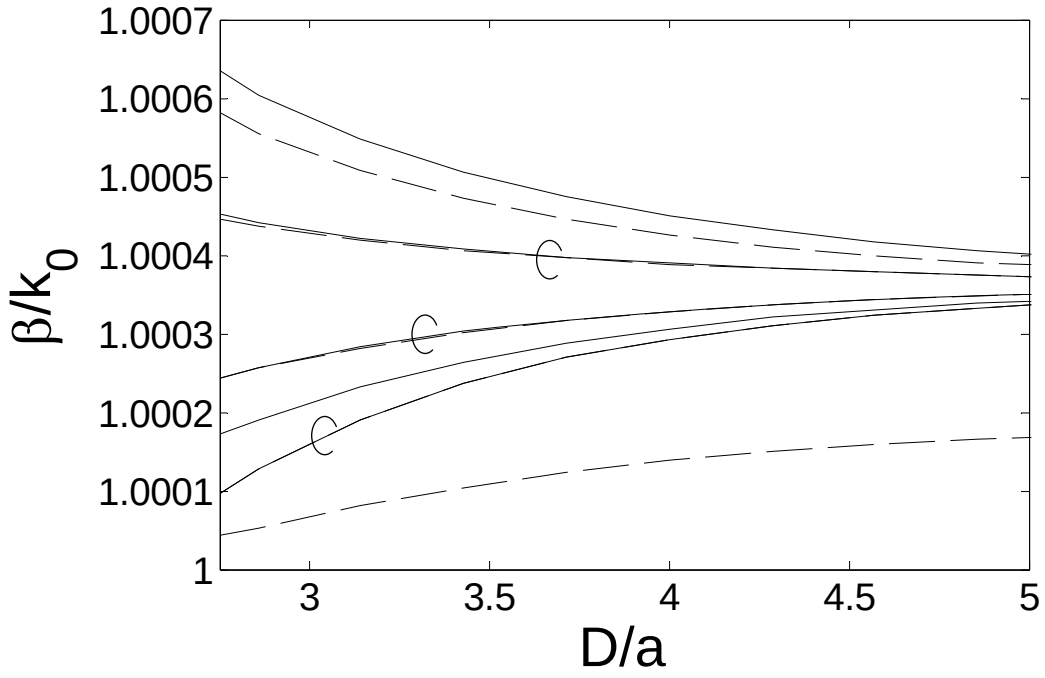

Figure 3-11. Normalized propagation constant versus core spacing for case (1): identical cores (solid line) and case (2): V_c=1.3576 (dashed line). Overlapping modes from each case are circled.

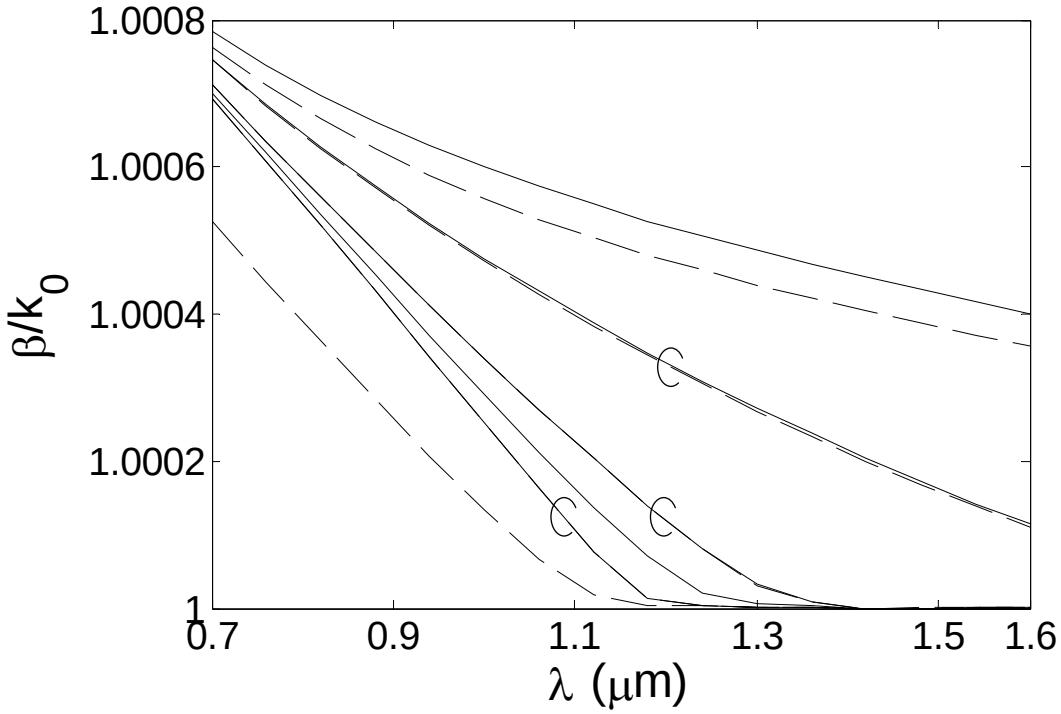

Figure 3-12. Dispersion for the 7-core array with identical cores (V=1.5804 at λ=1.06μm, solid line) and with central core V_c=1.3576 at λ=1.06μm and outer core V_o=1.5804 at λ=1.06μm (dashed line). Overlapping modes from each case are circled.

3.3.2 **Conclusions**

We have determined the propagation constants and electromagnetic fields of evanescently coupled waveguide arrays comprising three, four, five, six and seven cores with a common central core using the SMM. We show that all cores in an array can have equal power in the LP_{01} supermode if the V-number of the central core is properly selected. We have also investigated the 7-core array in greater detail by determining electromagnetic fields for higher order supermodes and comparing the dispersion characteristics and effect of core spacing for arrays with all identical cores and those with non-identical central cores. For 7-core arrays with smaller V_c, the supermodes with non-

zero center core fields (the LP_{01} and LP_{02} modes) have lower propagation constants compared to the identical core case, due to the presence of the field in the center core with reduced β. In fact, the dispersion characteristics show that the LP_{02} mode β approaches β_c as the core separation is increased, while the remaining supermode propagation constants approach β_o. These results can be used to tailor the near field of waveguide arrays with common central cores. With the proper mode discrimination to select the LP_{01} supermode in an array with optimized V_c, a significant increase in array power handling could be achieved. The methods described herein could also be applied to devices with active cores for more efficient use of the gain medium. These results are easily scalable to larger arrays and multicore photonic crystal waveguides.

3.4 Modeling Photonic Crystal Fibers

The SMM is also well suited for modeling photonic crystal fibers [43-45]. The method is essentially the same as for the case of multicore fibers with the high-index cores replaced with low index (air) cores. As an example, the SMM is used to determine the fundamental mode of a PCF with 36-holes in a hexagonal arrangement with an air hole missing in the center of the array as shown on the left in Figure 3-13. The radius of each hole is 1.9 μm, the pitch (center-to-center hole spacing) is Λ = 13 μm and the hole and cladding refractive indices are 1.000800 and 1.453888 respectively. The effective index of the fundamental mode was determined to be 1.453583 at a wavelength of 775 nm. The simulated power distribution of the fundamental supermode is shown on the right in Figure 3-13.

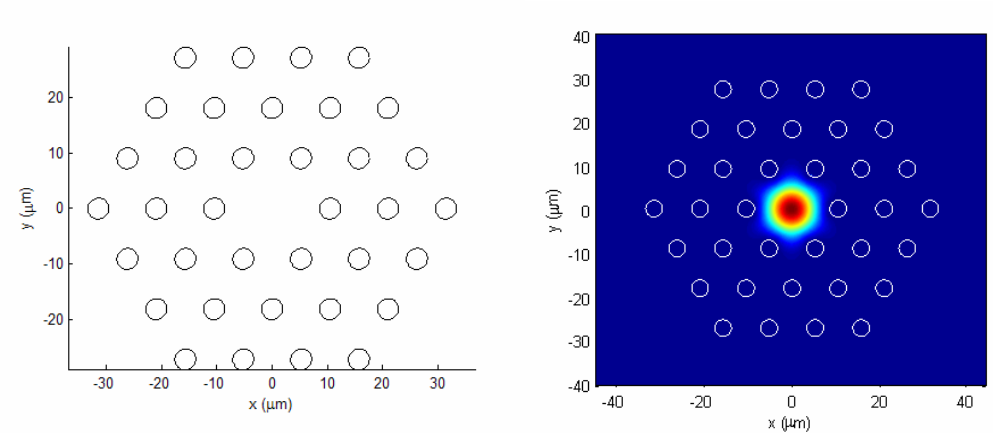

Figure 3-13. Simulated PCF. Left: hole geometry, Right: fundamental mode power distribution simulated using SMM

4 Femtosecond Pulses in Specialty Fibers

In this chapter, three types of specialty fibers are investigated for ultrashort pulse delivery: a solid-core photonic crystal fiber (PCF), a hollow-core photonic crystal fiber (HC-PCF) and silver-coated hollow silica waveguide (HSW). All three fibers have large mode-areas (LMA), however, the mechanisms of light confinement and light-matter interactions are unique for each case. The output from each of the fibers is characterized in terms of the beam profile, spectra, temporal dynamics and energy transmission as a function of input pulse energy.

4.1 Solid-Core Photonic Crystal Fiber

Photonic crystal fiber (PCF) was introduced by Knight *et al.* in 1996 [6]. The cladding is formed by a periodic array of air holes that run the length of the fiber and has an effective-index that is determined by the air-filling fraction and hence the hole diameter and spacing (pitch). The core in a solid-core PCF is created by omitting at least one air hole, forming a localized region that effectively has a higher index than the rest of the structure. This effective-index difference is a strong function of wavelength, since at longer wavelengths the modal field extends further into the holes, thereby reducing the

effective cladding index [49]. This property provides novel functionality including single-mode propagation at any wavelength within the transparency window of fused silica [50] and anomalous GVD at visible and infrared wavelengths [51]. Of special interest to ultrashort pulse delivery is the fact that the core size in PCF can be scaled to large diameters and still remain single-mode [52]. This is possible because for a PCF, the number of guided modes is independent of the ratio of the core radius to the optical wavelength as is the case in conventional fibers. For a PCF, the number of guided modes depends only on the ratio of the air hole diameter to the spacing between the holes. A PCF will support a single-mode for a hole-to-pitch ratio < 0.43. The performance of large core PCF is limited by bend loss, which becomes impractical for very large cores and tight bends.

Previously, Knight and co-workers have fabricated and tested a 22.5μm core PCF and confirmed single-mode guidance [52]. They estimated its bend radius for catastrophic loss of power to be ~ 50 cm at 458 nm and ~ 4 cm at 1550 nm. While the bend losses are much higher than for conventional single-mode fibers, the 22.5um core diameter represents an increase of approximately 20 times the cross-sectional area, reducing the intensity in the core by the same factor. This provides the possibility of much higher power pulse propagation compared to standard single-mode fibers.

The LMA solid-core PCF used in this experiment was obtained from Crystal-Fibre A/S in Denmark (Figure 4-1). The fiber has a triangular lattice of 3.8 μm diameter air holes with a center-to-center spacing (pitch) of 13 μm. A single air hole is omitted in the center of the structure to form a pure silica core with a diameter of 23±1 μm. This core diameter is approximately 3 to 5 times the diameter of a conventional single-mode

fiber, increasing the nonlinear threshold by approximately 20. The numerical aperture (NA) for the fiber is 0.02, which is about 5 to 7 times smaller than for conventional single-mode fibers. This is due to the small air filling fraction, and therefore small index differential, between the core and the cladding.

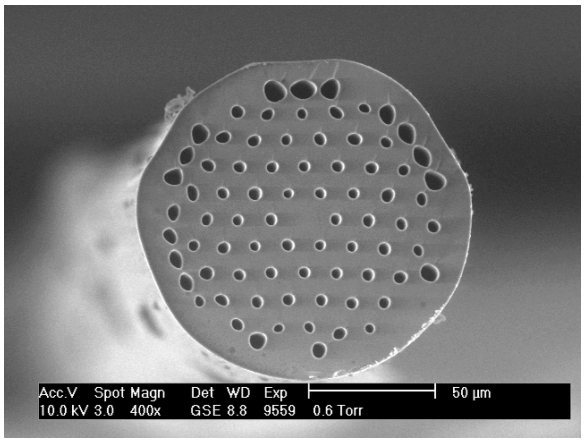

Figure 4-1. SEM image of solid-core PCF

4.1.1 **Scattering Matrix Method Modeling of Real PCF**

The SMM was used to model the PCF in Figure 4-1. A threshold image of the scanning electron micrograph was obtained to reveal only the holes of the fiber as shown on the left in Figure 4-2. An algorithm was then used to extract the minimum circle diameter that completely encloses each hole as well as the centroid of each hole for input into the SMM. The retrieved holes are plotted on the right in Figure 4-2. Recall that the SMM assumes that a cylinder with cross-section C_j is enclosed by a circle D_j with center O_j and that the diameter of D_j is the smallest possible diameter that includes C_j [42]. The hole and cladding refractive indices used in the simulation were 1.000800 and 1.453888 respectively. The SMM gave an effective index of 1.453706 for the fundamental mode at

a wavelength of 775 nm. Compared to the ideal, as-designed PCF that was modeled in section 3.4, which had an effective index of 1.453583, the model of the actual fiber is within 0.009%. The near-field output beam profile of a 710 mm long section of PCF with 30 nJ, 135 fs input pulses and the simulated output from the SMM are plotted in Figure 4-3 and are in good qualitative agreement.

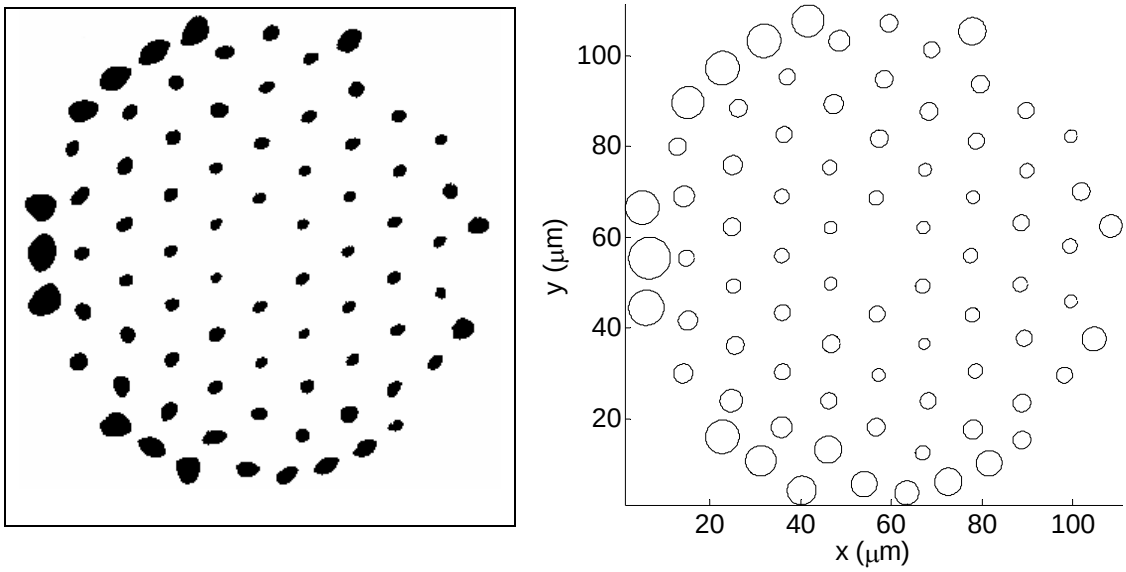

Figure 4-2. Left: Threshold image of Figure 4-1. Right: Retrieved 'holes' from threshold image.

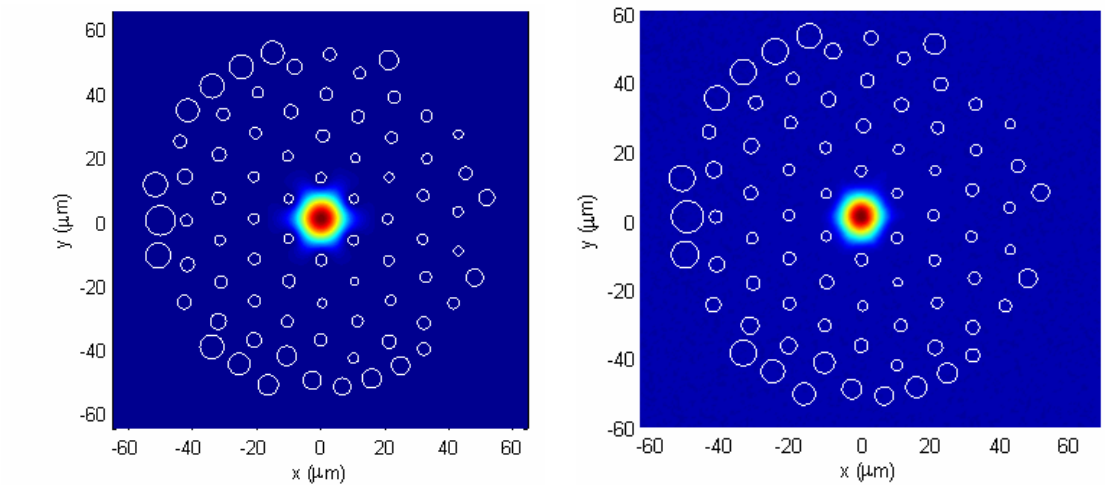

Figure 4-3. Output from real PCF Left: simulated output using the SMM, Right: experimental output from 710 mm long fiber with 30 nJ input pulses. White circles indicate air hole positions.

4.1.2 Characterization

4.1.2.1 Experimental Setup

The experimental setup for characterizing the solid-core PCF is illustrated in Figure 4-4. Pulses from a Ti:Al_2O_3 regenerative amplifier with the properties listed in Table 4-1 and energies ranging from 30 nJ to 2000 nJ were endfire coupled into the PCF using a 150 mm focal length lens. The beam was spatially filtered prior to the lens using a pinhole to produce an Airy pattern and an iris in the far field to select the central Gaussian lobe. The pulse energy was adjusted using a half-waveplate and polarizer and the input polarization was linear along the *x*-axis. An adjustable beam expander was used to closely match the fiber numerical aperture. The ultrashort pulses were coupled to either a 650 mm or a 710 mm long section of PCF that was loosely draped between two fiber holders. The fiber bend radius was estimated to be 4 m at each fiber holder. The CW beams from a 633 nm HeNe laser and a 532 nm diode-pumped solid-state laser were also collinear with the ultrashort pulses to aid in alignment of the optical components and for

excitation of the fibers and waveguides at other wavelengths in the visible regime. The wavelength could easily be chosen by selectively blocking the unwanted beams. The near-field fiber output was coupled into a 20× microscope objective and observed using a beam profiling system (Spiricon) and spectrometer with resolution of 0.29 nm (Ocean Optics). The power was measured before and after the fiber using a silicon photodetector (Newport 818-SL). Temporal pulse dynamics were monitored using a home-built interferometric autocorrelator with a GaP photodiode as a nonlinear detector. The autocorrelator signal was coupled to a lock-in amplifier, digitized and recorded on a personal computer.

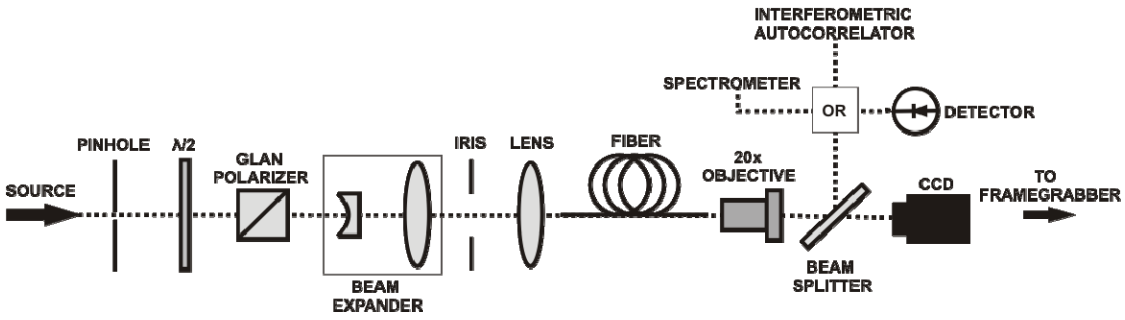

Figure 4-4. Experimental setup for characterizing the solid-core PCF

Table 4-1. Output pulse properties of Ti:Al_2O_3 regenerative amplifier

Pulse Width, τ_{FWHM}	**110-135 fs**
Wavelength, λ_0	**780 nm**
Repetition Rate, R_p	**1 kHz**
Pulse Energy, E_p	**< 1 mJ**

4.1.2.2 *Output Beam Profiles*

Near-field output beam profiles were recorded as a function of input pulse energy. No significant differences were noted over the entire energy range tested. Beam profiles at output energies of 2.6 nJ and 178 nJ in the vicinity of the core are shown in Figure 4-5. The beam output from the fiber appears to be single-mode even under slight bending; in fact, beam profiles for delivery of 532 nm and 633 nm light also look very similar (data not shown), suggesting that the fiber indeed has a large single-mode bandwidth.

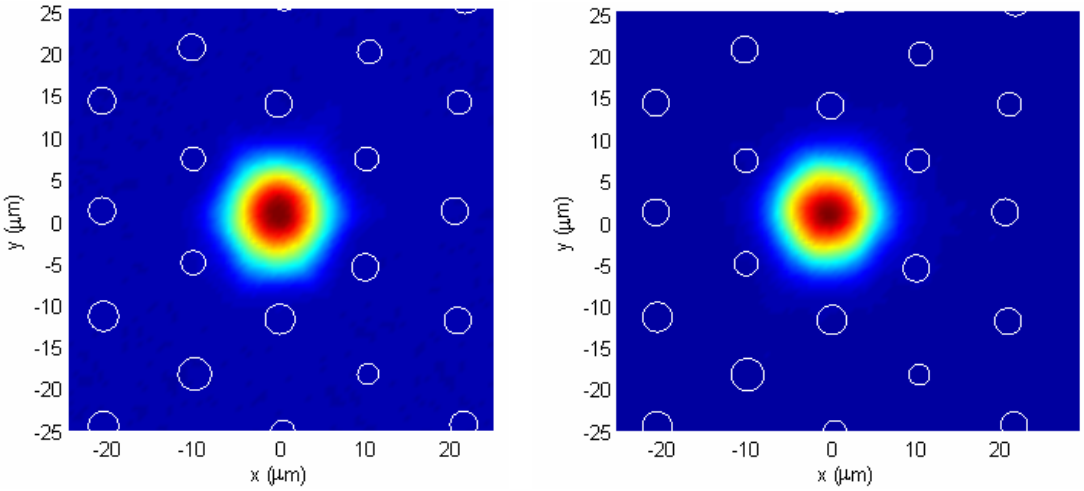

Figure 4-5. PCF near-field beam profiles. Left: 2.6 nJ output energy, Right: 178 nJ output energy

4.1.2.3 *Temporal Dynamics*

An interferometric autocorrelation of the input pulse, taken prior to the 150 mm coupling lens, is shown in Figure 4-6. In general, an interferometric autocorrelation signal should exhibit an 8:1 (peak:wing) ratio. In this case the ratio is approximately 6.5:1, likely due to an imbalance in the pulse energies in the two arms of the autocorrelator. An 8:1 ratio has been verified in autocorrelations of pulses that were not spatially filtered, so the difference is likely due to slight misalignment of the spatially-filtered pulses in the

autocorrelator. Furthermore, the shape of the autocorrelation of the spatially-filtered pulses is similar to that of the un-filtered pulses, but appears to be slightly broader. The autocorrelation full-width at half-maximum (FWHM) is 150 fs. In order to determine the actual FWHM pulse duration, the autocorrelation FWHM must be multiplied by a proper scale factor that is dependent on pulse shape. The input pulse duration for this case was estimated to be 110 fs, assuming a Gaussian pulse shape. It should be noted, however, that recent a study by Zeek *et. al.* in which frequency-resolved optical gating (FROG) was used to determine actual scale factors, showed that the assumption of simply a Gaussian or $sech^2$ pulse shape could result in measurement errors on the order of 25%, especially for complex pulses [53].

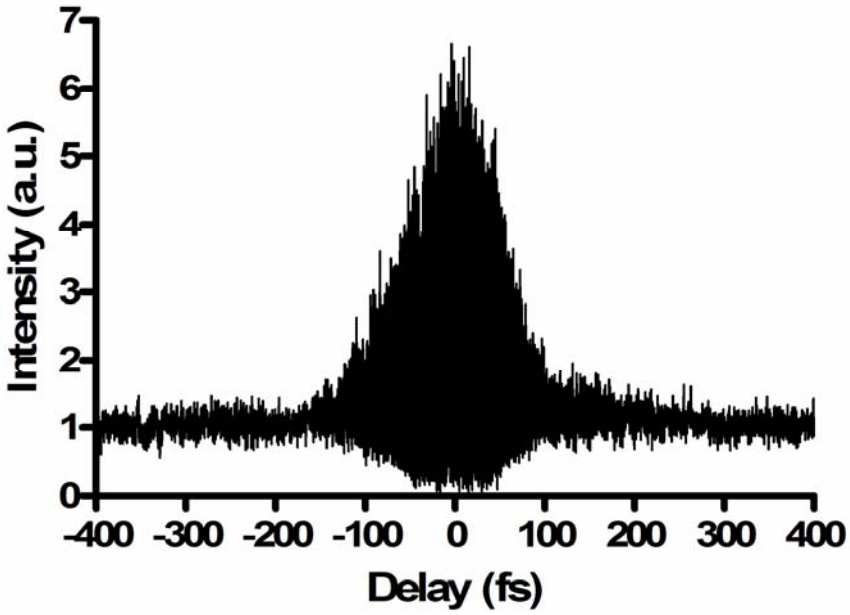

Figure 4-6. Interferometric autocorrelation of input pulse

Interferometric autocorrelations of the output pulses from the 650 mm long PCF for input pulse energies in the range from 100 nJ to 1000 nJ are plotted in Figure 4-7.

The output pulse autocorrelations show complex structure even for those recorded at the lowest input energy of 100 nJ. In fact, every autocorrelation over the entire range of energies recorded exhibits a widening of the autocorrelation envelope combined with a narrowing of the interference pattern, which is indicative of induced chirp. This chirp can be attributed to self-phase modulation (SPM) which is also responsible for the spectral broadening and oscillatory structure observed in the spectra in Figure 4-8. The pulse duration is further increased by normal group velocity dispersion (GVD), which has a more pronounced contribution due the significantly broadened spectrum. Additionally, side-lobes appear for input (output) pulse energies between 200 nJ (90 nJ) and 300 nJ (130 nJ). Similar side-lobes were observed in an experiment by Ouzounov *et al.* when they coupled 100 fs, 1.25 nJ pulses into a 15 μm core solid-core PCF [54]. Since their fiber had a hole-to-pitch ratio of 0.6, they attributed the peaks to higher-order mode transmission. In this case, however, the fiber supports only a single-mode and no changes in the output beam profiles were noted near the input energies at which the side-lobes occurred. The side-lobes that appear are more likely due to the steep, highly structured spectrum that results from nonlinearities [55].

4.1.2.4 ***Output Spectra***

Output spectra for the 650 mm long PCF were taken at input energies over the range from 100 pJ to 1000 nJ. These spectra are plotted in Figure 4-8. A composite, interpolated spectrum is shown in Figure 4-10. At 100 pJ (dashed line in Figure 4-8), the output spectra was similar to the input spectra. However, by 20 nJ, spectral broadening was more pronounced and modulation of the spectra had occurred due to SPM (Figure

4-9). As the input pulse energy was increased above 100 nJ, the spectrum continued to broaden and exhibited significant modulation. Above an input pulse energy of 400 nJ, the fiber had a faint red/orange glow which could be seen with the unaided eye. By the transmission peak at 550 nJ input energy, the spectrum had broadened to more than 150 nm in the wings. For the most part, spectral broadening ceased for input pulse energies above 500 nJ, due to the onset of fiber damage and subsequent reduction in transmitted energy and degree of SPM.

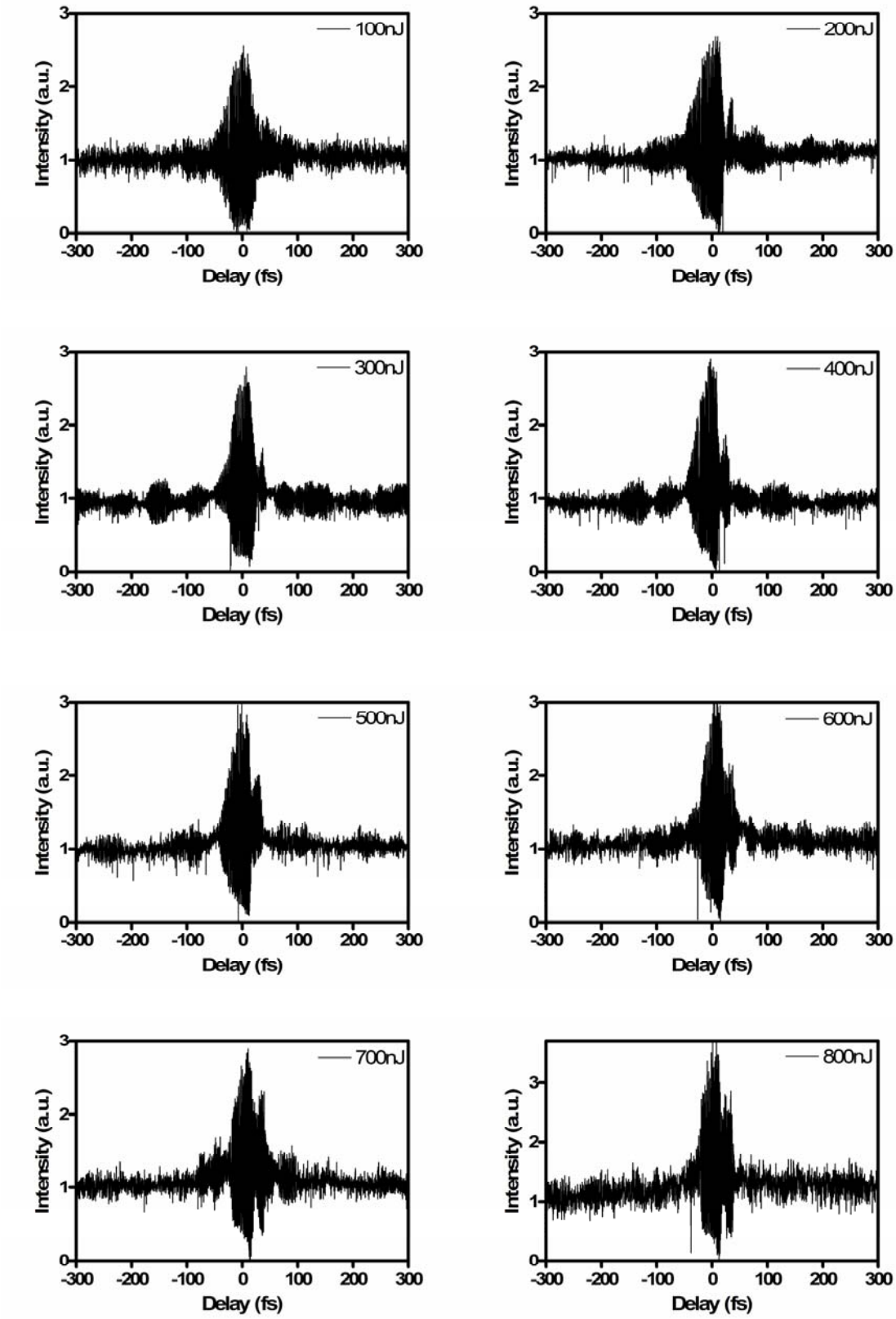

Figure 4-7. Interferometric autocorrelations of PCF output for given input pulse energies

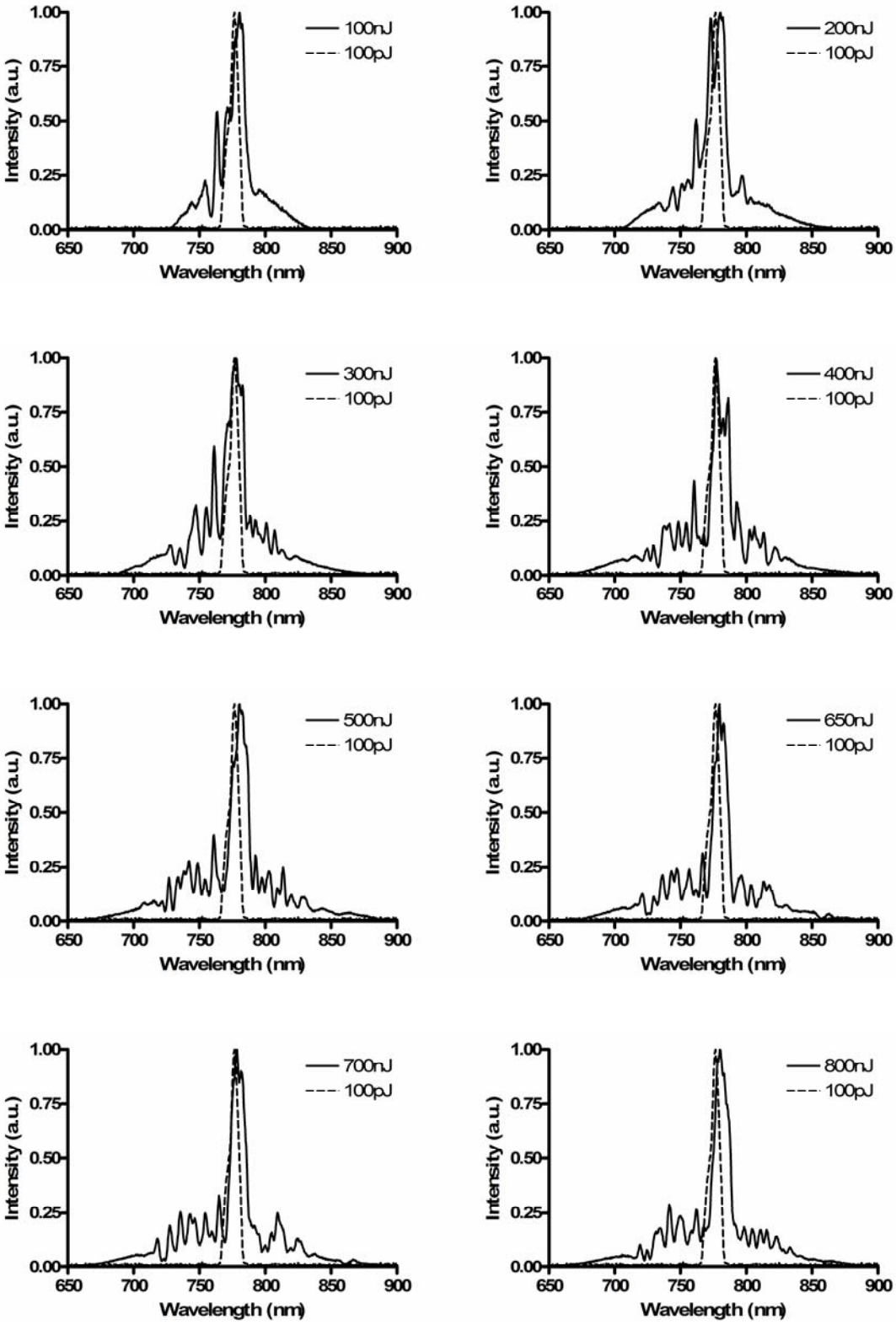

Figure 4-8. Output spectra from solid-core PCF with given input pulse energies

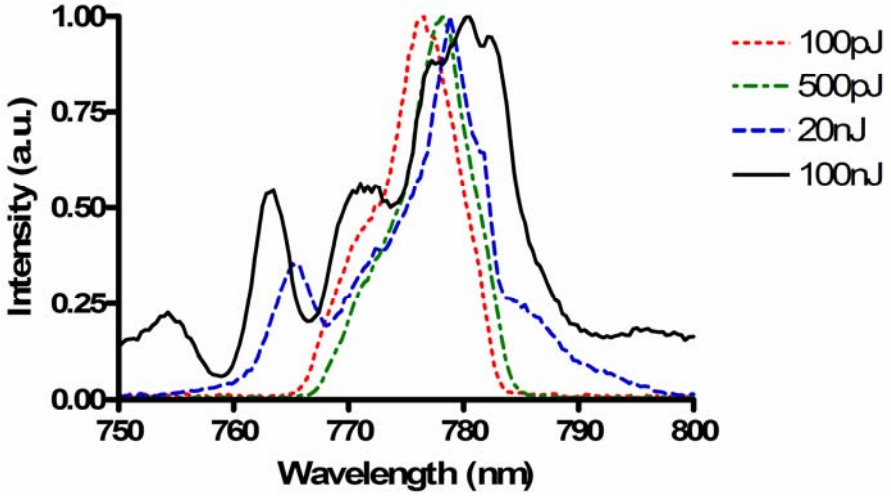

Figure 4-9. Solid-Core PCF output spectra with input energies below 100 nJ

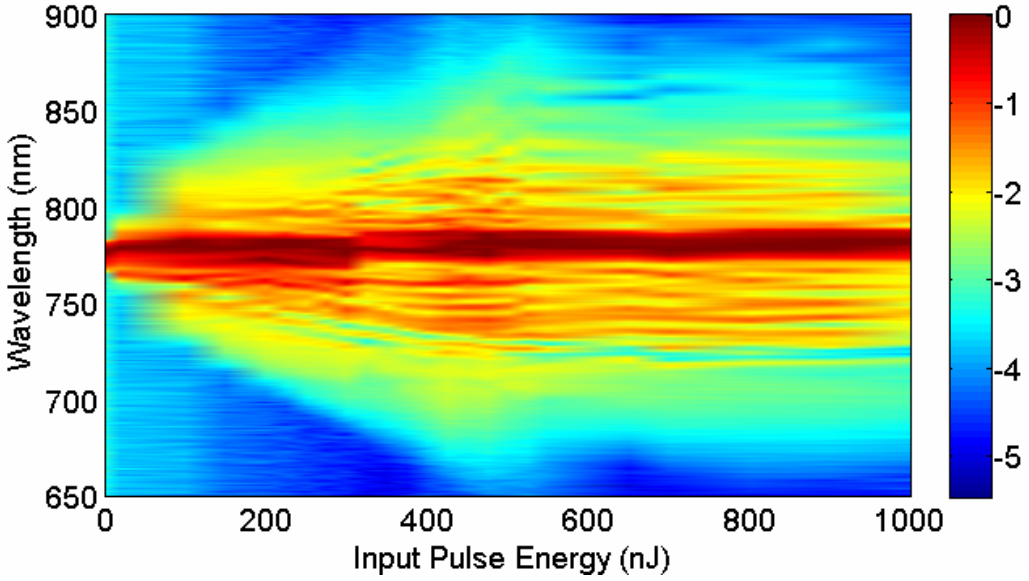

Figure 4-10. Interpolated spectra for the 650 mm long, solid-core PCF (logarithmic scale intensity)

4.1.2.5 ***Transmission***

The transmission as a function of input pulse energy for the 650 mm long fiber is plotted in Figure 4-11. In order to determine the input pulse energy that resulted in fiber damage, the transmitted pulse energy was measured in an iterative fashion where the previous (lower energy) point was re-measured after each successive energy increase. If the previous point was not the same as the initial measurement, then it was assumed that damage had occurred and transmission measurements were retaken at all lower energy points. The energy was then increased above the previous highest value and the process repeated.

As shown in Figure 4-11, the transmitted energy was nearly linear with input pulse energy over the range from 100 pJ to 375 nJ, with a transmission efficiency (including coupling losses) of approximately 44% for the 650 mm long fiber. The 710 mm long fiber had a smaller transmission (approximately 15%), but exhibited a similar trend. The first sign of damage in the 650 mm fiber occurred with 550 nJ input (190 nJ output) pulses. Damage was also first observed in the 710 mm long fiber for similar output pulse energy of 195 nJ. Since this output pulse energy corresponds closely with the calculated energy required to cause self-focusing, it is suggested that the damage is a direct result of self-focusing induced pulse compression of off-axis energy in space and time [56]. Input pulse energies that were higher than those required to initially damage the fiber resulted in subsequent damage and continued drop in fiber transmission. The transmission drops for the first two points taken after the transmission peak for the 650 mm long fiber (600 nJ and 650 nJ) were 89% and 83% of the peak respectively. Beyond

an input energy of 650 nJ, the transmission experienced only a slight drop with 81% of the peak delivered at 1000 nJ input energy.

Observation of the fiber input using a stereoscope as the input pulse energy was increased revealed the onset of a region of bright light slightly behind the input face for coupled pulse power above approximately 0.5 MW. This occurred in the 710 mm long fiber for an input (output) pulse energy of 400 nJ (60 nJ). The intensity of the light increased up to an input energy of 1600 nJ (output 195 nJ), as shown in Figure 4-12. Beyond 1600 nJ, the output energy dropped due to fiber damage. An explanation of the observed light can be found by considering the dynamics of the pulse as the power approaches the critical power for catastrophic self-focusing, P_{crit}. It has been suggested that a pulse propagating in a LMA fiber will undergo adiabatic focusing as the power is increased toward P_{crit} [57]. The intensity is therefore increased significantly in the fiber prior to the region where catastrophic self-focusing and damage occur. This increase in intensity will excite a cascade of nonlinear effects, causing significant spectral broadening and the experimentally observed 'bright light' region at the PCF input.

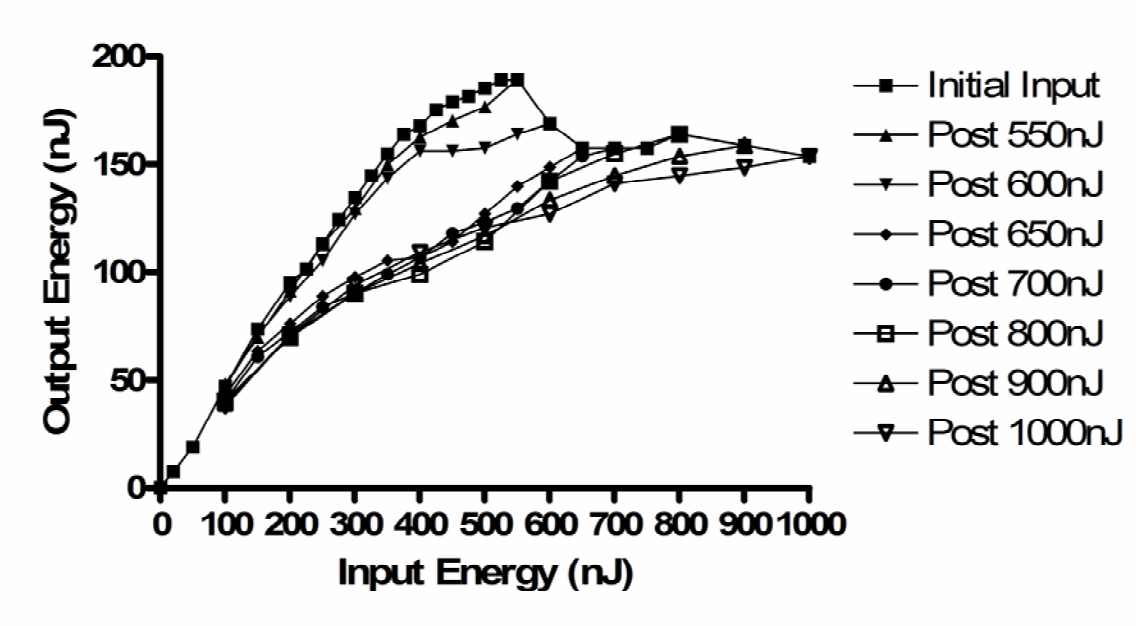

Figure 4-11. Energy transmission through 650 mm long PCF

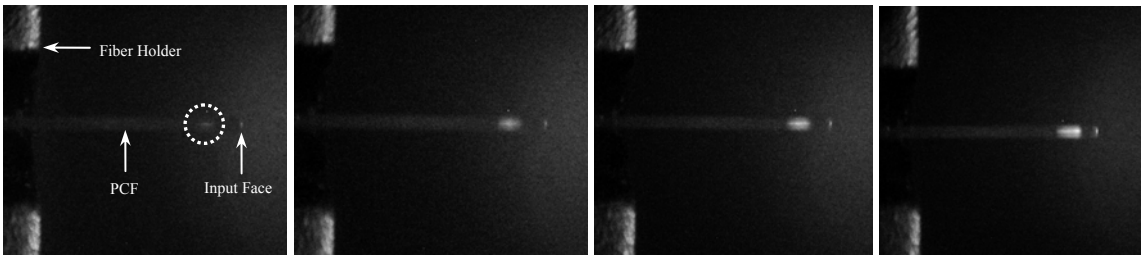

Figure 4-12. Images of PCF input for increasing input pulse energy in the 710 mm long fiber. Pulses are incident from the right. The input (output) pulse energies are 400 (60), 600 (100), 800 (117) and 1600 (195) nJ from left to right respectively.

4.1.3 Conclusions

For 30 nJ input pulses in the 710 mm long PCF, the measured output pulse energy was 2.6 nJ and the output spectrum showed no signs of self-phase modulation induced broadening. Spectral broadening began between an input energy range of 30 to 75 nJ (2.6 to 7.1 nJ output) and was symmetric about the central wavelength of the input pulses.

At an input pulse energy of 400 nJ, a bright light region became visible just after the fiber input face. This region continued to become more intense as the input energy was increased up to 1600 nJ, at which the output power was approximately the critical power for self-focusing. Above the self-focusing threshold, the fiber was further damaged by subsequent increases in input pulse energy. The experiment was repeated for a 650 mm length of the same PCF with similar results. Temporal dynamics were examined for the 650 mm fiber and it was found that side-lobes were present in the interferometric autocorrelation at input powers below the critical power for self-focusing. The side-lobes were attributed to the highly structured spectrum that results from fiber nonlinearities. As the output power was increased above the critical power for self-focusing, the temporal side-lobes disappeared, due to a reduction in peak intensity.

A delivered pulse energy of 2.6 nJ with negligible spectral broadening is comparable in delivered energy to that of previously reported values for a large mode-area PCF [54]. In comparison the previously reported fiber, the PCF in this study was slightly over half as long (710 mm compared to 1300 mm) and had a much smaller air-filling fraction (0.1 compared to nearly unity). The PCF in this study therefore had a much smaller numerical aperture and higher bend losses, but output a single transverse mode. In contrast, the PCF in [54] supported many higher-order modes, a few of which were observed at the output.

4.2 Hollow-Core Photonic Crystal Fiber (HC-PCF)

Hollow-core photonic crystal fiber (HC-PCF) was introduced in 1998 by Knight *et al* [58]. HC-PCF is typically fabricated by stacking silica capillary rods in a fiber perform

in precise arrangements to form a crystal lattice. Several rods are then removed in the center of the bundle to form a core region and a modified drawing method is used to pull a fiber. For certain capillary arrangements (e.g. hexagonal close-packed or triangular), a photonic crystal will exhibit a full two-dimensional (2-D) photonic bandgap. Modes with propagation constants (β) outside the bandgap will propagate in the cladding region. Modes with β values within a 2-D photonic bandgap cannot fill the cladding and are therefore confined to the core. Since the confining mechanism is not total internal reflection (TIR), the core does not have to have a higher index than the cladding, allowing propagation in an air core.

Photonic bandgap guidance can occur through two different processes: frustrated tunneling and Bragg guidance. In frustrated tunneling, $kn_2 < \beta < kn_1$ where k is the vacuum wave constant and n_1 and n_2 are the refractive indices of the high and low index regions respectively. This is the same condition as in a conventional TIR fiber. The high index regions act as TIR waveguides and the light is evanescent in the low index regions. Pass bands and band gaps exist between adjacent high index layers. If a high index layer has a smaller width than its neighboring high index layers and supports a β that is within the bandgap, then resonant tunneling between adjacent high index layers is frustrated. Bragg photonic bandgaps, on the other hand, occur for $\beta < kn_2$ allowing light to propagate in all layers and bandgaps occur as a result of multiple scattering and interference [59].

For high power delivery, the Bragg form is preferred over the frustrated tunneling form, since it allows concentration of optical power in air. Earlier silica-air HC-PCF with a honeycomb lattice of air holes guided light through frustrated tunneling and it was

found that light was confined to the fused silica surrounding the air core, but not actually in the core [58]. To ensure a Bragg photonic bandgap, air-filling fractions > 30% are typically required as well as the omission of more than one capillary to form the core.

The HC-PCF investigated in this section was generously donated by the Optoelectronics Group at the University of Bath in Bath, United Kingdom. The fiber is fused silica and has an outer diameter of 185 μm. The outer diameter of the cladding region is approximately 62 μm and the air core is approximately 27 μm in diameter. The cladding structure pitch is approximately 4 μm and the strut width is < 500 nm. An SEM image of the fiber endface is shown in Figure 4-13. The cladding for this fiber has a kagome-lattice (Star of David) structure which is generally associated with incomplete, or non-existent photonic bandgaps. Rather than true Bragg photonic bandgap guidance, it has been proposed that these fibers confine light to the air core by either suppressed coupling between core and cladding modes due to a low density of states in the cladding [60, 61] or through higher-order photonic bandgaps [62].

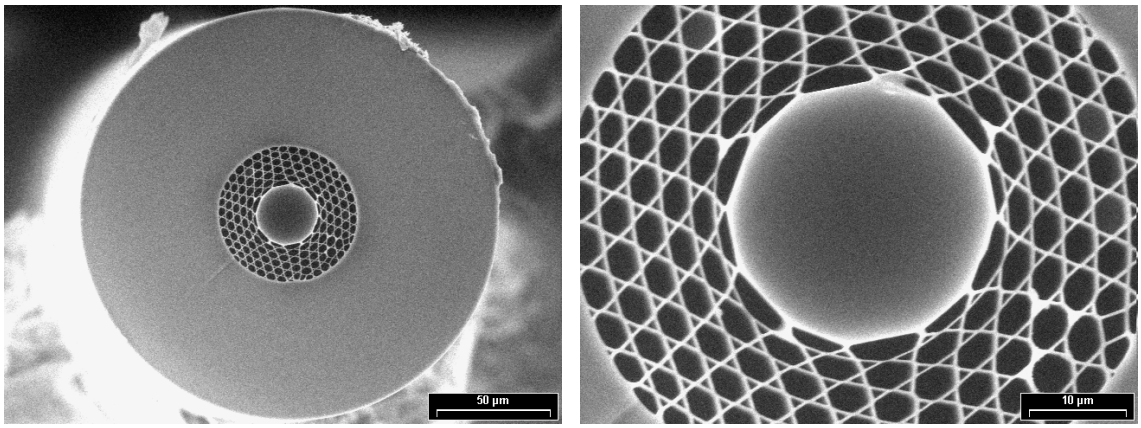

Figure 4-13. SEM image of HC-PCF cross-section (left) and close-up view of core and kagome structured cladding (right)

4.2.1 Characterization

4.2.1.1 Experimental Setup

Since the core diameter of the HC-PCF is similar in size to the PCF, the experimental setup for characterizing the HC-PCF was identical to the setup used for the PCF in section 4.1.2.1 with the main difference being slight adjustments to the beam expander to improve coupling. Also, above an input pulse energy of 2.6 μJ, the signal in the autocorrelator GaP detector was saturated and a neutral density filter was inserted before the autocorrelator to reduce the intensity. The fiber was also slightly repositioned for input energies above 2.6 μJ in order to improve the output beam profile and increase the transmission efficiency. Initial coupling to a 500 mm long section of HC-PCF revealed significant scatter at multiple points along the fiber, possibly due to imperfections or breaks in the kagome-lattice. Output beam profiles also confirmed that light was not guided in the core for the 500 mm long fiber. Therefore, a shorter 60 mm long section of HC-PCF was verified to be free of major scattering defects along its length and used for further testing. Similar to the PCF tested in the previous section, the HC-PCF was characterized by endfire-coupling femtosecond pulses and measuring the transmission efficiency, output beam profiles, output spectra and temporal dynamics as a function of the input pulse energy.

4.2.1.2 Output Beam Profiles

The near-field output beam profiles for 775 nm, 30 nJ, 135 fs, input pulses are shown in Figure 4-14. The fiber is illuminated with a white light source to aid in viewing the position of the guided mode within the core. The guided mode is centered within and

confined to the air core with minimal light propagating within the cladding. Figure 4-15 shows the near-field output beam profiles for input pulse energies ranging from 0.9 to 8 μJ without the additional white light excitation. For pulse energies at or below 2.6 μJ the output beam has multiple lobes that are attributed to a slight misalignment of the coupled pulses resulting in excitation of a few higher-order modes. Above 2.6 μJ, the fiber was repositioned and the output beam is single-mode with only minor asymmetry. A Gaussian fit of the output profile for 8 μJ input pulses resulted in an R^2 value of 0.989 (Figure 4-16), indicating the predominance of the fundamental mode.

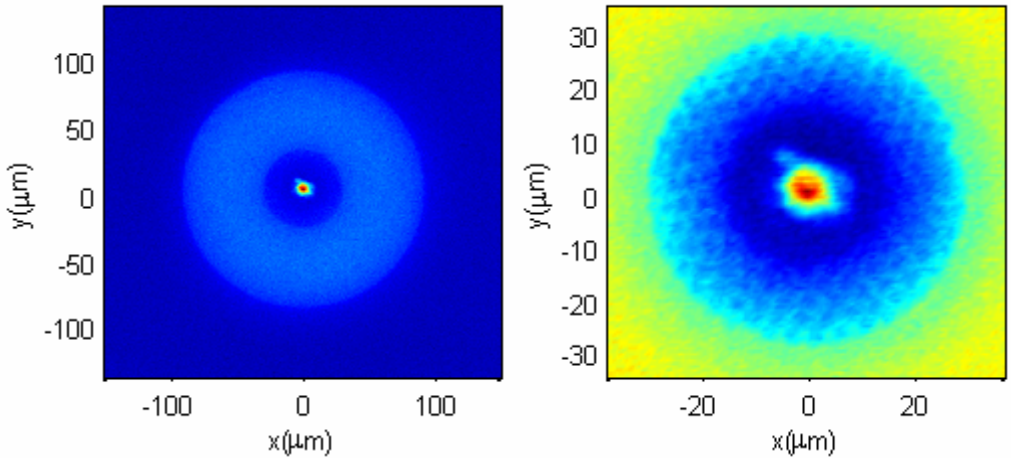

Figure 4-14. Image of 775 nm output from HC-PCF showing the position of the guided mode within the air core Left: entire fiber cross-section, Right: close-up of kagome-lattice cladding and core

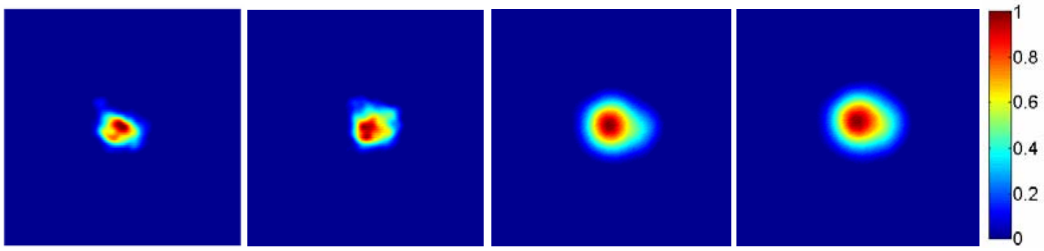

Figure 4-15. Output beam profiles for 0.9, 2.6, 4.2 and 8 μJ (from left to right respectively) input pulses in a 60 mm long HC-PCF

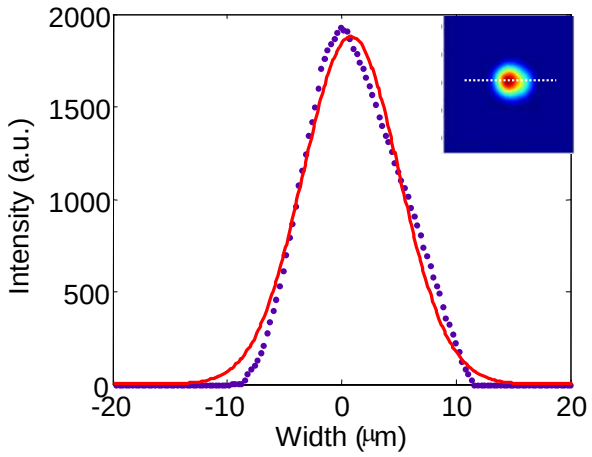

Figure 4-16. First-order Gaussian fit (solid line) of output profile for 8 μJ input pulses ($R^2 = 0.989$). (Inset) Dotted white line indicates plotted cross-section.

*4.2.1.3 **Temporal Dynamics***

The input pulses are the same as shown in the interferometric autocorrelation in Figure 4-6, with a pulse duration of approximately 110 fs. Interferometric autocorrelations of the output pulses were taken over an input energy range from 200 nJ to 6 μJ. Autocorrelations from 1 μJ to 6 μJ are plotted in Figure 4-17. At an input pulse energy of 1 μJ, the autocorrelation exhibits the characteristic 8:1 peak:wing ratio and has a FWHM pulse duration of approximately 100 fs assuming a Gaussian deconvolution factor ($\sqrt{2}$). For an input pulse energy of 2 μJ, the autocorrelation peak intensity is lower, but the FWHM pulse duration remains approximately the same. At 2.6 μJ input, the signal from the autocorrelator GaP photodiode was saturated at the pulse intensity peak as indicated by the flattening around zero delay in Figure 4-17. An ND filter was inserted before the autocorrelator to prevent the saturation and autocorrelations were taken for pulses above 4.2 μJ. Above 4.2 μJ, the autocorrelation FWHM is relatively unchanged giving a FWHM pulse duration of approximately 110 fs, which is the same as the input pulses.

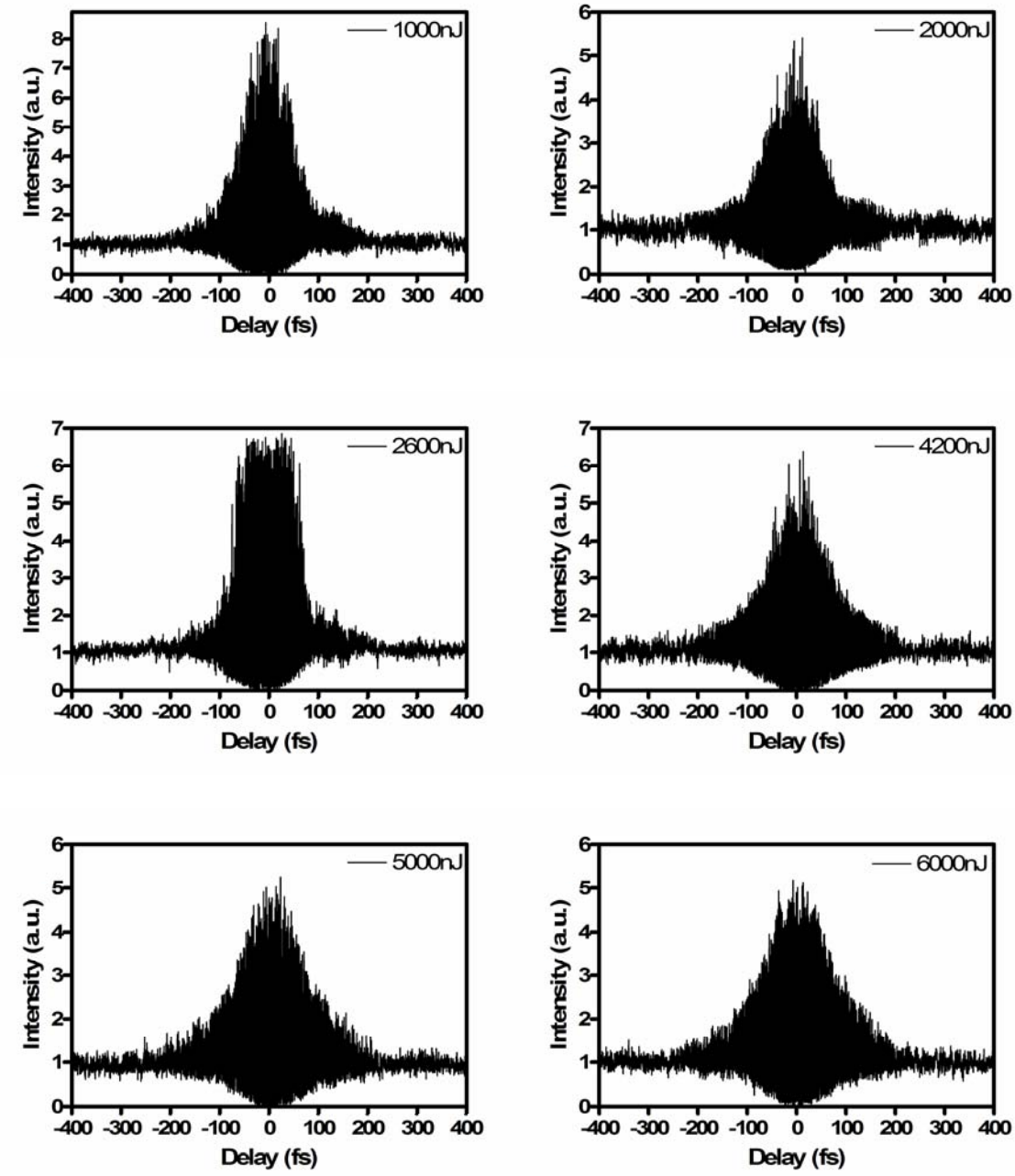

Figure 4-17. Interferometric autocorrelations of HC-PCF output for given input pulse energies

*4.2.1.4 **Output Spectra***

Output spectra were taken at input energies over the range from 1 nJ to 8 μJ. Unlike the PCF, the HC-PCF does not exhibit significant spectral broadening or modulation over the entire input energy range as shown in Figure 4-18 through Figure 4-20. The spectrum does, however, undergo subtle changes as the input pulse energy is increased. These changes are caused by interaction of the pulse with the kagome-lattice cladding which is a normally dispersive, Kerr medium. Although the portion of light in the silica strands of the cladding is typically on the order of a few percent for HC-PCF [63] and characteristically smaller for kagome lattice fibers [62], the contribution to the effective nonlinear refractive index is relatively large. For example, in [63] a HC-PCF was shown to have a nonlinear coefficient of 8.6×10^{-23} m^2/W whereas the nonlinear coefficient of air alone is 2.9×10^{-23} m^2/W, or about three times smaller.

For the HC-PCF under test, asymmetric spectral narrowing is observed at 1 μJ and a tail begins to form on the short wavelength side. The asymmetric formation of a tail on the short wavelength side is sometimes associated with self-steepening [18]; however, the temporal peak does not appear to be shifting in the interferometric autocorrelation data. Another possibility could be due to down-chirped input pulses undergoing SPM [64]. Above 4.2 μJ, the main spectral peak continues to narrow with increasing input pulse energy and a peak forms in the short-wavelength-side tail. The secondary peak is attenuated as input pulse energies are increased further. At 8 μJ, the main peak has narrowed to a FWHM of 9 nm, compared to the original FWHM of 11 nm and the secondary peak remains.

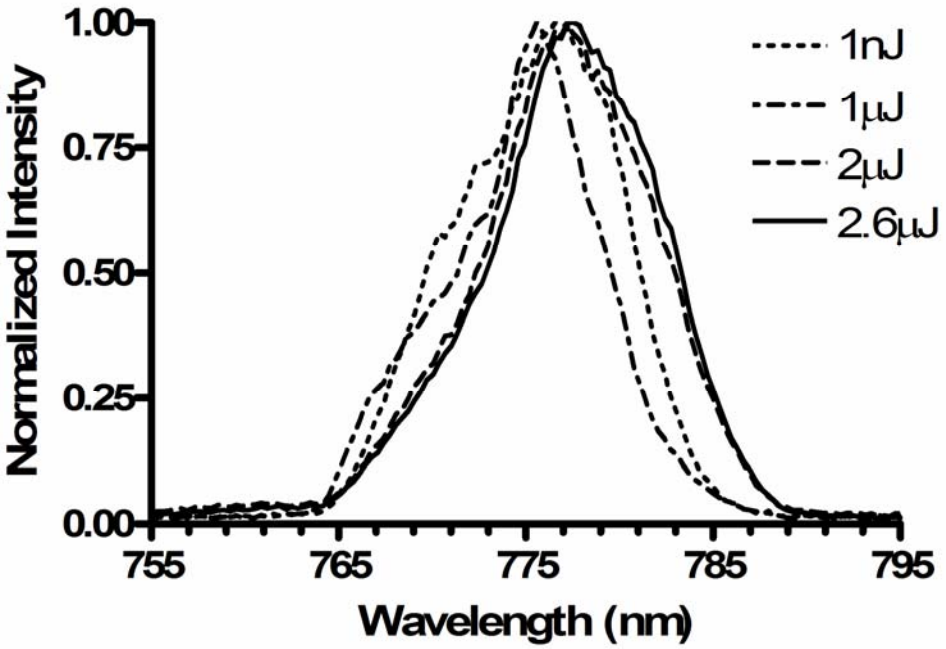

Figure 4-18. HC-PCF output spectra with input pulse energies < 2.6 μJ

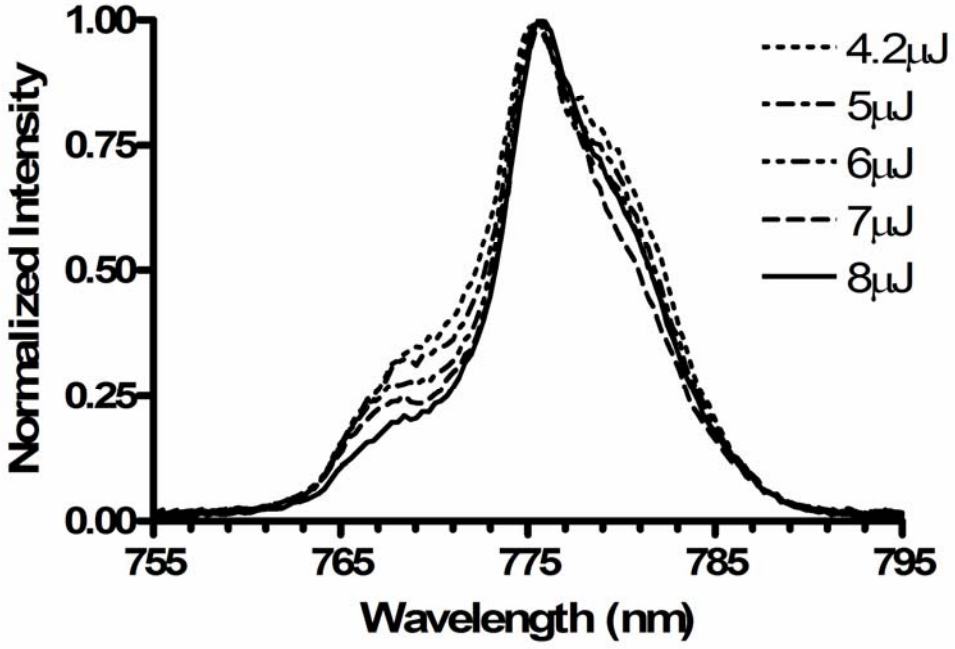

Figure 4-19. HC-PCF output spectra with input pulse energies > 4.2 μJ

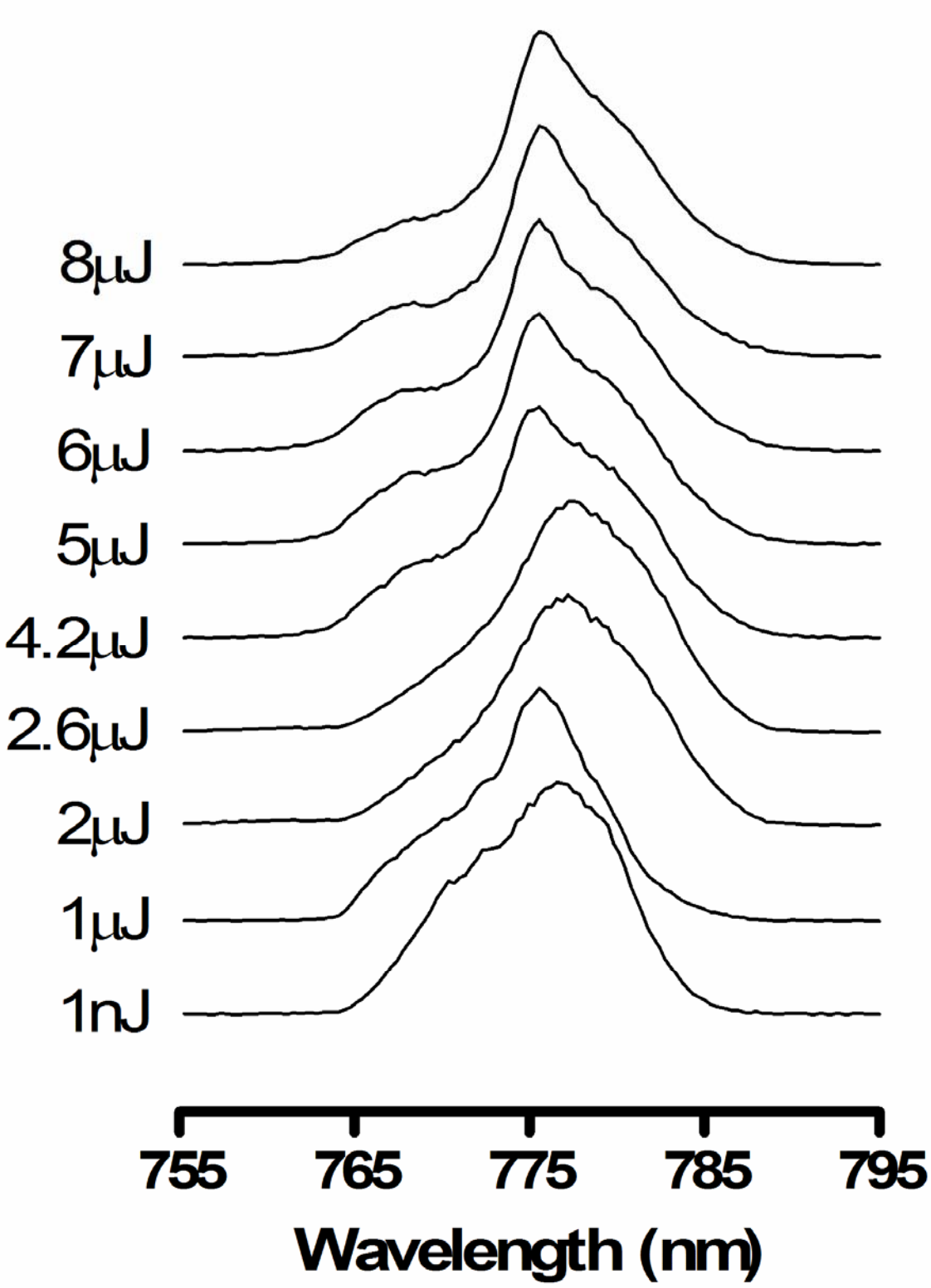

Figure 4-20. Output spectra from HC-PCF as a function of input pulse energy

4.2.1.5 ***Transmission***

The energy transmission through the HC-PCF as a function of the input energy is plotted in Figure 4-21. The transmission is linear over the entire range of energies tested, though the transmission efficiency of the more energetic input pulses is higher due to the predominance of the lower-loss fundamental mode. The transmission for the lower and higher energy ranges was approximately 24% and 34% respectively, including coupling losses. At an input energy of 8 μJ, the output energy was 2.6 μJ, corresponding to a delivered peak power of 23.6 MW and peak intensity on the order of 5 TW/cm^2.

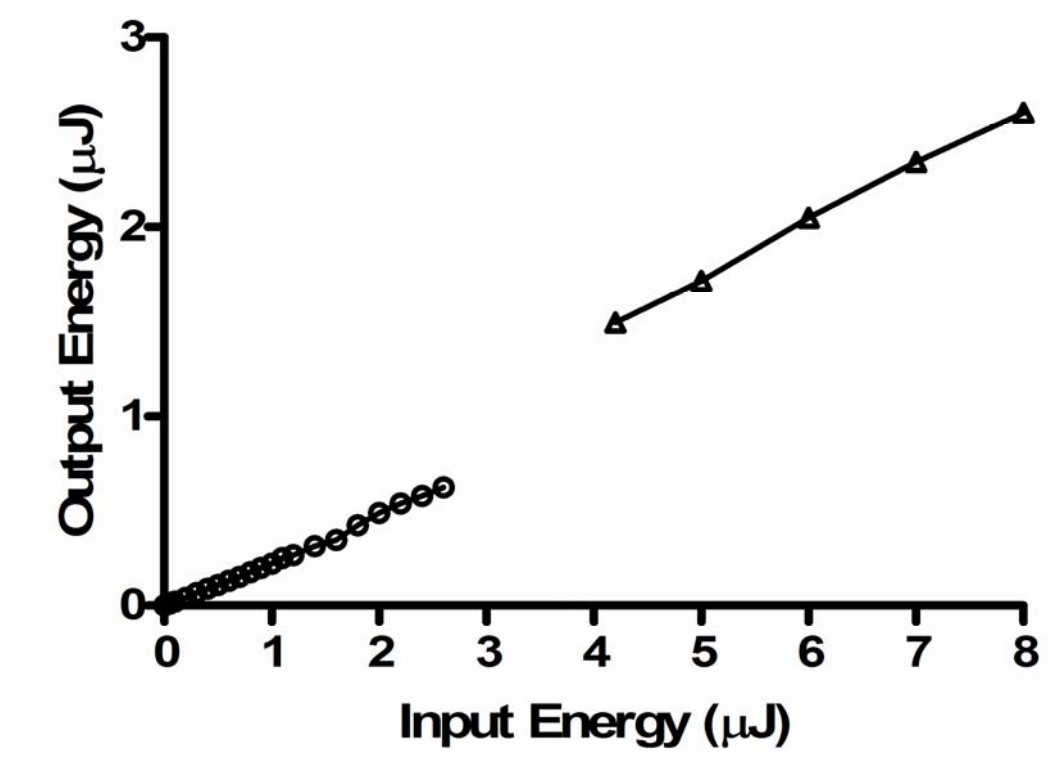

Figure 4-21 Energy transmission through 60 mm long HC-PCF

4.2.1.6 *Damage*

The fiber was inspected using a DIC microscope after coupling 3 μJ pulses. Discoloration of the cladding was observed at up to 1 mm away from the input end face as shown in Figure 4-22. However, this discoloration had no noticeable effect on the transmission properties of the fiber.

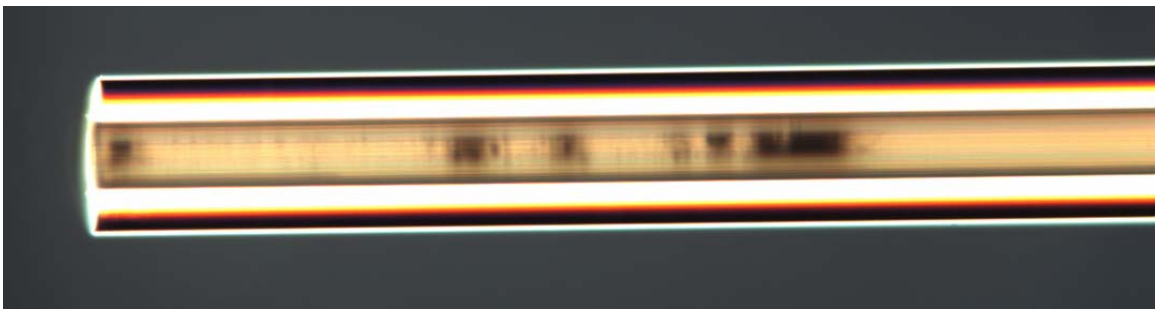

Figure 4-22. Discoloration in HC-PCF cladding after 3 μJ, 110 fs input pulses

4.2.2 Conclusions

A maximum energy of 2.6 μJ was delivered through the HC-PCF with no significant spectral broadening. The output spectrum is slightly broadened with a secondary peak forming on the short wavelength side as the energy is increased. Comparatively, a 3 m long, 12.7 μm core diameter HC-PCF exhibited a red-shift as pulse energy was increased above 300 nJ due to intrapulse Raman scattering in air [65]. However, the larger core, short length of HC-PCF in this study has a SRS threshold approximately 200 times higher.

The delivered energy of 2.6 μJ represents a peak power of 23.6 MW and an intensity in the core of over 4×10^{12} W/cm^2. Clearly, the nonlinear threshold for the HC-

PCF is much higher than for the solid-core PCF in Section 4.1. This is as expected, since the nonlinear coefficient of air is approximately 10^3 times lower than that of fused silica. Also, the trend of the energy transmission in Figure 4-21 suggests that the HC-PCF is capable of handling even higher power than was tested in this study, without significant deleterious effects on the transmitted pulse.

4.3 Hollow Silica Waveguide (HSW)

Hollow silica waveguides with a thin metallic inner coating have long been used to deliver CO_2 and Er:YAG laser energy in surgical and industrial applications [66]. More recently, similar waveguides have been developed to deliver ultraviolet, visible and near-infrared light [8, 9]. Applications directly related to high power ultrashort pulses include spectral broadening and pulse compression in gas-filled waveguides [67]. Matsuura *et al*. have also recently demonstrated the delivery of high power femtosecond regime pulses using cyclic olefin polymer (COP) coated hollow waveguides [10].

In this section, the transmission characteristics of high power femtosecond regime pulses are determined for silver coated hollow waveguides with four different bore diameters. The waveguides are commercially available and contain an inner thin-film dielectric layer to enhance the reflectivity of Er:YAG laser energy at the waveguide wall. Although the thickness of the dielectric layer is not optimized for low loss in the near-infrared, sufficient energy is transmitted to ablate tissue when focused by micro-lenses as discussed in Section 6.2.

The hollow waveguides were obtained from Polymicro Technologies, LLC. They are fabricated by first coating the inner wall of a silica tube with a thin film of Ag and

then a thin layer of AgI. The AgI acts to protect the Ag and also to enhance the reflectivity through thin-film interference. The thickness of the AgI layer for these particular waveguides has been optimized for delivery of Er:YAG radiation at a wavelength of 2.9 μm. The silica tube is protected by an acrylate buffer coating. The waveguide construct is shown in Figure 4-23 and the waveguide properties are listed in Table 4-2 [68].

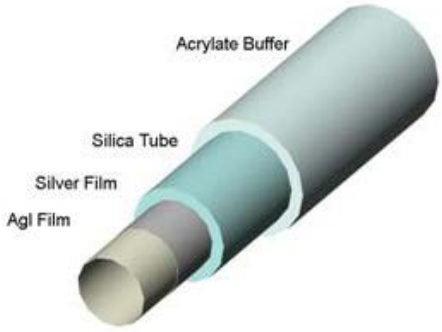

Figure 4-23. Hollow silica waveguide construct.

Table 4-2. Hollow Silica Waveguide Properties [68]

Bore I.D. (μm)	Glass O.D. (μm)	Buffer O.D. (μm)	Length (m)	Polymicro Part #
300 ± 20	400 ± 15	750 ± 25	1.0	HWEA300750
500 ± 25	650 ± 20	850 ± 30	0.5	HWEA500850
750 ± 30	950 ± 25	1200 ± 50	0.92	HWEA7501200
1000 ± 50	1300 ± 25	1600 ± 50	0.98	HWEA10001600

4.3.1 Characterization

4.3.1.1 Experimental Setup

A Spectra-Physics Spitfire Ti:Sapphire regenerative amplifier was used as a source for the femtosecond-regime pulses. The pulses had a central wavelength of 800 nm and a repetition rate of 1 kHz. The laser power was adjusted using a half-waveplate and

polarizer in the amplifier prior to pulse compression. An autocorrelator with a resolution of 5 fs was used to measure the temporal duration of the output pulses. In all cases, the input pulse duration was < 150 fs and the input pulse energy was ≤ 700 μJ.

It is well known that the HE_{11} mode experiences the lowest loss in a hollow waveguide and that the highest coupling efficiency to this mode is achieved for a laser beam waist to bore radius ratio of $\omega/\alpha = 0.64$ [69]. Therefore, an extremely long focal length (>1 m) is required for a single element lens, due to the short laser wavelength and relatively large waveguide bore diameters. In order to efficiently couple the laser to the HE_{11} mode in a much shorter distance, a telephoto lens system was used as illustrated in Figure 4-24. The positive and negative focal length lenses in the telephoto lens system are separated by a distance *s*. The waveguide input is located a distance *d* from the negative lens, and *s* is adjusted to obtain the proper waist. The focal lengths for the two lenses used were f_1 = 150 mm and f_2 = -48 mm. The distance *s* is limited by the extremely high intensities in the negative lens. As *s* is increased ($s < f_1$), the beam diameter in the negative lens becomes smaller and the intensity becomes sufficient to cause nonlinear effects and or damage in the lens. To avoid these effects, the beam diameter in the negative lens was maintained at > 2 mm.

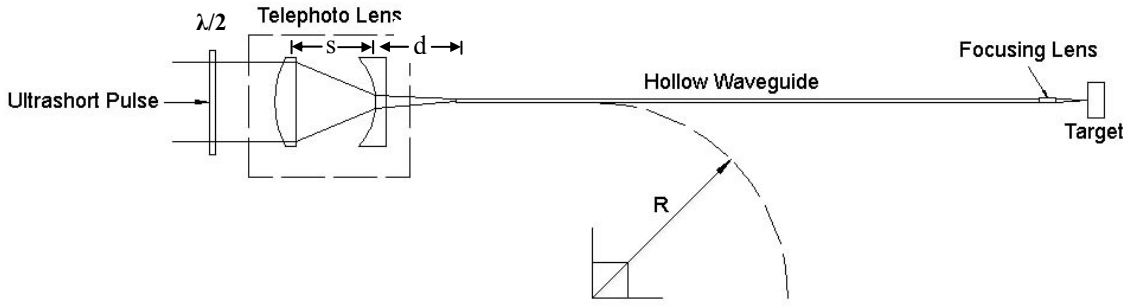

Figure 4-24: Experimental setup for testing hollow waveguides

The waveguides were placed in aluminum v-grooves attached to a 5-axis aligner during testing. For bend loss measurements, v-grooves with a bend radius of R = 500mm were used. The input polarization for the bend loss measurements was selected as either parallel or perpendicular to the bend plane using a half-waveplate prior to the coupling optics. Beam intensity profiles of the output from straight and bent waveguides were taken using a Spiricon Laser Beam Analyzer (LBA).

*4.3.1.2 **Beam Profiles of Output***

Intensity profiles of the output from straight and bent waveguides at distances < 50 mm from the distal end are shown in Figure 4-25 through Figure 4-28. In each figure, the profile on the left is for the straight waveguide and the profile on the right is for the waveguide bent 90º (45º for the 500 μm waveguide) with a 500 mm bend radius and perpendicular polarization. Most of the energy appears to be in the fundamental mode for the straight waveguides due to optimum launch conditions for excitation of the HE_{11} mode at the input. The profiles of the bent waveguides consist of numerous peaks due to higher-order mode excitation under bending.

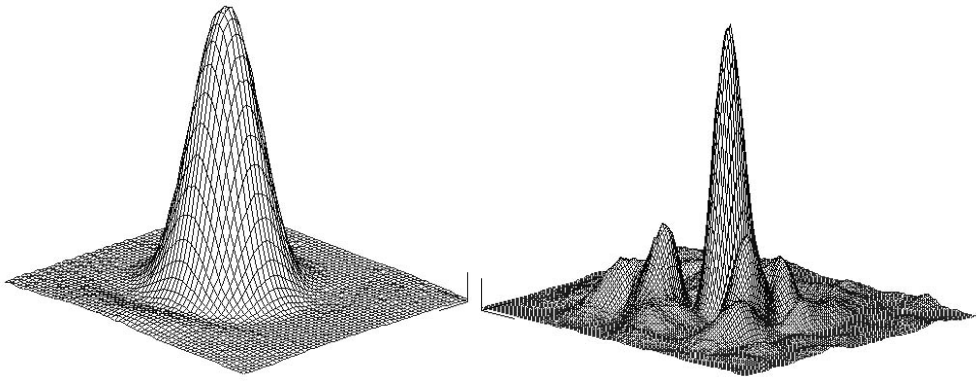

Figure 4-25: Output profiles for 300 μm bore diameter waveguide Left: straight waveguide, Right: bent waveguide

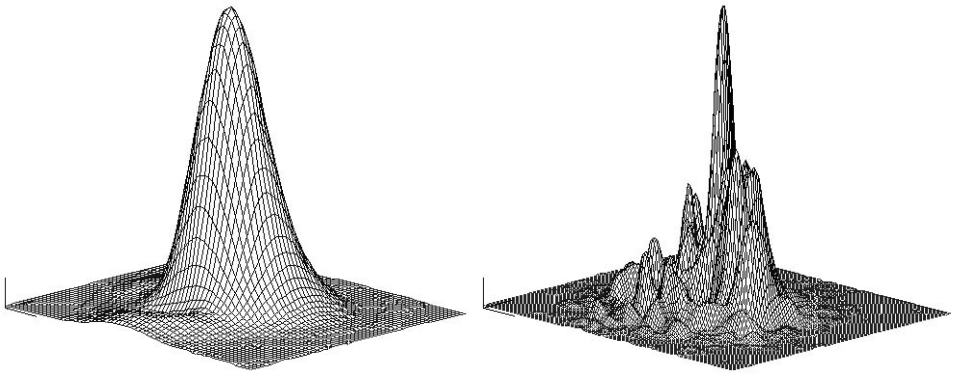

Figure 4-26: Output profiles for 500 μm bore diameter waveguide Left: straight waveguide, Right: bent waveguide

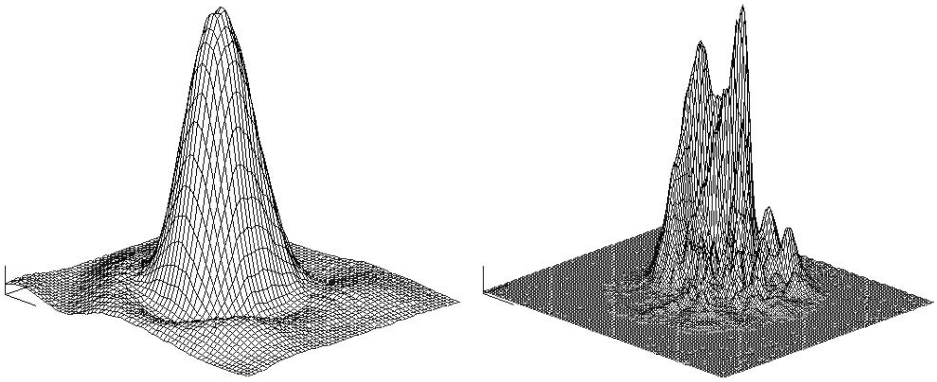

Figure 4-27: Output profiles for 750 μm bore diameter waveguide Left: straight waveguide, Right: bent waveguide

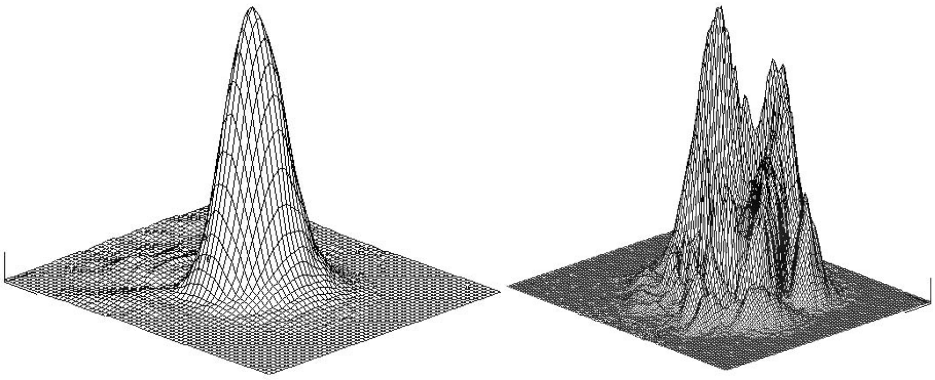

Figure 4-28: Output profiles for 1000 μm bore diameter waveguide Left: straight waveguide, Right: bent waveguide

4.3.1.3 Output Spectra

The output spectra for a straight 700 mm long, 750 μm bore diameter waveguide with τ_{FWHM} = 135 fs, 150 μJ input pulses is shown in Figure 4-29. The input and output pulses are nearly identical, indicating the absence of nonlinear effects.

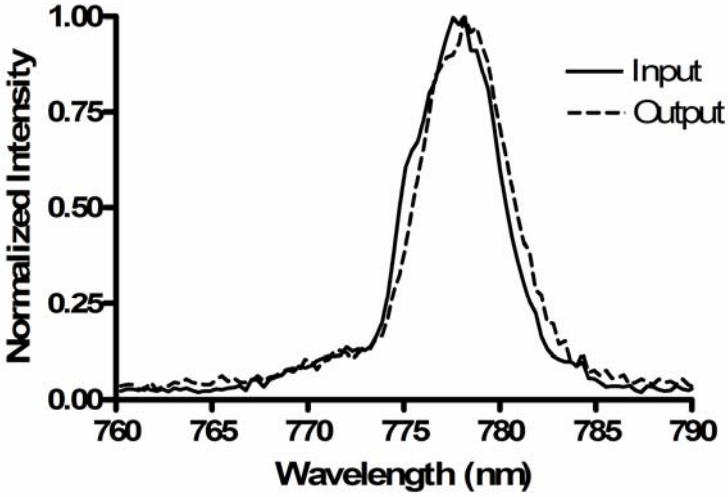

Figure 4-29. Output spectra from 700 mm long, 750 μm bore diameter waveguide with 150 μJ input pulses

4.3.1.4 Loss

The measured losses for straight waveguides and waveguides bent 90º (45º for the 500 μm waveguide) with a 500 mm bend radius are listed in Table 4-3. The losses are determined by measuring the power immediately before and after the waveguide, so coupling losses are included. The bend losses are listed for polarizations both perpendicular (⊥) and parallel (∥) to the bend plane.

The transmission for the straight waveguides is high due to minimal excitation of lossy higher order modes. A transmission efficiency as high as 91% was achieved for the 1 mm bore waveguide. The transmission of the 500 and 750 μm waveguides was slightly

less and the 300 μm waveguide exhibited the lowest transmission efficiency at 63%, which is likely due to the higher attenuation coefficients for the smaller bore and possibly a lower coupling efficiency. The bend losses are high due to the thickness of the dielectric layer not being optimized for 800 nm. Bending excites higher order modes which are lossy due to increased interaction with the waveguide wall. The loss is especially high when the input polarization is parallel to the bend plane due to the dominance of lossy TM modes [10].

Table 4-3. Measured Waveguide Losses

Bore Diameter (μm)	***Length***	***Straight Loss (dB/m)***	***Bend Loss (dB/m) R=500mm, ⊥***	***Bend Loss (dB/m) R=500mm, ∥***
300	1.00 m	2.0	10.7	36.1
500	0.50 m	0.6	12.6*	26.8*
750	0.92 m	0.54	10.2	38.2
1000	0.98 m	0.41	5.6	25.5

*45º bend angle, all others are 90º

4.3.2 **Comparison with Temporal Broadening Model**

The autocorrelation measurements of the temporal pulse broadening for straight and bent waveguides are listed in

Table 4-4. Pulse broadening in hollow waveguides is mainly a result of group delay of the modes in the waveguide or intermodal dispersion. In general, the broadening increases with waveguide bore diameter since the attenuation of higher order modes is less in the larger bore waveguides. The higher order modes in these waveguides are not `filtered` as efficiently as they are in the smaller bore waveguides and propagate through

to the output where they are delayed with respect to the lower order modes. The measured broadening in the straight 300 and 500 μm waveguides is on the order of the resolution of the autocorrelator. The number of modes present at the output of the waveguides can be estimated from the pulse broadening which corresponds to the difference in the group delay between the highest and lowest order modes. Following the analysis in reference [10], the transverse phase constant *u* and number of transmitted LP modes were determined for each of the waveguides. The results are listed in Table 4-4. The number of transmitted modes generally increases with both waveguide bore diameter and bend. A minimum of two modes are estimated for the straight 300 μm waveguide, while the number of transmitted modes for the bent 1000 μm waveguide is more than 50.

Table 4-4. Pulse Broadening in Hollow Waveguides

Bore Diameter	***Straight (fs)***	***Bent 500mm, ⊥ (fs)***	***u, straight (LP mode order)***	***u, bent (LP mode order)***
300	4	-	3 (2)	-
500	6	13*	5 (4)	6 (6)
750	15	22	9 (13)	11 (19)
1000	24	69	16 (35)	26 (>50)

*45º bend angle

The measured values for temporal broadening were compared to a refined ray tracing program that took into account roughness of the internal reflecting and refracting inner layers [16]. A comparison between the experimental measurements and calculations conducted at identical parameters are listed in Table 4-5. The 500 μm bore diameter dispersion values are for a 0.5 m length of waveguide, compared to nearly 1 m lengths for the other bore diameters. Overall, good agreement is found between experiment and theory, with as little as 8% difference between experiment and simulation [16].

Table 4-5. Comparison between the experimental and calculated values for pulse dispersion in hollow silica waveguides [15]

Bore Dia. (μm)	*Waveguide*	*Theoretical Smooth*	*Theoretical Rough*	*Experimental*
500	Straight	9	11	6
	Bent[a]	11	18	13
750	Straight	17	22	15
	Bent[a]	19	30	22
1000	Straight	26	30	24
	Bent[a]	60	75	69

[a]R = 500 mm

4.3.2.1 ***Damage***

No damage was observed in the straight waveguides for input energies up to 700 μJ. In fact, a long term power delivery study was conducted in which 430 μJ was delivered through a straight 750 μm waveguide over a period of 8 hours without a loss in power or waveguide degradation. However, damage was observed in the 750 μm waveguide when it was bent with 300 μJ input with perpendicular polarization after only a few minutes of irradiation. Damage spots, in which the silver coating was discolored, were present along the outer edge of the waveguide at several areas along the bend (Figure 4-30). This is likely due to the shift in electric field distribution to the outer edge which occurs in bent waveguides [70].

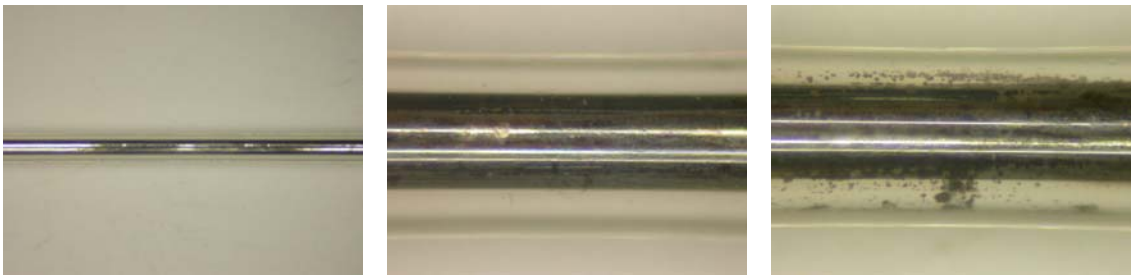

Figure 4-30. Damage in 750 μm hollow waveguide with 300 μJ input pulses as a result of bending

4.3.3 **Conclusions**

The transmission characteristics of commercially available hollow waveguides with four different bore diameters were determined for ultrashort pulses from a Ti:Sapphire laser. A telephoto lens system was used to efficiently couple the laser to the HE_{11} mode at the waveguide input. The waveguides exhibited low loss when straight and significantly higher losses when bent, due to excitation of lossy higher order modes. Beam intensity profiles confirmed that most of the energy remained in the HE_{11} mode at the output of the straight waveguides and multiple intensity peaks were present for the bent waveguides. Autocorrelation measurements show increasing pulse broadening with waveguide bore diameter and bend. The number of transmitted modes was estimated from the pulse broadening and it was shown that the mode order increases with both waveguide bore diameter and bending. No damage was observed for up to 700 μJ in the straight waveguides, but 300 μJ was sufficient to damage the 750 μm waveguide when bent. This damage was in the form of discoloration of the silver coating at several spots along the outer waveguide wall along the bend.

5 Femtosecond Direct-Written Waveguide Arrays

In this chapter, the femtosecond direct-write technique is used to fabricate optical waveguide arrays in soda-lime glass and fused silica substrates. A brief background on the technique is given as well as examples of prior art. The main variables at play during waveguide writing are discussed and the experimental setup is described in detail. The conditions required to obtain single-mode waveguides in each substrate type are determined. The concept of supermode 'tailoring', as described and modeled in section 3.3, is also tested by fabricating common-core waveguide arrays with varying center-core properties in both soda-lime glass and fused silica. The central core refractive index and diameter are shown to be key variables in tailoring the guided modes in common-core arrays as predicted in Chapter 3 by the Scattering Matrix Method (SMM) model.

5.1 Laser Direct-Writing

Laser direct writing in transparent materials was first described by Sopori and Chang in 1978, when they used a CO_2 laser to write a densified track in a thin film of Na_2O/SiO_2 [71]. Femtosecond laser direct-written waveguides were first reported by Davis *et al.* in

1996 [12]. In short (see Chapter 2 for a more in-depth discussion on the physics of femtosecond pulse-material interaction), when a femtosecond pulse of sufficient energy is focused inside the bulk of a transparent material, multiphoton absorption, nonlinear ionization, optical breakdown and subsequent plasma formation occurs near the beam waist. Rapid quenching and re-solidification follow, resulting in morphological, chemical and physical changes to the material. By translating the substrate with respect to the beam, a modified line is 'written' in the material. The process is very dependent on the writing conditions, e.g. pulse width, translation speed, pulse energy, repetition rate, focusing conditions and material properties. When the conditions are within a narrow optimal range for writing waveguides, the refractive index within the focal volume is increased with respect to the surrounding material due to densification. Typical values of the refractive index increase, Δn, are on the order of 10^{-4} to 10^{-3}. Other phenomenon, such as color-centers or void formation may also result depending on the type of material and writing conditions.

Direct writing of waveguides in bulk transparent substrates using femtosecond laser pulses has opened the possibility to fabricate complex three-dimensional devices that would have been impractical with technologies such as planar fabrication or ion-exchange [12]. A number of waveguide properties such as diameter, cross-section, depth and refractive index can be finely tuned by controlling the characteristics of the writing beam. Since the process relies on nonlinear or multiphoton absorption, it is amenable to a variety of transparent substrates and material modifications can be confined to a small focal volume. Several groups have demonstrated the ability to direct-write three-dimensional devices such as splitters [72], directional couplers [73], interleavers [74] and

interferometers [75]. Linear, cubic and hexagonal direct-write waveguide arrays have also very recently been fabricated by Szameit *et al.*; their group has also characterized the coupling characteristics of these devices and demonstrated spatial soliton formation at high peak powers [76].

5.1.1 Waveguide Writing Variables

Although many of the following variables are fixed in this work, it is important to understand their effect on the waveguide writing process and to define the phase space over which single-mode waveguides can be fabricated.

5.1.1.1 Materials

The list of materials investigated by researchers continues to grow. These include organic glasses, inorganic glasses, polymers, thin films and crystalline materials. The type of index change induced by femtosecond laser pulse processing is dependent on the type of material. For example, some materials exhibit lower refractive index changes [77] or color centers [32]. The magnitude of the induced index difference for a given writing pulse is also material dependent. Of special interest in this work are silicate glasses, in particular soda-lime glass (Corning 0215) due to its low cost and widespread availability and fused silica (Corning HPFS) due to its lack of impurities, well known properties and prevalent use in the fields of fiber optics and optical waveguides.

*5.1.1.2 **Parallel versus Perpendicular Writing***

Two different waveguide writing configurations that are often used are parallel (a.k.a. longitudinal) and perpendicular (a.k.a. transverse or side-writing). These are in reference to the way in which the beam is focused into the sample, i.e. either parallel to the optical axis or perpendicular to it respectively as shown in Figure 5-1.

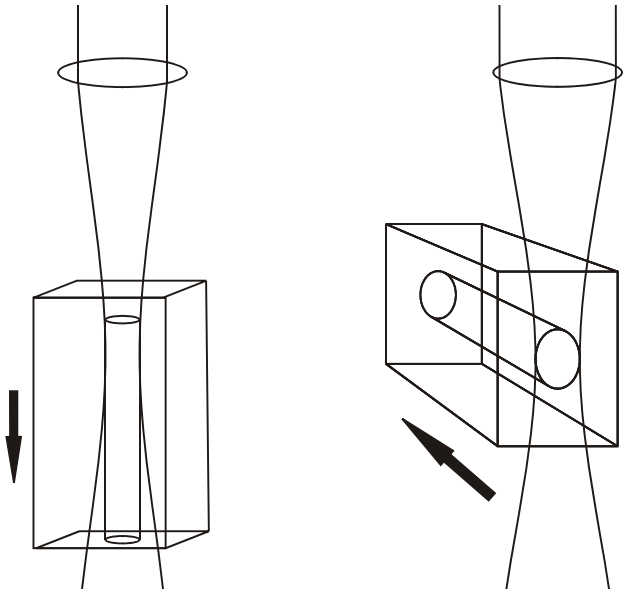

Figure 5-1. Parallel (left) and perpendicular (right) waveguide writing schemes. The arrow indicates the movement direction of the substrate.

Each method has obvious advantages and disadvantages. Parallel writing can produce waveguides with a circular cross-section, however, waveguide length is limited by the working distance of the focusing lens. Also, since the writing depth is constantly changing and comparatively large, parallel writing is more susceptible to optical absorption, spherical aberrations and nonlinear effects. Perpendicular writing has the advantage that the writing depth can be maintained, typically at a shallow depth, during

writing so as to avoid absorption, aberrations and nonlinearities. It can also be used to write arbitrarily long waveguides, limited in length only by the substrate size or translation stage limits. Its main drawback is that, unless the beam is focused to a very small spot size (using a high numerical aperture, short focal length lens), the waveguide cross-section is non-circular and elongated along the optical axis. Perpendicular writing is often the preferred technique and therefore a number of groups have developed methods to correct the waveguide symmetry. The method of astigmatic focusing, described by Cerullo *et al.* [78] is one such technique and is implemented in the experimental setup in Section 5.3.1.1.

5.1.1.3 ***Focusing Conditions***

As discussed in Section 2.1, the behavior of femtosecond pulses in transparent materials is very dependent on the focusing conditions. Effects such as supercontinuum generation and multiphoton-induced bulk damage typically have threshold values that can be described in terms of the numerical aperture of the focusing lens [17]. Generally, for small numerical apertures (i.e. loose focusing), supercontinuum generation can occur as a result of significant spectral broadening due to nonlinear effects. This affects the writing process in that material modifications can now occur as a result of linear or two-photon absorption of the blue edge of the spectrum. Also, self-focusing and subsequent re-focusing due to plasma formation can occur, resulting in multiple regions of material modification. Conversely, large numerical apertures typically result in damage at thresholds below the power of self-focusing and material modifications occur only within the focal volume dictated by the focusing optics. All waveguides in this study were

written using a 20× microscope objective with a numerical aperture of 0.4, which is considered to be in the high numerical aperture regime. However, interesting effects, including multiple zones of modification, which are typically associated with low NA focusing are noted in Section 5.3.1.1 and are attributed to focusing an astigmatic beam.

5.1.1.4 ***Pulse Energy***

The energy at which material modification occurs is highly dependent on the focusing conditions. At low NA, the energy required to elicit a permanent change in the material is higher, since self-focusing and/or blue edge supercontinuum light are responsible. At high NA, the energy required for material modification is typically less than the threshold of self-focusing, as multiphoton absorption and avalanche ionization readily occur in the small focal volume [22].

Different regimes of material modification are also dependent on applied energy. For example, silicate glasses exhibit a threshold for refractive index modification as well as void formation. Refractive index modifications can be due to densification, localized melting and re-solidification or color center formation. While each of these mechanisms is dependent on the material and writing beam properties, they all rely on multiphoton absorption and therefore have a nonlinear dependence on energy applied. Void formation is associated with high energy pulses producing micro-explosions in the focal volume that result in rapid expansion of hot electrons and ions into the surrounding material [33].

The writing pulse energy is the main variable in this work. The properties of the written waveguides, namely the core diameter and the magnitude of the refractive index change, are controlled by adjusting only the pulse energy. All other conditions were

constant during the writing trials. Three writing pulse energies, each for the soda-lime glass waveguides and the fused silica waveguides, were chosen to give three single-mode waveguides that could be used in fabricating waveguide arrays with tailored supermodes.

5.1.1.5 ***Repetition Rate and Translation Speed***

The waveguide writing process is also dependent on the repetition rate of the writing pulses. Two regimes are often considered, with 1 MHz typically defined as the cutoff between the low and high repetition rate regimes [22]. The 1 MHz cutoff is determined by the time it takes thermal energy to diffuse out of the focal volume, which is on the order of 1 μs. If the pulse repetition rate is faster than the thermal diffusion time, successive pulses heat the material in and around the focal volume in a cumulative fashion, until the material is modified to an extent to which the beam focus is interrupted [22]. At this point no further material modification occurs. If the repetition rate is slower than 1 MHz, then the electrons have sufficient time to transfer heat to the lattice between pulses and structural changes are tightly confined to the focal volume.

The repetition rate is also closely related to the translation speed required to write continuous structures. Modified volumes are often on the order of 1 μm wide, so in order to achieve sufficient overlap of successive pulses, and therefore obtain continuous structures, low repetition rate lasers require slow sample translation speeds, typically < 100 μm/s. On the other hand, high repetition rate lasers allow much faster translation speeds, on the order of several mm/s. The direct-write waveguides in this dissertation were written with a 1 kHz repetition rate and are therefore in the low repetition rate

regime. The translation speed used to write waveguides with smooth boundaries was 20 μm/s.

5.1.1.6 ***Wavelength***

Laser direct writing of structures in glass is typically accomplished using either UV lasers or femtosecond lasers. UV lasers induce material modifications by absorption of single-photons, with energies exceeding the material bandgap energy. Near-infrared (NIR) femtosecond pulses, on the other hand, rely on multi-photon absorption and therefore have an advantage over UV in many respects. For example, deep bulk modifications are not possible with UV lasers, since the penetration depth is prohibitively short (typically 100 μm or less). NIR femtosecond pulses, however, can penetrate much deeper into most materials since their photon energy is less than the material bandgap energy and therefore are well suited to bulk processing and the fabrication of three dimensional waveguides [79]. The femtosecond laser used in this study has a central wavelength of 775 nm that was fixed for all writing experiments.

5.1.1.7 ***Pulse Duration***

In order for permanent structural changes to be induced in a transparent material, the laser intensity must exceed the optical breakdown threshold. Since intensity is inversely proportional to the pulse duration, it follows that long pulses will require more energy or tighter focusing to achieve optical breakdown and plasma formation. The plasma that is formed near the temporal peak of the pulse absorbs energy from the second half of the pulse [22]. Shorter pulses require less energy to achieve optical breakdown and therefore

deposit less energy into the plasma, thereby producing smaller, more confined structural changes. In order for structural changes to be confined to a volume on the order of the focal volume, the pulse duration should typically be less than a few hundred femtoseconds, although waveguiding structures have also been fabricated with pulse durations up to 1 picosecond [80]. The laser used in this study has a full-width at half-maximum (FWHM) pulse duration of 135 fs that was fixed for all waveguide writing experiments.

5.2 Waveguide Writing Setup

The experimental setup is illustrated in Figure 5-2. A Clark-MXR CPA-2010 Ti:Al_2O_3 regenerative amplifier was used for all waveguide writing experiments. It has a center wavelength of 775 nm, a repetition rate of 1 kHz, a full-width at half-maximum (FWHM) temporal pulse width of 135 fs and produces pulses with energies up to 1 mJ. The laser power is adjusted using a half-waveplate and polarizer combination with the half-waveplate mounted in a computer-controlled rotation stage. The typical output from the half-waveplate and polarizer combination is plotted in Figure 5-3. The light reflected from the polarizer is monitored using a photodiode. The photodiode signal is digitized and recorded by a computer; this feedback provides a means by which the power can be controlled using a simple algorithm to adjust the half-waveplate *in situ*.

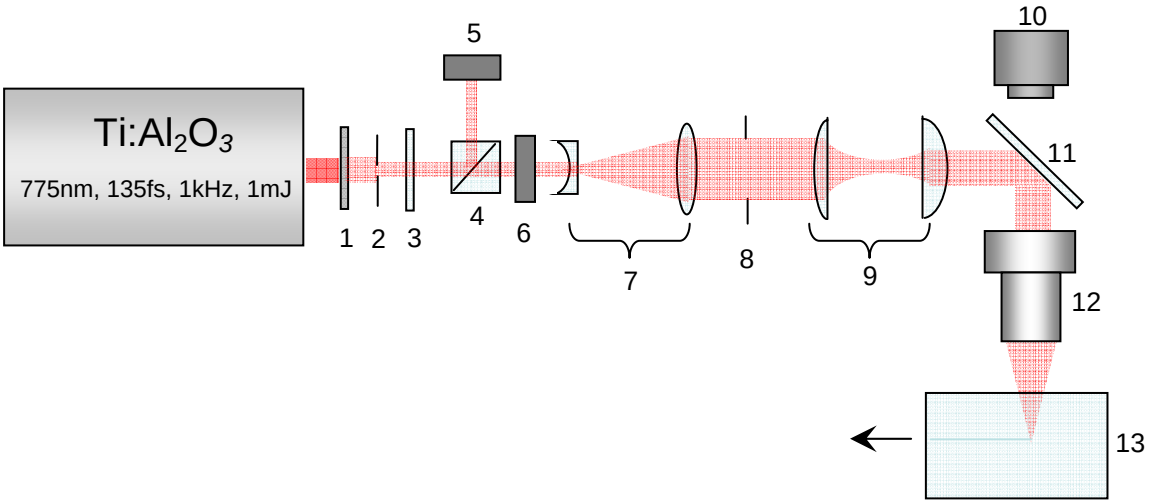

Figure 5-2. Experimental setup: 1. adjustable neutral-density filter, 2. pinhole, 3. half-wave plate mounted in motorized rotation stage, 4. polarizer, 5. digitized photodiode, 6. shutter, 7. beam expander, 8. aperture, 9. cylindrical telescope, 10. CCD camera, 11. dielectric turning mirror, 12. microscope objective, 13. substrate

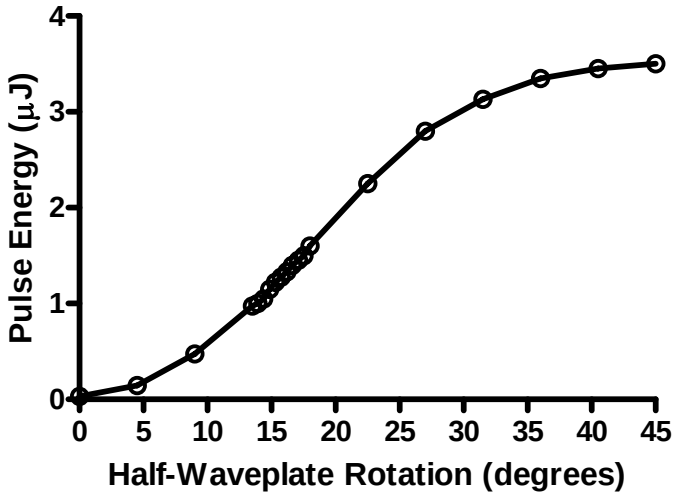

Figure 5-3: Pulse energy as a function of half-waveplate rotation. Measured before the microscope objective.

5.2.1 **Spatial Filtering**

The beam exiting the laser aperture is slightly elliptical due to the transmissive gratings used in the chirped-pulse amplifier pulse compressor. Spatial filtering is therefore required to attain a circular Gaussian beam. Due to the high intensities of focused amplified femtosecond pulses, traditional spatial filters that require tight focusing through a small pinhole cannot be used due to damage to the pinhole and air breakdown. Vacuum spatial filters are often used with such high power systems; however, a simpler, alternative spatial filter was used for the waveguide writing experiments. Here the beam is first passed through a 600 μm pinhole. Diffraction causes the light transmitted through the pinhole to form an Airy pattern in the far field. The airy pattern is then expanded in a 4× beam expander and the center-most lobe of the Airy pattern is selected by transmitting the beam through an aperture that blocks the fringes. A typical beam profile after the aperture is shown in Figure 5-4. A significant amount of energy is lost using this method, however, only a small fraction (< 1/500) of the overall energy produced by the amplifier is actually required to write waveguides.

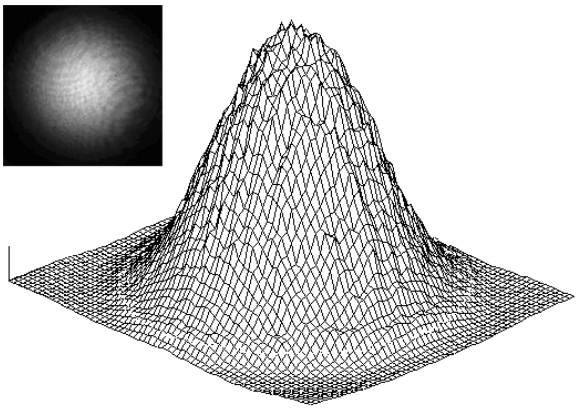

Figure 5-4: Beam profile after expander and aperture

5.2.2 **Astigmatic Beam Shaping**

After weighing the positive and negative aspects of parallel and perpendicular waveguide writing discussed in Section 5.1.1.2, perpendicular writing was chosen due to the ability to machine at a constant depth over a large area. As discussed in Section 5.1.1.2, the main drawback to perpendicular writing is the waveguide cross-sectional asymmetry. This is caused by a narrow waist and relatively long Rayleigh range that are formed by focusing a Gaussian beam through a spherical lens. Several groups have developed alternative methods that give some control over the waveguide cross-sectional symmetry. For example, Liu *et al.* used a multipass scheme to effectively widen the modified region, thereby creating more symmetric waveguides. Moh *et al.* inserted rectangular apertures before the focusing objective in an astigmatic focusing technique that focuses the *x* and *y* axes to different degrees and de-couples the Rayleigh lengths [81, 82]. The result is a cross-section that is dependent on the geometry of the rectangular aperture. This technique is a simplification of a method originally developed by Cerullo *et al.* in which they used a cylindrical telescope rather than a rectangular aperture to provide the astigmatic beam [78, 83]. The advantage of their method is that the astigmatic difference (and waveguide cross-section) can be continuously tuned by adjusting the distance between the two lenses in the cylindrical telescope. Following the derivation in [83], the intensity for a focused astigmatic Gaussian beam is given by:

$$I_0(x,y,z) = I_{00}\frac{\omega_{0x}}{\omega_x(z)}\frac{\omega_{0y}}{\omega_y(z)}\exp\left[-2\left(\frac{x^2}{\omega_x(z)^2}+\frac{y^2}{\omega_y(z)^2}\right)\right] \tag{3.16}$$

where,

$$\omega_x(z) = \omega_{0x}(z)\sqrt{1+\left(\frac{z}{z_{Rx}}\right)^2} \tag{3.17}$$

and

$$\omega_y(z) = \omega_{0y}(z)\sqrt{1+\left(\frac{z-z_0}{z_{Ry}}\right)^2} \tag{3.18}$$

In the preceding equations, I_{00} is the initial intensity, ω_{0x} and ω_{0y} are the beam waists in the x and y directions respectively, z_0 is the distance between the beam waists and

$$z_{Rx,y} = \pi\left(\omega_{0x,y}{}^2/\lambda\right) \tag{3.19}$$

are the independent Rayleigh ranges. The intensity in the vicinity of ω_{0x} for an astigmatic beam is shown in Figure 5-5. A cylindrical telescope that provides 3× de-magnification in the *y*-direction was used to shape the beam. A typical beam profile at the output of the cylindrical telescope is shown in Figure 5-6.

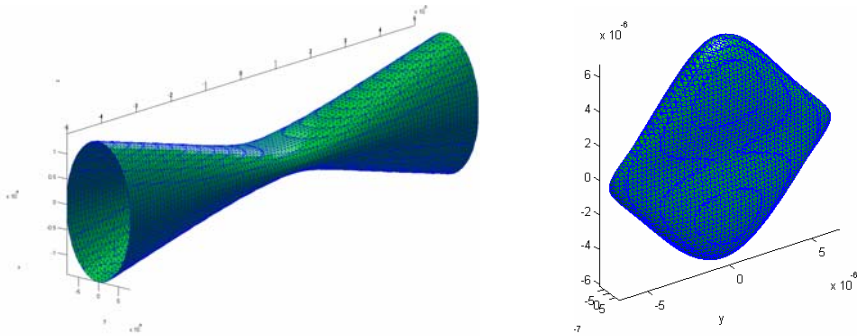

Figure 5-5: Left: Model of focused astigmatic beam in the vicinity of ω_{0x}. Right: Constant surface of intensity at ω_{0x} sufficient for material modification.

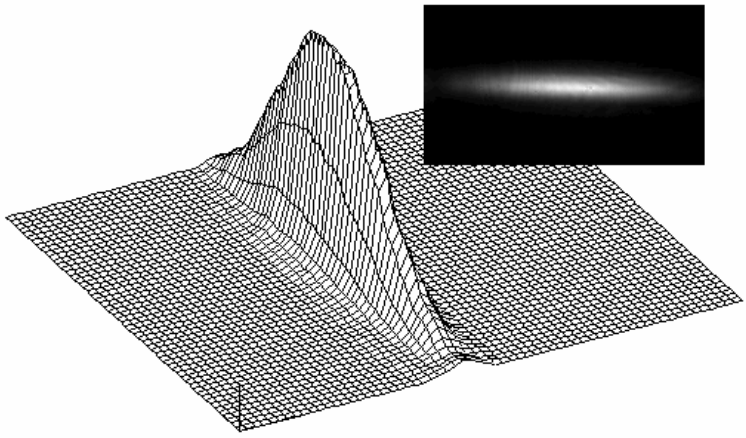

Figure 5-6: Beam after cylindrical telescope.

5.3 Soda-Lime Glass Waveguides

Sodium calcium silicate ($22Na_2O{\cdot}3CaO{\cdot}75SiO_2$) or soda-lime glass is the most common and widely available type of glass and is often used as a base component for more complex glasses. Commercially available soda-lime glass typically contains impurities such as Fe^{3+} that shift the absorption edge to a lower energy and contribute to photoionization. Several groups have investigated color-center formation (darkening) in both high [84] and low-purity [26] soda-lime glass substrates irradiated by femtosecond laser pulses and defect types and kinetics are fairly well understood. In this section, waveguides are directly written in commercially available soda-lime glass substrates (Corning 0215) using femtosecond laser pulses. Waveguides are characterized based on cross-section, refractive index change and mode quality. Three single-mode waveguides with different mode-field diameters are selected and used to investigate supermode tailoring and discrete diffraction in waveguide arrays.

5.3.1 Single Waveguide Characterization

In order to fabricate arrays for investigating the tailoring of waveguide supermodes, at least three single-mode waveguides are needed that vary in diameter and/or refractive index. The waveguide cross-sections must be circularly symmetric to ensure directional independence in evanescent coupling and the refractive index change and core diameter must be small enough to ensure single-mode operation. Experimental matrices were set up to determine firstly, the proper cylindrical telescope lens spacing and astigmatic difference for producing circularly symmetric waveguides and secondly, the proper writing pulse energy to ensure single-mode operation.

5.3.1.1 Waveguide Shaping Using Astigmatic Focusing

As discussed in Section 5.2.2, a cylindrical telescope is used to provide beam shaping for astigmatic focusing, which can produce waveguides with circular cross-sections given the proper writing conditions. In this section, the astigmatic difference and pulse energy are varied to determine the writing conditions that result in waveguides with circular cross-sections.

The waveguide cross-section dependence on the astigmatic difference (the distance between the beam waists in the x and y directions) was evaluated by writing a matrix of short waveguides (250μm in length) while varying the distance between the two lenses of the cylindrical telescope. The distance between the two lenses was adjusted in increments of 500 μm over a total distance of 4 mm. The writing pulse energy was fixed at 3.3 μJ and the beam was focused 500 μm below the surface of a 25 mm × 25 mm × 1 mm substrate using a 20×, 0.40 NA microscope objective. The resulting matrix is

shown in Figure 5-7. From the figure, it is apparent that not only does the cross-section vary with the astigmatic difference, but also the number and locations of the regions of refractive index change as well as the area and extent of darkening. The multiple zones of refractive index change for astigmatic differences other than zero can be explained by the separation of the focal planes in the *x* and *y* directions. The waveguide is formed at the waist in the *x*-*z* plane (ω_{0x}), while the waist in the y-*z* plane (ω_{0y}) can contribute to smaller refractive index changes or darkening away from the waveguiding region. This is illustrated in Figure 5-8, which is a simulation of the intensity profile in glass for varying the astigmatic difference over a range from 0 μm to 160 μm. When both waists are close or overlapping (i.e. astigmatic difference of zero), the modified region is elongated along the *z*-direction and the glass is darkened. As the astigmatic difference increases, ω_{0y} is shifted away from the waveguiding region (ω_{0x}). If the intensity is sufficient, material modification will occur at ω_{0y}. However, as the contour plot in Figure 5-8 shows, the intensity at ω_{0y} is significantly smaller than at ω_{0x}, so modification in this region can be eliminated by simply reducing the writing beam energy until the intensity within ω_{0y} is below the modification threshold.

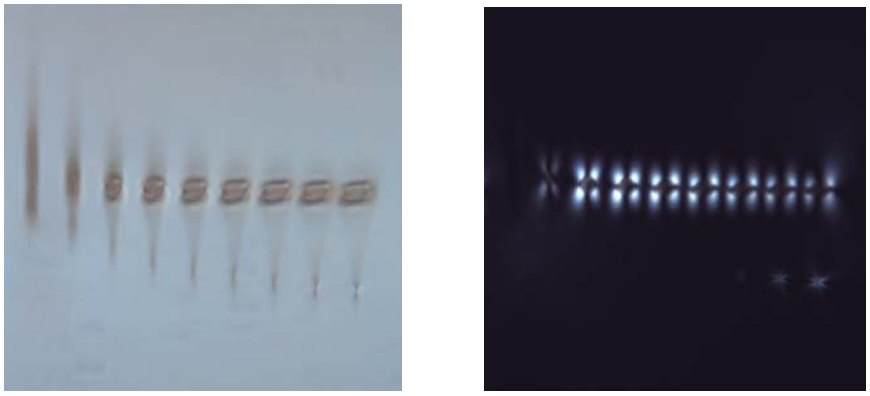

Figure 5-7. Matrix of waveguides written with varying astigmatic differences. Writing pulses are incident from the top. Left: DIC image, Right: Image through crossed polarizers.

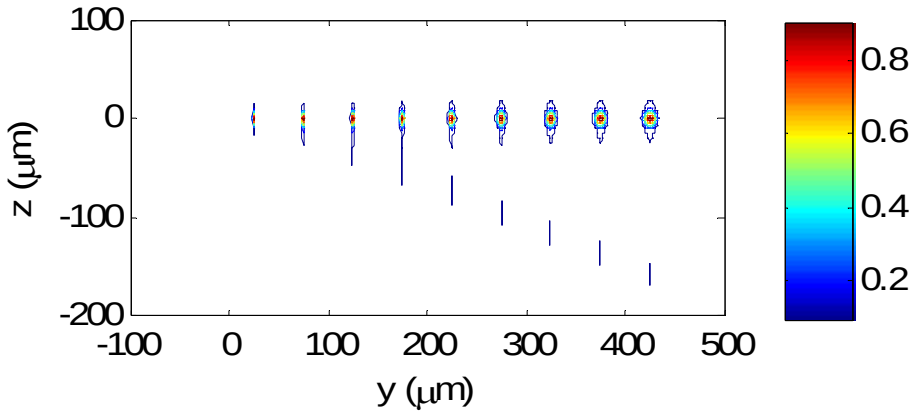

Figure 5-8. Simulation of astigmatic focusing in glass for Z_0 varied from 0 to 160μm.

The waveguide written with an astigmatic difference of 80μm (third from the left in Figure 5-7) exhibited the best circularity and was used to write a matrix of 250 μm long waveguides with pulse energies of 0.1, 0.2, 0.6, 1.1, 1.7, 2.4, 3.0, 3.3, 3.5, 4.4 and 4.5 μJ from left to right in Figure 5-9 and Figure 5-10. The DIC image in Figure 5-9 shows a long photo-darkened region above the waveguide for pulse energies greater than 1.7 μJ. Polarization microscopy of the same waveguides (Figure 5-10) indicates stress-induced birefringence for all waveguides written with pulse energies greater than 1.1 μJ, with

intensity increasing with writing pulse energy [85]. However, the photo-darkened region above the waveguides appears to remain isotropic.

Figure 5-9. DIC image of matrix of waveguides written with varying pulse energy and Z_0=40μm.

In order to characterize the modified region in the *x-z* plane, the substrate was scanned at a velocity sufficient to cause each pulse to be incident on a fresh volume of material (i.e. not overlapping with previous pulses), thereby creating single "disks" of modified glass. These "disks" are shown in Figure 5-11 for writing speeds of 5 mm/s and 2.5 mm/s from left to right respectively.

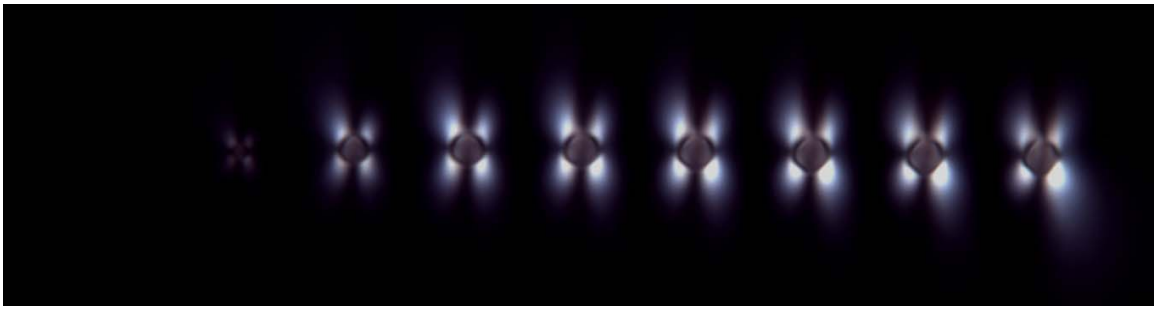

Figure 5-10. Polarization microscopy image of matrix of waveguides written with varying pulse energy and Z_0=40μm.

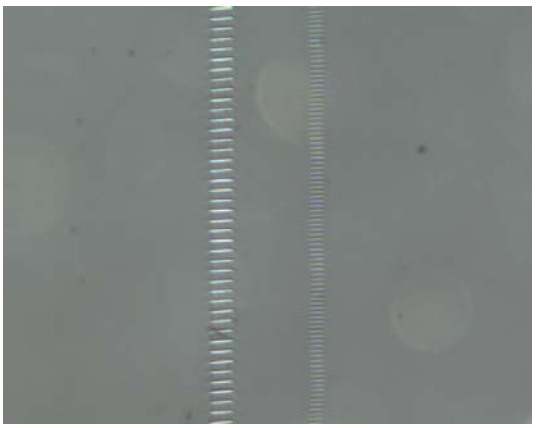

Figure 5-11: Top view DIC microscopy image of individual astigmatically-shaped femtosecond pulse modified "disk" regions in soda-lime glass. Left: 5mm/s translation speed, Right: 2.5 mm/s translation speed.

The thickness of the disk is on the order of 1 μm, which dictates that the translation speed should be < 1 mm/s achieve overlapping of successive disks. In practice, however, significant overlap is required to achieve waveguides with smooth boundaries. It is of interest to note that devices exist that make use of these types of individual regions of modification, namely type II waveguides [80] and fiber Bragg gratings [86]. However, the main focus of this research is evanescent coupling of continuous core waveguides, so they are not considered in this dissertation.

5.3.1.2 ***Near-field beam profiles versus writing pulse energy***

A series of waveguides was written with pulse energies ranging from 1.0 to 1.7 μJ and astigmatic difference of $Z_0 = 80$ μm, slightly larger than the optimum value of $Z_0 = 40$ μm that was determined in Section 5.3.1.1. The near-field beam profiles of three waveguides that were single-mode at 633 nm (measured using the setup illustrated in Figure 5-12) are

shown in Figure 5-13. The waveguides were written with pulse energies of 1.1, 1.2 and 1.3 μJ. They have a measured near-field *x*-width (*y*-width) of 14.1 μm (14.8 μm), 12.7 μm (13.2 μm) and 11.8 μm (12.0 μm) respectively.

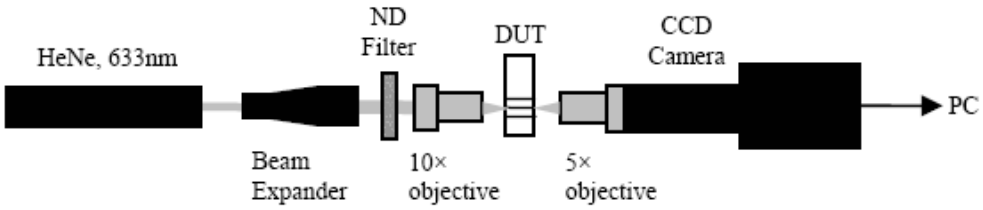

Figure 5-12. Setup for examining the waveguide near-field beam profiles at 633nm.

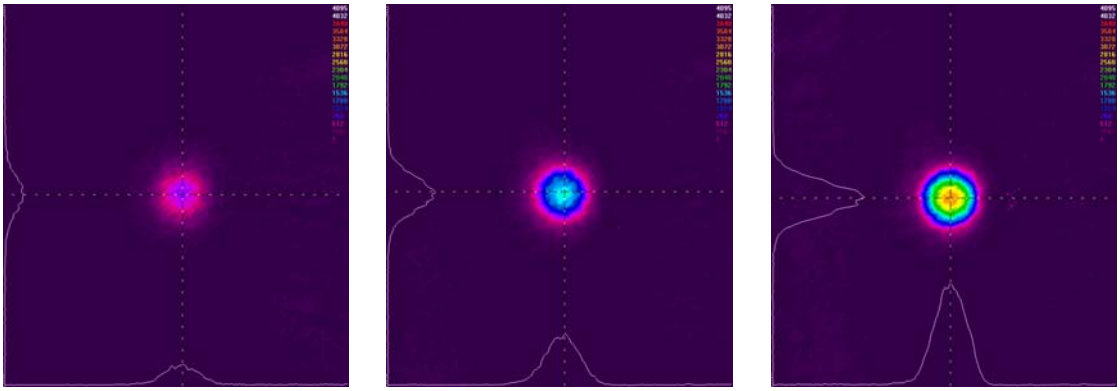

Figure 5-13. Near-field beam profiles of single-core waveguides written with translation speeds of 20 μm/s and pulse energies of 1.1, 1.2 and 1.3 μJ from left to right respectively.

5.3.1.3 Index change (Δn) versus writing pulse energy

The numerical apertures of the waveguides in Figure 5-13 were measured using the method described in [87]. The induced refractive index change, Δn was estimated from the measured numerical apertures using the equation $NA = \sqrt{2n\Delta n}$ which applies for step-index waveguides with small Δn [87]. Here, n is the refractive index of the soda-lime glass substrate. The Δn for the three waveguides in Figure 5-13 was estimated to be

0.7×10^{-3}, 1.0×10^{-3} and 1.3×10^{-3} for the 1.1, 1.2 and 1.3μJ waveguides respectively (NA = 0.046, 0.056 and 0.062 respectively).

5.3.1.4 ***Color Center Characterization***

As mentioned in section 2.4.1, color centers in soda-lime glass are attributed to trapped hole centers which link non-binding oxygen holes and neutral Na atoms. The color centers induced in short waveguides in the soda-lime glass were characterized using Laser Scanning Confocal Microscopy (LSCM). A matrix of 250 μm long waveguides was written at 20 μm/s with writing pulse energy varied from 0.03 to 4.5 μJ. The waveguides were scanned with 488 nm light from an Ar^+ laser, which caused fluorescence of the non-bridging oxygen hole centers at 620 nm [30]. The fluorescent light was passed through a filter with a passband > 510 nm and measured with a photomultiplier tube (PMT). The resulting scanned image from the PMT is shown in Figure 5-14. The fluorescent intensity is clearly proportional to the writing pulse energy.

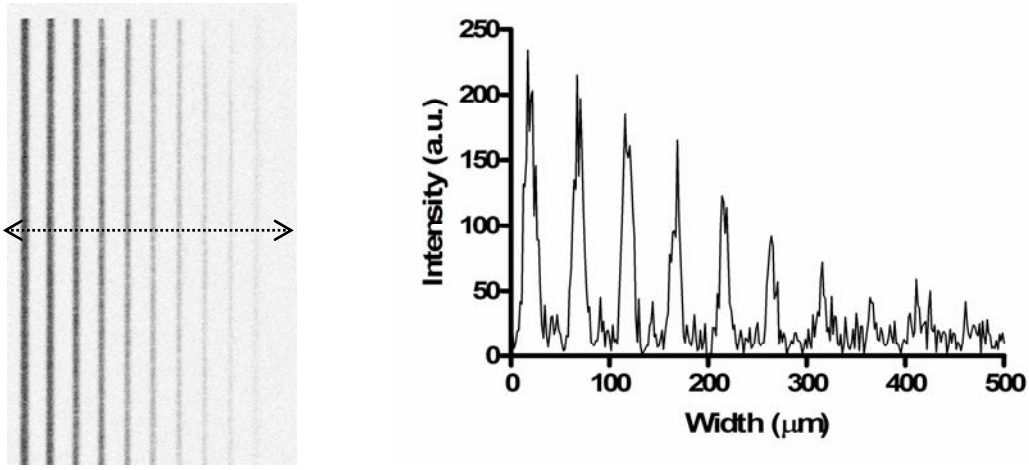

Figure 5-14. Laser Scanning Confocal Microscopy (LSCM) image of waveguides; Left: dark areas indicate fluorescence from color centers. The writing pulse energy from left to right was: 4.5, 4.4, 3.5, 3.3, 3.0, 2.4, 1.7, 1.1, 0.5, 0.15 and 0.03 μJ; Right: color center fluorescent intensity

LSCM is also useful for determining the cross-sections of color-center containing waveguides. Five waveguides written with translation speeds of 20 μm/s, pulse energies of 5 μJ and varying astigmatic differences, were scanned at 21 planes throughout their depth and images were stacked and interpolated to determine the waveguide cross-sections. The resulting images are shown in Figure 5-15.

Further confirmation of fluorescent color centers in femtosecond direct-written soda-lime glass waveguides was obtained by end-fire coupling 532 nm light from a diode-pumped solid-state laser. Florescence from color centers causes the waveguide to appear orange when viewed from the side using a stereoscope as shown in Figure 5-16.

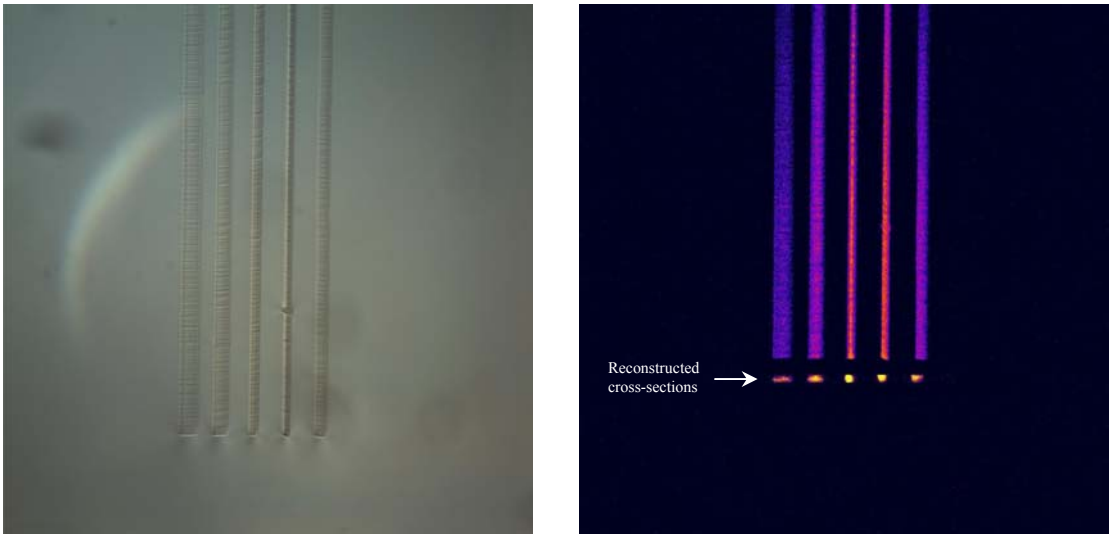

Figure 5-15: Waveguides written in soda-lime glass with astigmatically-shaped femtosecond pulses. The astigmatic difference was adjusted for each waveguide to determine the effect on the waveguide cross-section. Left: DIC microscopy image of waveguides. Right: Laser Scanning Confocal Microscopy (LSCM) false-color image of waveguide fluorescence. Reconstructed waveguide cross-sections from z-stack are also shown.

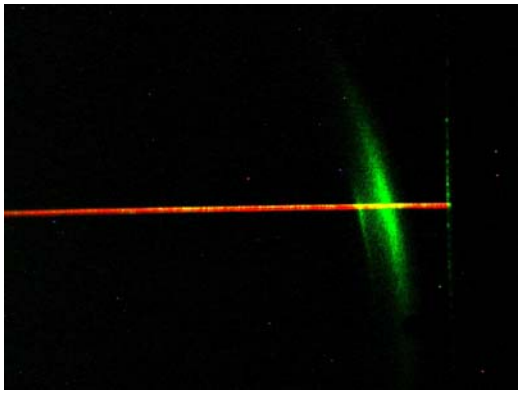

Figure 5-16. Side image taken with CCD camera of waveguide in soda lime glass with 532 nm end-fire coupled with 5x objective. The waveguide appears orange due to fluorescent color centers formed during waveguide writing.

5.3.2 **Evanescently Coupled Waveguide Arrays**

In this section, the supermode beam profiles of 3- and 7-core waveguides arrays in soda-lime glass are examined as a function of the center core properties. Diffraction properties are also determined for a short 7-core array.

*5.3.2.1 **3-core Array***

In order to evaluate the effect of the center core properties on the array, three linear, 3-core arrays were written in 1 mm thick soda-lime glass substrates with identical outer cores and either smaller, equivalent or larger center cores. The outer cores were written with 1.2 μJ pulses, the smaller center core was written with 1.1 μJ pulses and the larger center core was written with 1.3 μJ pulses. All waveguides were written with a translation speed of 20 μm/s at a depth of 500 μm below the substrate surface using a focused astigmatic beam with $Z_0 = 80$ μm. The length of each array was 12 mm and the center-to-center waveguide spacing was 15 μm. Beam profiles of each of the individual waveguides used to form the arrays are shown in Figure 5-13.

The waveguide end faces were polished and light from a HeNe laser at a wavelength of 633nm was endfire coupled into the center core of each of the arrays using a 5× microscope objective with a numerical aperture of 0.09. The near-field beam profiles, recorded at the output of each array, are shown in Figure 5-17 and Figure 5-18.

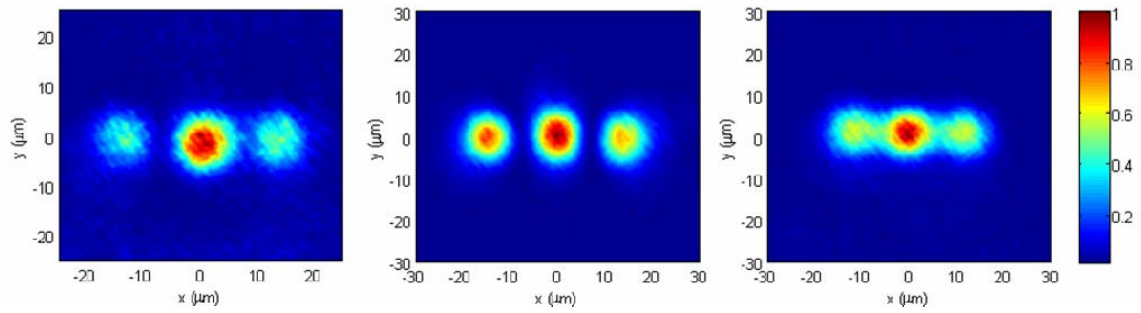

Figure 5-17. Near-field beam profiles of 3-core waveguide arrays with 15 μm center-to-center core spacing. Left – all cores written with 1.2 μJ, Middle – outer waveguides written with 1.2 μJ, middle core written with 1.1 μJ, Right – outer waveguides written with 1.2 μJ, middle core written with 1.3 μJ. The writing speed for all waveguides was 20 μm/s.

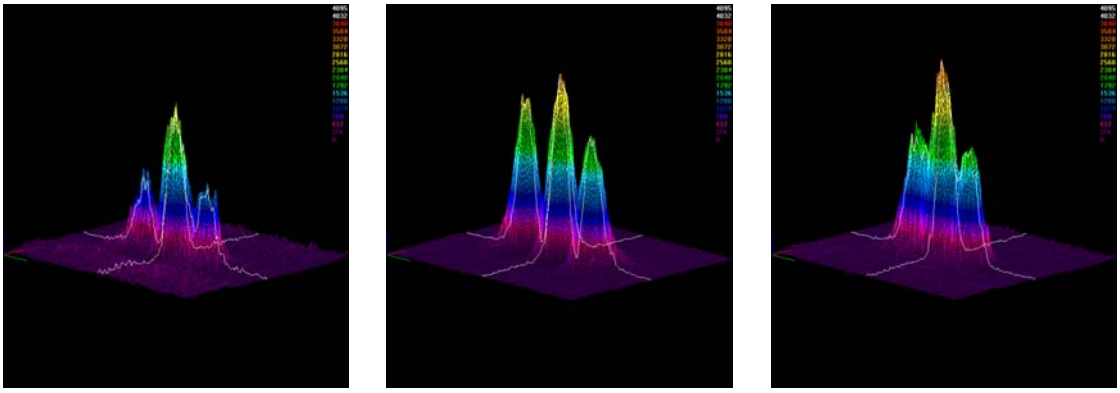

Figure 5-18. 3-D views of waveguides in Figure 5-17.

Beam profiles of the fundamental supermode, calculated using the SMM with input parameters determined from single waveguide measurements, are plotted in Figure 5-19.

The model results are in good qualitative agreement with the observed experimental profiles.

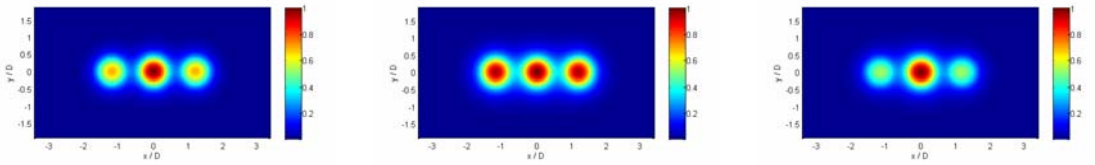

Figure 5-19. Scattering Matrix Method model of fundamental supermode for 3-core array

5.3.2.2 ***7-core Array***

Three isometric, 7-core arrays were written in 1 mm thick soda-lime glass substrates with identical outer cores and either smaller, equivalent or larger center cores. The outer cores were written with 1.2 μJ pulses, the smaller center core was written with 1.1 μJ pulses and the larger center core was written with 1.3 μJ pulses. All waveguides were written with a translation speed of 20 μm/s at a depth of 500 μm below the substrate surface. In this case, however, the astigmatic difference was set to the optimum value determined in Section 5.3.1.1 of $Z_0 = 40$ μm. The length of each array was 12 mm and the center-to-center waveguide spacing was 15 μm for each array.

As for the 3-core arrays, the waveguide end faces were polished and light from a HeNe laser at a wavelength of 633 nm was end-fire coupled into the center core of each of the arrays using a 5× microscope objective with a numerical aperture of 0.09. The near-field beam profiles, recorded at the output of each array, are shown in Figure 5-20 and Figure 5-21. The waveguides appear to support the higher-order LP_{11} mode in addition to the fundamental mode at 633 nm. The LP_{11} mode was also excited for 775 nm coupling (data not shown). The likely cause that the waveguides are multimode is

that the refractive index of the core was likely increased above the measured values in Section 5.3.1.3 when the astigmatic difference was changed from $Z_0 = 80$ μm to $Z_0 = 40$ μm given the same writing pulse energies. One trend that is clear in the three arrays is the stronger confinement of light to the central core as its writing pulse energy is increased.

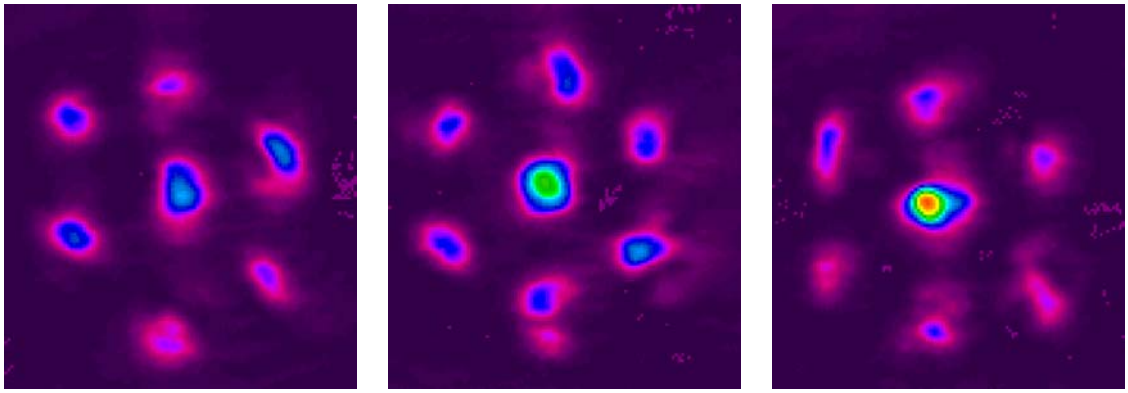

Figure 5-20. Near-field beam profiles of 7-core waveguide arrays femtosecond-written in soda-lime glass. A 633 nm HeNe beam is endfire coupled. The waveguides are 12 mm long, spaced 15 μm center-to-center. All outer cores are written with 1.2 μJ pulse energy. Center cores are written with pulse energies of 1.1, 1.2 and 1.3 μJ for the arrays on the left, middle and right respectively. The writing speed for all waveguides was 20 μm/s. The astigmatic difference was $Z_0 = 40$ μm.

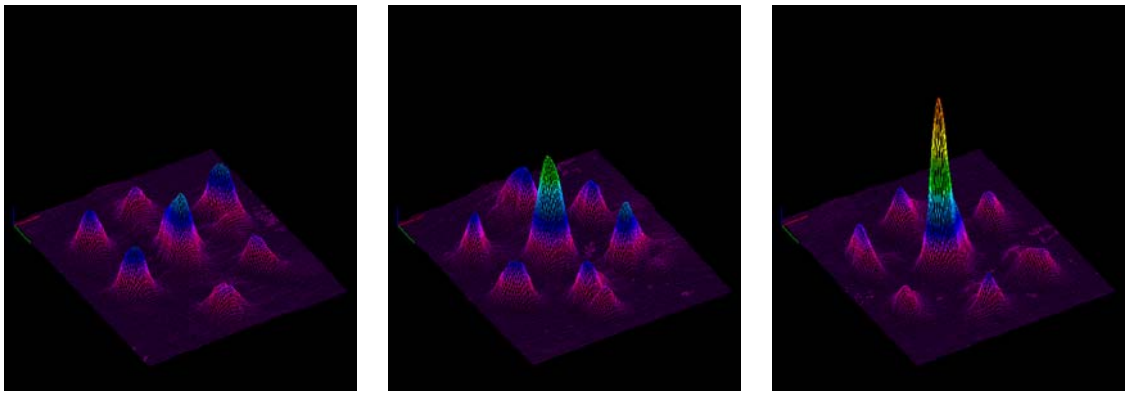

Figure 5-21. 3-D views of waveguides in Figure 5-20.

5.3.2.3 ***Far-field Analysis***

In addition to the 12 mm long 7-core arrays in Section 5.3.2.2, short (250 μm long) 7-core arrays were also written under the same conditions. A polarization microscopy image of the cross-section of an array with all cores written with 1.2 μJ pulses is shown in Figure 5-22. The array was end-fire coupled with 532 and 633 nm light from a diode-pumped solid-state and HeNe laser respectively using a 5× microscope objective with a numerical aperture of 0.09. The far-field diffraction pattern that resulted from simultaneous coupling of the two laser sources is shown in Figure 5-22. The central lobe appears white due to high on-axis intensity. Also, the angle of diffraction is greater for the longer wavelength (633 nm) light as expected. The diffraction was modeled using Fraunhofer's diffraction theory with each core assumed to be identical with equal field strength [88]. Figure 5-23 shows the comparison between the simulated and experimentally observed far-field for 532 nm coupling at a distance of 380 mm from the array output. Figure 5-24 shows the comparison for 633 nm coupling. Reasonable qualitative agreement is found between the measured and experimental profiles for both cases.

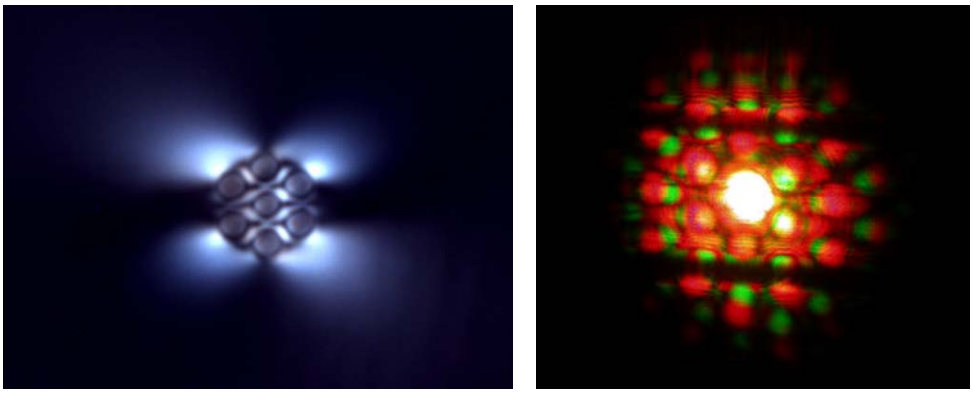

Figure 5-22. (Left) Polarization microscopy image of 250 µm long, 7-core array end face. (Right) Far-field pattern from 250 µm long, 7-core array with simultaneous excitation of 532 and 633 nm at a distance of 380 mm from the array output

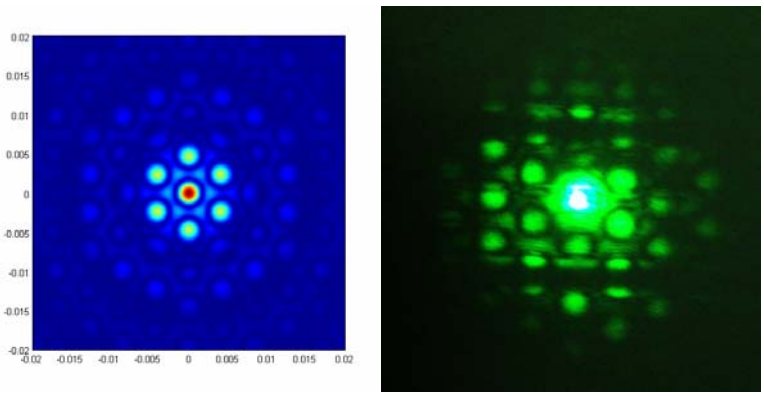

Figure 5-23. Comparison of simulated (left) and experimental (right) far-field intensity profiles from a 250 µm long, 7-core array with 532 nm excitation at a distance of 380 mm from the array output

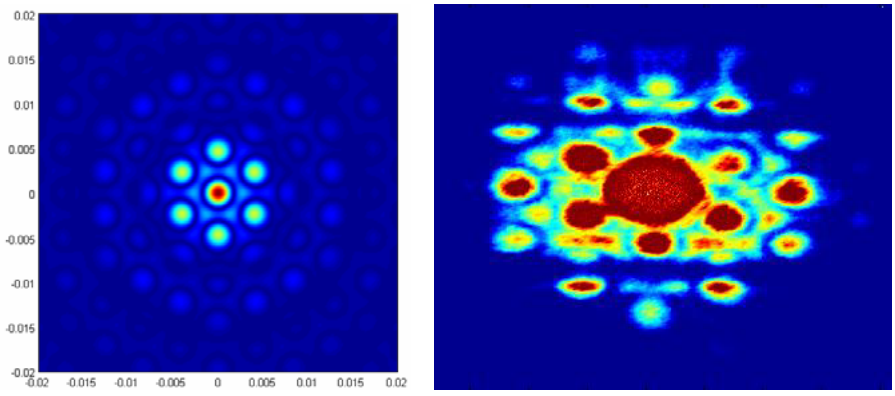

Figure 5-24. Comparison of simulated (left) and experimental (right) far-field intensity profiles from a 250 µm long, 7-core array with 633 nm excitation at a distance of 380 mm from the array output

5.4 High-Purity Fused Silica (HPFS) Waveguides

Fused silica is widely used in the fabrication of optical fibers and waveguides due to its high damage threshold, low optical loss and low absorption. The substrates used in this section are 25 mm × 12 mm × 1 mm HPFS® Standard Grade, Corning code 7980, which is a high purity synthetic amorphous silicon dioxide manufactured by flame hydrolysis [89]. As in the previous section, waveguides are directly written in the substrates using femtosecond laser pulses. Waveguides are characterized based on cross-section, refractive index change and mode quality. Three single-mode waveguides with different mode-field diameters are selected and used to investigate supermode tailoring and discrete diffraction in waveguide arrays. Arrays with common central cores, comprising 3-, 4- and 7-cores are investigated.

5.4.1 Single Waveguide Characterization

As in the case of the soda-lime glass waveguides, three single-mode waveguides are needed that vary in diameter and/or refractive index in order to fabricate waveguide arrays. Experimental matrices were set up to determine firstly, the proper cylindrical telescope lens spacing and astigmatic difference for producing circularly symmetric waveguides and secondly, the proper writing pulse energy to ensure single-mode operation.

5.4.1.1 Waveguide Shaping Using Astigmatic Focusing

A series of waveguides were written for varying astigmatic differences (Z_0) as in Section 5.3.1.1. Short waveguides, 250 μm in length were written at a pulse energy of 2 μJ and a

translation speed of 20 μm/s, 500 μm below the surface of the substrate. The waveguide end faces were then polished, etched in 36 wt. % hydrofluoric acid (HF) for 10 minutes to selectively etch the higher index waveguiding regions [90] and then sputter coated with platinum. A scanning electron micrograph of the waveguide cross-sections is shown in Figure 5-25. The arrow indicates that the value of Z_0 chosen to write waveguides with cylindrical cross-sections was between the values used to write the two adjacent waveguides. In this case, Z_0 = 50 μm resulted in symmetric waveguide cross-sections.

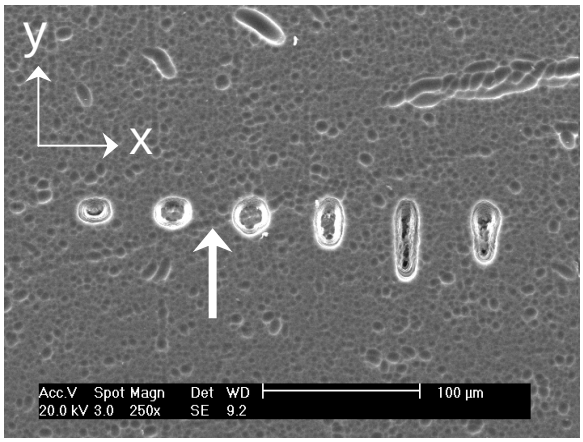

Figure 5-25. Waveguide cross-sections for varying astigmatic difference, Z_0.

5.4.1.2 Index change (Δn) versus writing pulse energy

The refractive indices of waveguides written with pulse energies ranging from 1.1 to 1.5μJ were determined using the same method as in 5.3.1.3, whereby the refractive index is determined from numerical aperture measurements. The index change, Δn, is plotted in Figure 5-26 as a function of writing pulse energy. The shaded region in the figure represents waveguides that support multiple modes at a wavelength of 775 nm and are therefore not considered for this study. The three waveguides written with pulse energies

of 1.1, 1.15 and 1.2 μJ, however, were single-mode at 775 nm. These waveguides were selected for fabricating arrays. More in-depth characterization of their properties follows.

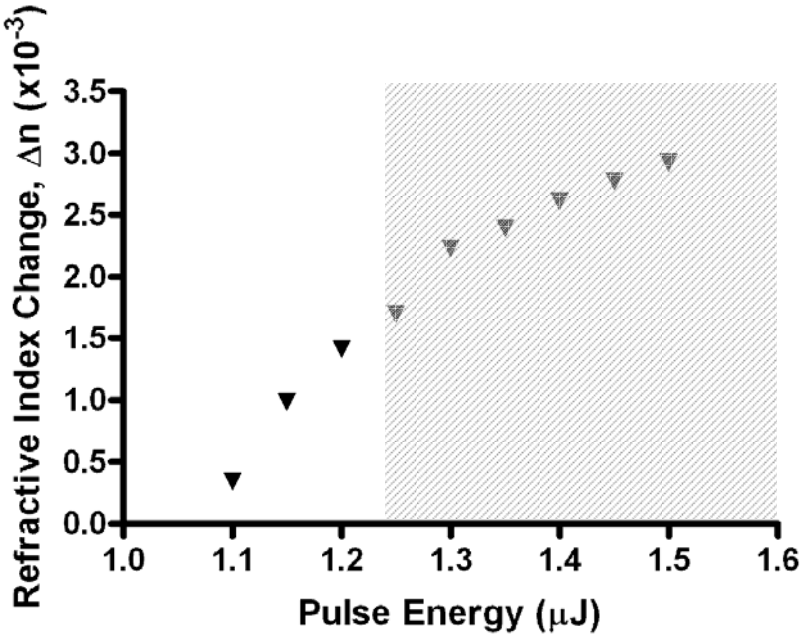

Figure 5-26. Induced refractive index change as a function of writing pulse energy.

5.4.1.3 ***Microscopy of Single-Mode Waveguides***

Cross-sections of the single-mode waveguides written with pulse energies of 1.1, 1.15 and 1.2 μJ were examined by polishing the end-faces, etching in 36 wt. % hydrofluoric acid (HF) for 10 minutes, sputter coating with platinum and imaging in a scanning electron microscope (SEM). Core diameters, measured from scanning electron micrographs (Figure 5-27), were 4.9, 9.0 and 9.6μm for the waveguides written with 1.1, 1.15 and 1.2μJ pulses respectively. The aspect ratios for all waveguides were on the order of 1.1 to 1.0 (*x to y*). The uniformity of the waveguides can be seen in the differential interference contrast microscope image taken from the side (Figure 5-28).

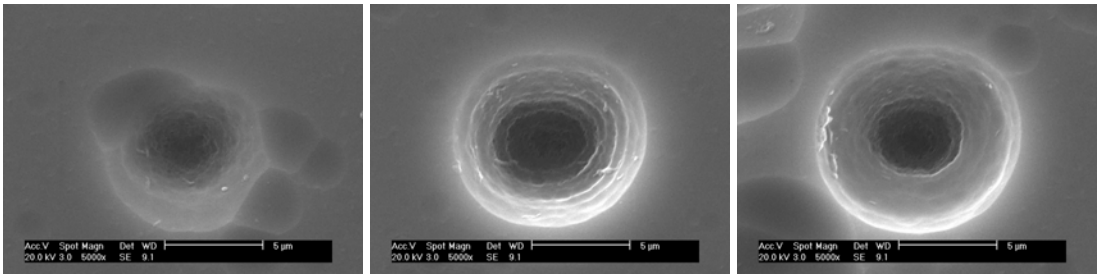

Figure 5-27 Waveguide cross-sections for fixed Z_0 and writing pulse energy of 1.1, 1.15 and 1.2 μJ from left to right respectively.

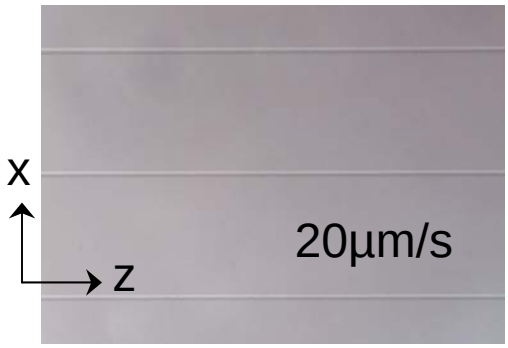

Figure 5-28. DIC image of waveguides written with translation speed of 20 μm/s and pulse energies of 1.2, 1.15 and 1.1 μJ from top to bottom respectively.

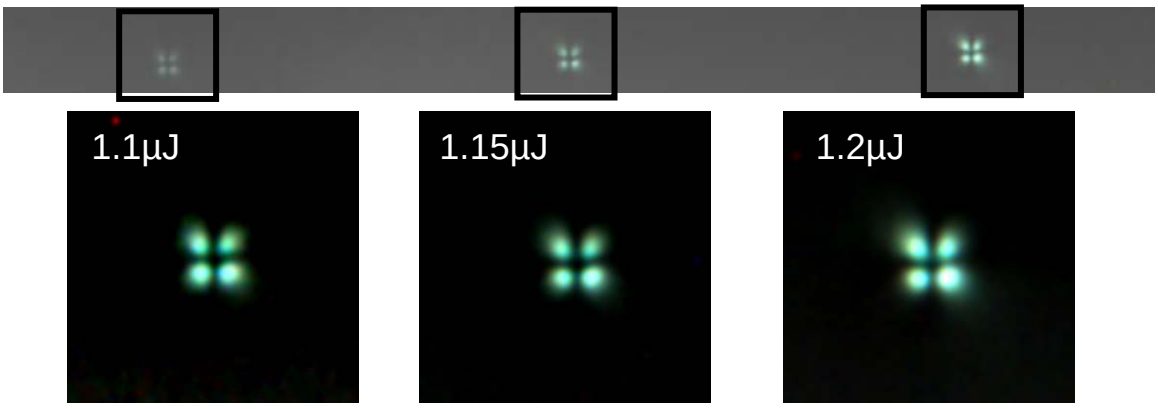

Figure 5-29. Polarization microscopy images of waveguide cross-sections for 250 μm long waveguides written with pulse energies of 1.1, 1.15 and 1.2 μJ from left to right respectively.

The waveguide end faces of short (250µm long) sections were also examined using polarization microscopy in order to observe their interference figures. The intensity of the interference patterns for each of the waveguides in Figure 5-29 increased with increasing writing pulse energy, indicating stress-induced birefringence similar to the case discussed in Section 5.3.1.1.

*5.4.1.4 **Near and Far-field Beam Profiles of Single-Mode Waveguides***

Near-field beam profiles of each of the three single-mode waveguides for 775 nm coupling are shown in Figure 5-30. The output is symmetric with the degree of field confinement to the core increasing with increasing core refractive index.

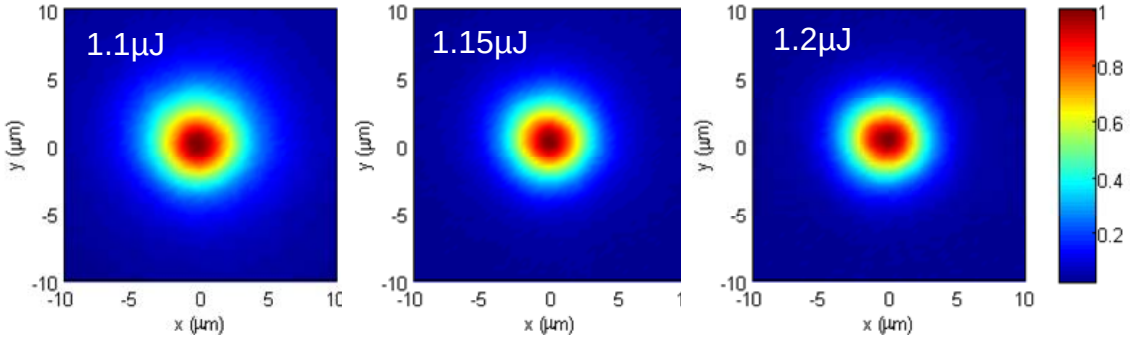

Figure 5-30. Near-field beam profiles of 11 mm long waveguides written with pulse energies of 1.1, 1.15 and 1.2 µJ from left to right respectively.

The far-field beam profiles of each of the arrays for 633 nm coupling are shown in Figure 5-31. The fringes are due to interference between the guided and un-coupled pump light and were used to estimate the core refractive index in Section 5.4.1.2. The fringes extend farther away from the center for increased writing pulse energy due to increased refractive index and numerical aperture.

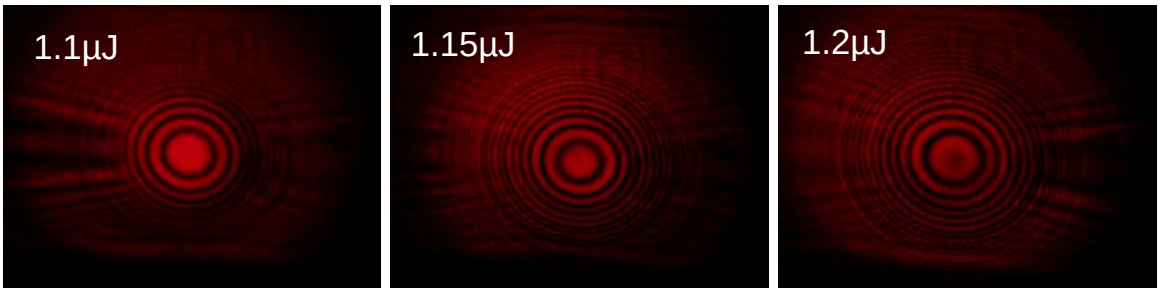

Figure 5-31. Far-field beam profiles of 11mm long waveguides written with pulse energies of 1.1, 1.15 and 1.2μJ from left to right respectively.

5.4.1.5 ***Waveguide Loss***

Waveguide loss was estimated using the scattering technique described in [91]. In the technique, it is assumed that the intensity normal to a given point along a waveguide is proportional to the intensity of light in the waveguide at that point. Mapping of the decay of intensity along the waveguide will therefore give the loss coefficient. Given the equation

$$\ln\left(I_L\right) = \ln\left(I_0\right) - \alpha L \tag{5.1}$$

where I_L is the scattered intensity after a propagation length L, I_0 is the initial intensity and α is the loss coefficient to be determined [91], it is possible to calculate α if the scattered intensity along the waveguide is known. Scattered intensity was extracted from images of the waveguides taken with 633 nm coupling using a camera attached to a stereoscope. An image of the scattered intensity from the 1.15 μJ waveguide is shown in Figure 5-32. The intensity was sampled over a 6 mm long section of the waveguide as indicated by the rectangular box; the region was chosen away from the input and output facets to exclude the large amount of scattered light in those areas.

A linear fit to the scattered intensity is shown in Figure 5-33. The retrieved loss coefficient was α = 0.1 cm^{-1}, which corresponds to a loss of 0.45 dB/cm. This is comparable to typical values reported in the literature [28].

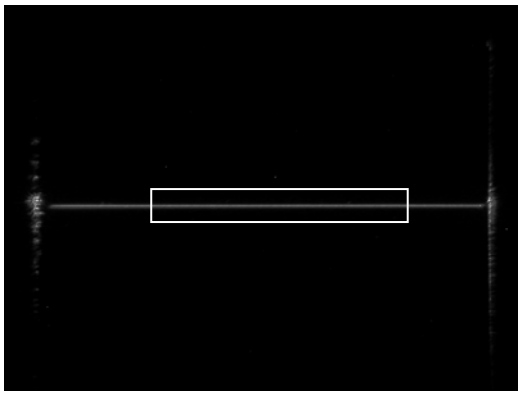

Figure 5-32. Top view of 633nm light scattering for waveguide written with 1.15μJ pulses.

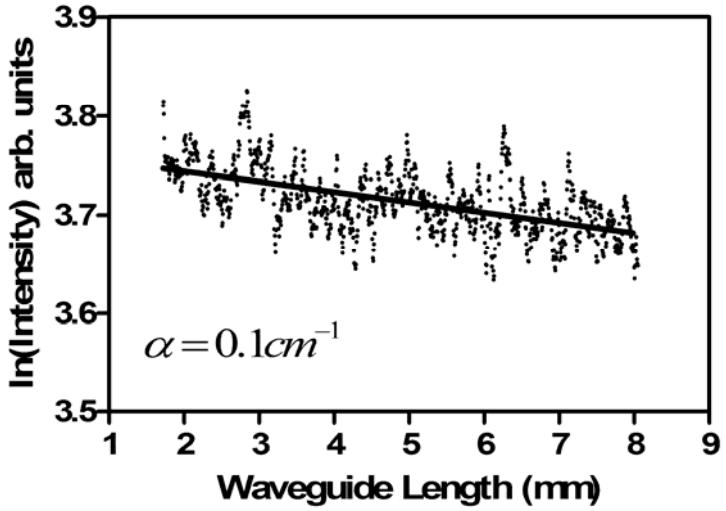

Figure 5-33. Scattered intensity along the length of the waveguide in Figure 5-32.

5.4.2 **Evanescently Coupled Waveguide Arrays**

In this section, waveguide arrays with 3-, 4-, and 7-cores are evaluated. Similar to the experiments for soda-lime glass, three arrays of each type are fabricated to investigate the effect of varying the center core properties on the array.

5.4.2.1 Three-Core Array

Three linear, 3-core arrays were written in 1 mm thick high-purity fused silica substrates with identical outer cores and either smaller, equivalent or larger center cores. The outer cores were written with 1.15 μJ pulses, the smaller center core was written with 1.1 μJ pulses and the larger center core was written with 1.2 μJ pulses. All waveguides were written with a translation speed of 20 μm/s at a depth of 500 μm below the substrate surface using a focused astigmatic beam with $Z_0 = 50$ μm. The length of each array was 10.3 mm and the center-to-center waveguide spacing was 10.5 μm for each array. Polarization microscopy images of each of the arrays are shown in Figure 5-34.

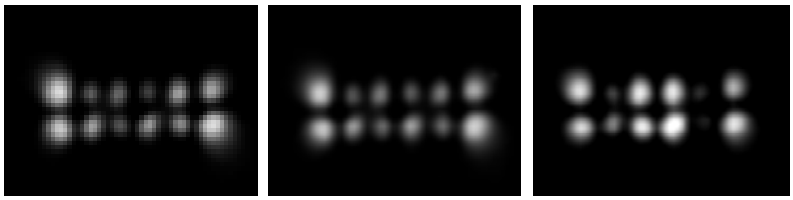

Figure 5-34. Polarization microscopy images of 3-core waveguide arrays with outer cores written with 1.15 μJ pulses and center cores written with 1.1, 1.15 and 1.2 μJ pulses from left to right respectively.

The waveguide end faces were polished and light from a HeNe laser at a wavelength of 633 nm was end-fire coupled into the center core of each of the arrays using a 5× microscope objective with a numerical aperture of 0.09. The near-field beam profiles,

recorded at the output of each array, are shown in Figure 5-35. For comparison, the fundamental supermodes, calculated from the SMM, are plotted in Figure 5-36.

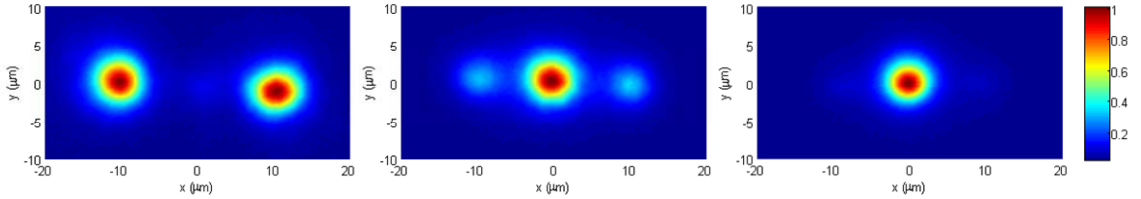

Figure 5-35. Experimental near-field output beam profiles from 3-core array. Left: smaller center core, Middle: all cores equivalent, Right: larger center core

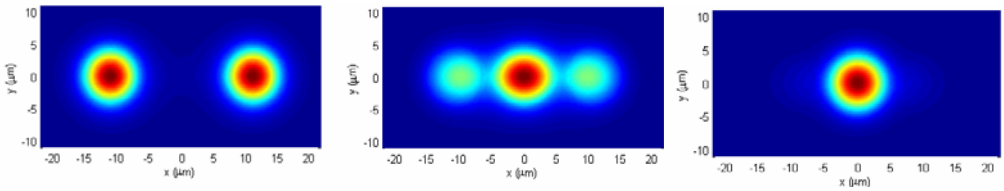

Figure 5-36. SMM simulated near-field output beam profiles of the fundamental supermode for the 3-core array. Left: smaller center core, Middle: all cores equivalent, Right: larger center core

In a perfectly symmetric array, coupling to the center core at the waveguide array input will excite both the fundamental, in-phase supermode (LP_{01}) as well as the anti-phase supermode (labeled LP_{21} in Figure 3-3) in which the center core is π out of phase with the outer cores. Power will then be transferred back and forth between the center and outer cores along the length of the array with a beat length determined by the difference in the supermode propagation constants. In order to determine the power coupling among the cores in the array along its length, a 10× microscope objective attached to a CCD camera was scanned along the length of the array. Images that were 540 µm wide were taken every 500 µm so that a composite image of the scattered intensity could be obtained. As shown in Figure 5-37, the beam is coupled to the center core on the left where the

intensity is highest. Maximum transfer of power from the center core to the outer cores occurs at approximately 2.5 mm after the input, after which the power is transferred back into the center core and the process repeats. Coupled mode analysis was used to simulate the coupling using measured properties of the waveguides combined with the results from the SMM analysis. The simulated power coupling along the length of the array is shown in Figure 5-38.

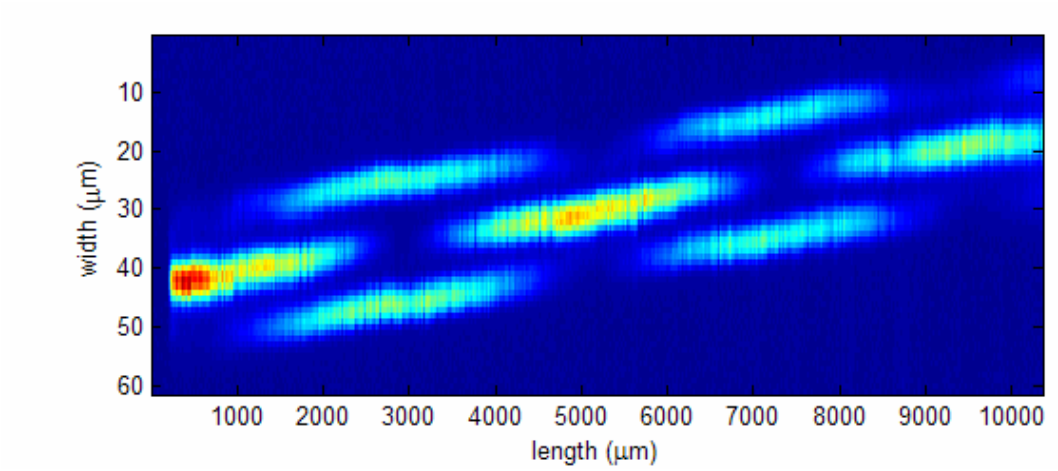

Figure 5-37. Composite image of scattered intensity along 3-core array with 633 nm light coupled to the center core

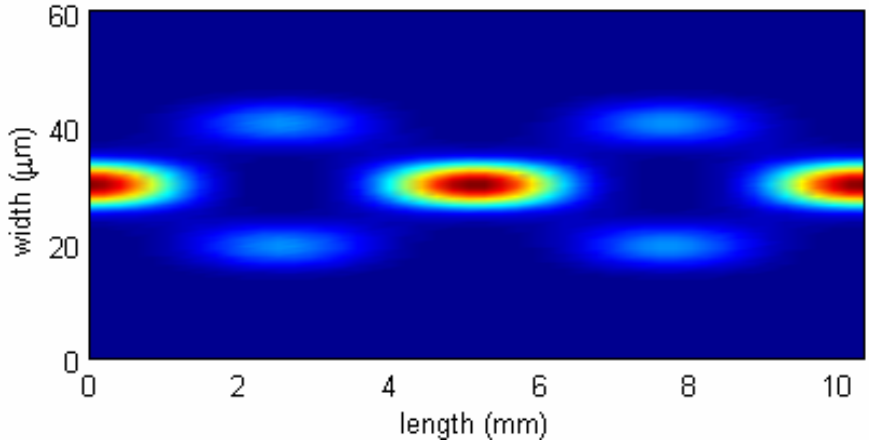

Figure 5-38. Coupled mode analysis simulation of the array power coupling

Good qualitative agreement is found with the main difference being that the model does not take into account waveguide loss, which is apparent in Figure 5-37. In an effort to obtain a more quantitative analysis comparing the experimental and simulated data, the scattered intensity for each individual waveguide was plotted along the length of the array in Figure 5-39. The simulated normalized power along the length of the array is plotted in Figure 5-40. The coupling length for the experimental waveguides is approximately 2.5 mm, while the coupling length for the simulated array is 2.56 mm. Also, the minima in the experimental plot are close to zero, indicative of a very small difference in the propagation constants of individual waveguides.

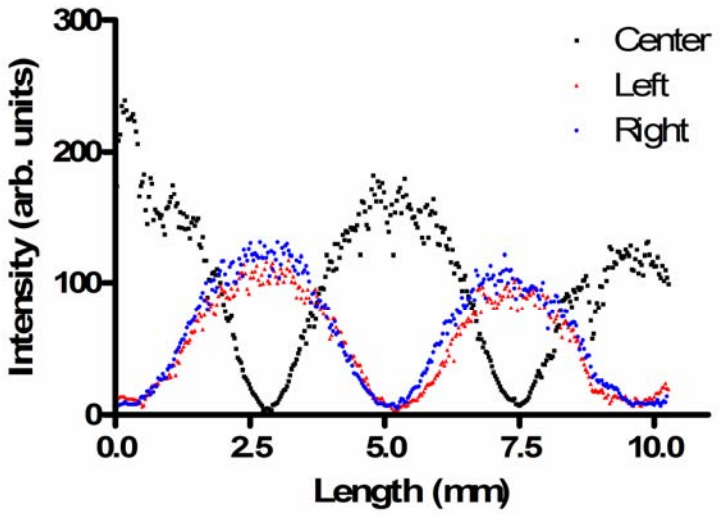

Figure 5-39. Scattered intensity for individual waveguides of the 3-core array

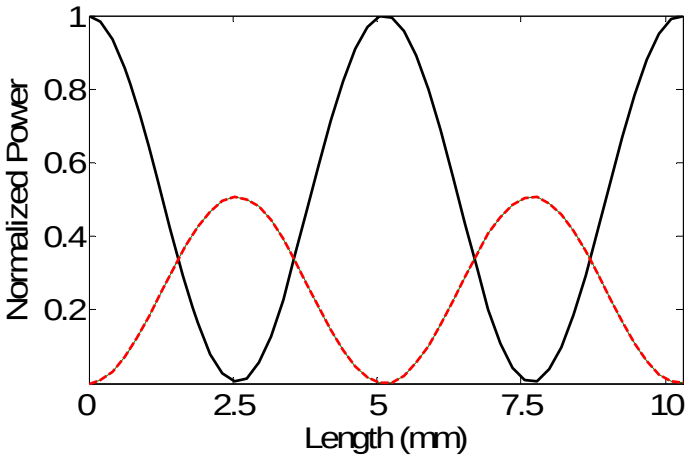

Figure 5-40. Simulated normalized power along the length of the 3-core array. Black (solid line): Center core, Red (dashed line) outer cores

5.4.2.2 ***Four-Core Array***

Three 4-core arrays in a triangular configuration were written in 25 mm × 12 mm × 1 mm Corning 7980 high purity fused silica substrates with identical outer cores and either smaller, equivalent or larger center cores [14]. The outer cores were written with 1.15 μJ pulses, the smaller center core was written with 1.1 μJ pulses and the larger center core was written with 1.2 μJ pulses. All waveguides were written with a translation speed of 20 μm/s at a depth of 500 μm below the substrate surface using a focused astigmatic beam with Z_0 = 50 μm. Since the damage threshold of the fused silica is significantly lower at the air interface than in the bulk, waveguides were written 200μm away from the substrate edge in order to reduce the intensity of the coupled light on the input facet. The length of each array was 11 mm and the center-to-center waveguide spacing was 12 μm for each array. Polarization microscopy images of each of the arrays are shown in Figure 5-41.

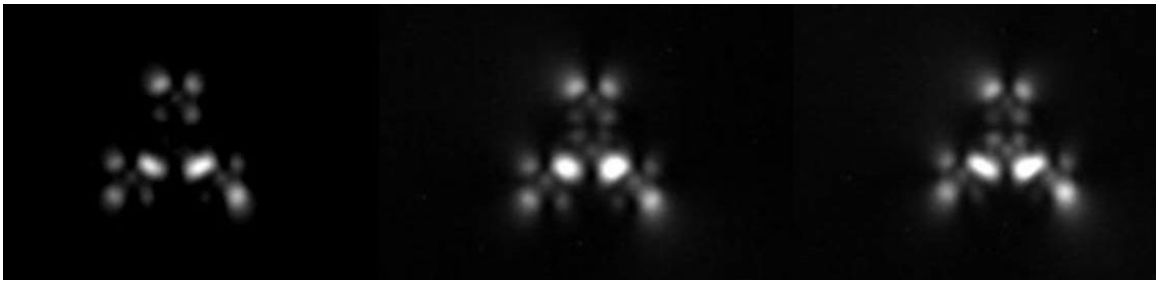

Figure 5-41. Polarization microscopy images of 4-core waveguide arrays with outer cores written with 1.15μJ pulses and center cores written with 1.1, 1.15 and 1.2 μJ pulses from left to right respectively.

The waveguide end faces were polished and 775 nm, 135 fs pulses were endfire coupled into the center core of each of the arrays using a 5× microscope objective with a numerical aperture of 0.09. The input pulse energy was on the order of 1 nJ for all cases tested. The near-field beam profiles, recorded at the output of each array, are shown in Figure 5-42. For comparison, the fundamental supermodes, calculated from the SMM, are plotted in Figure 5-43. Although the theoretical fundamental supermode profiles and experimental beam profiles are qualitatively similar, it is expected that due to the coupling and excitation of the center core at the input, at least two supermodes (namely, the symmetric and anti-symmetric) supermodes are propagating in the array. Numerical coupling analysis confirms that the output would look similar to the profiles in Figure 5-42 given the waveguide length of 11 mm and excitation of both the LP_{01} and LP_{21} supermodes. Also, the near-zero minima between the waveguide cores for the all-cores-equivalent experimental profile in Figure 5-42 suggests the presence of the LP_{21} supermode.

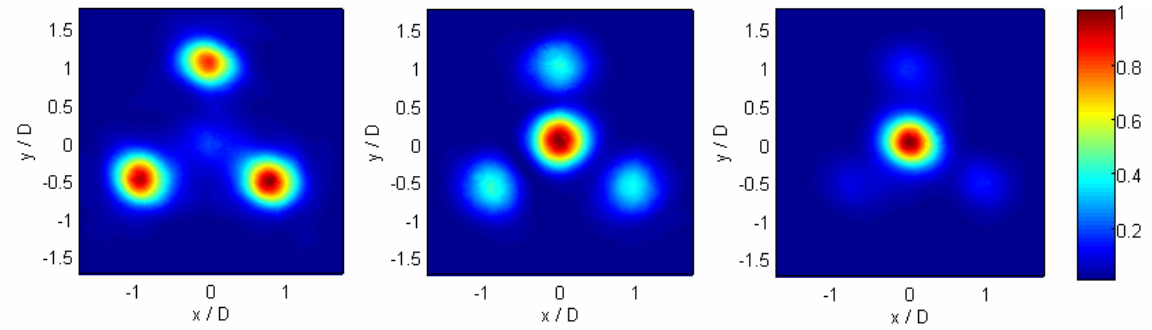

Figure 5-42. Experimental near-field output beam profiles from 4-core array. Left: smaller center core, Middle: all cores equivalent, Right: larger center core

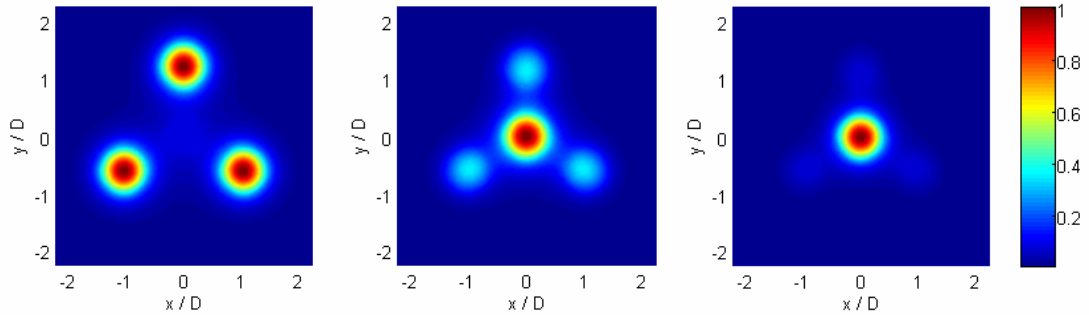

Figure 5-43. SMM simulated near-field output beam profiles of the fundamental supermode for the 4-core array. Left: smaller center core, Middle: all cores equivalent, Right: larger center core

5.4.3 **Femtosecond Pulse Delivery**

In this section, femtosecond pulses are coupled into femtosecond direct-written waveguides and 7-core waveguide arrays. The output spectra, energy transmission, temporal dynamics and beam profiles are recorded as a function of input pulse energy.

5.4.3.1 Femtosecond Pulses in Single-Core Waveguides

Femtosecond pulses were endfire coupled into three 11 mm long, single waveguides in HPFS that were direct-written with writing pulse energies of 1.1, 1.15 and 1.2 μJ, labeled small, medium and large respectively in the following figures. The properties of the femtosecond pulses are listed in Table 4-1 and the same experimental setup was used as

in Section 4.1.2.1. Pulses were also transmitted through 12 mm of bulk HPFS as a control. The measured energy transmission through the three waveguides and bulk HPFS as a function of input energy is plotted in Figure 5-44. The transmitted energy was similar for all three waveguides, with slightly greater variation occurring above an input energy of 1600 nJ. The transmitted energy through bulk HPFS, however, was about half that transmitted through the waveguides up to an input energy of 2400 nJ, above which the detected energy increased rapidly. This increase is likely due to either an in induced refractive increase in the HPFS which acted as a waveguide and increased the light coupled to the detector, the onset of self-focusing or both.

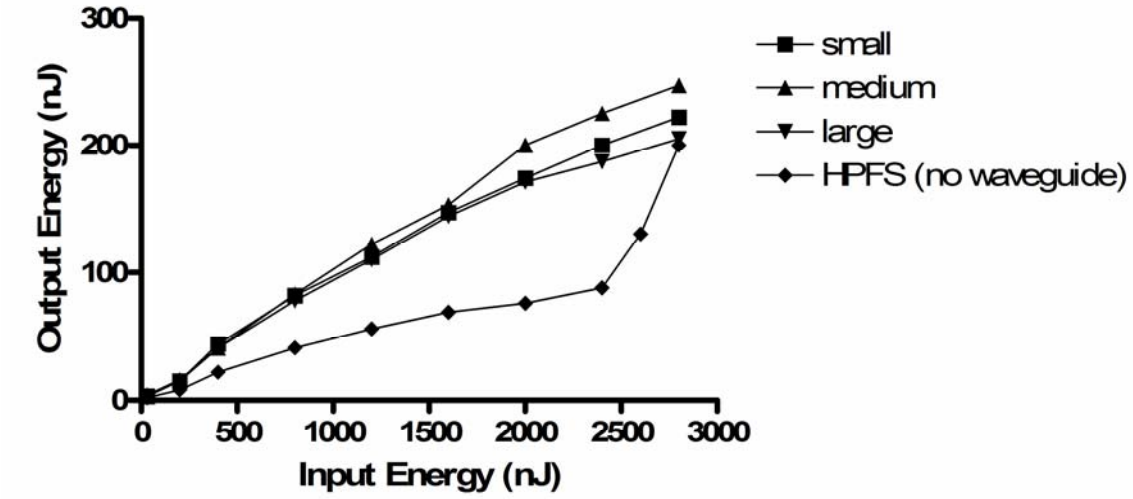

Figure 5-44. Transmission through single-core femtosecond direct-written waveguides

The output spectra for HPFS only coupling is shown in Figure 5-45. A slight broadening and blue-shifting is present at higher input energies. The output spectra for each of the single waveguides as a function of input energy are shown in Figure 5-46. The effect of self-phase modulation can clearly be seen through the increase in the

number of peaks as the input energy is increased. The maximum nonlinear phase shift, $\phi_{\max}$ can be deduced from the number of peaks, M as [18]

$$\phi_{\max} \approx \left(M - \frac{1}{2} \right) \pi . \tag{5.2}$$

Using Equation (5.2), $\phi_{\max}$ for the waveguides written with 30, 400, 800, 1200, 1800 and 2200nJ pulses is approximately 1.5π, 2.5π, 3.5π, 4.5π, 5.5π and 6.5π respectively.

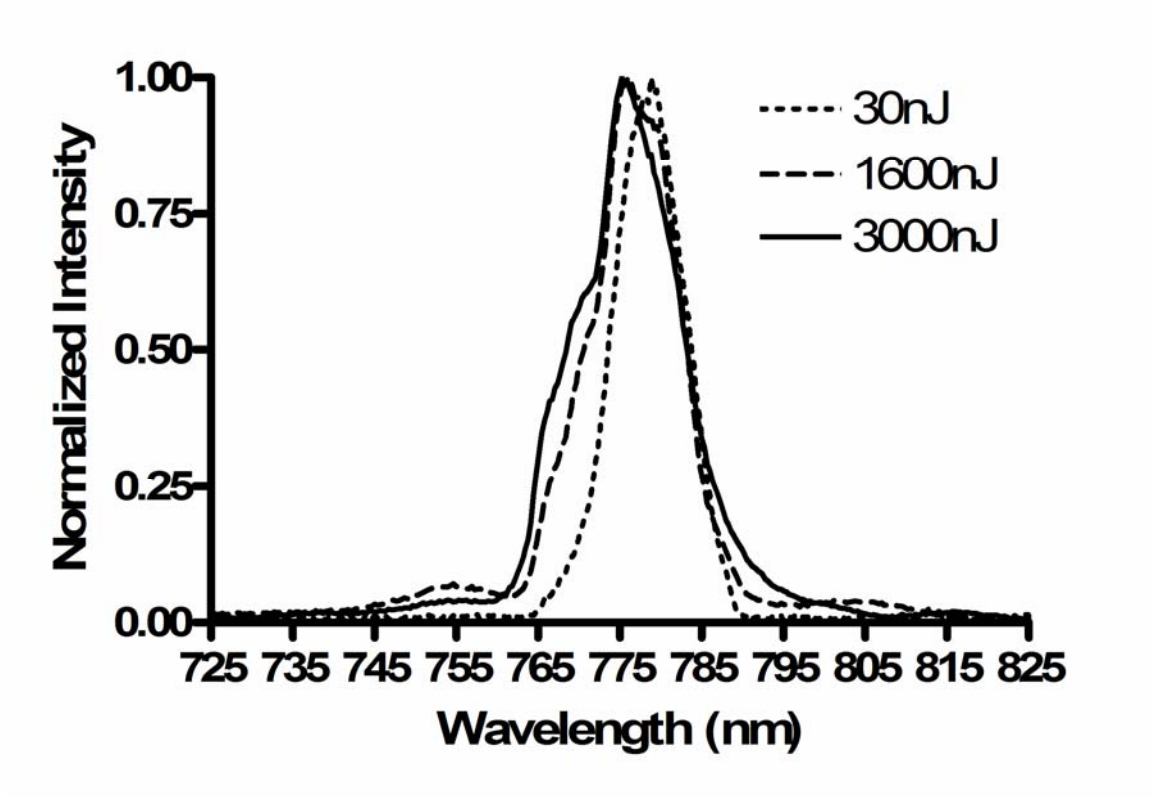

Figure 5-45. Output spectra for coupling to bulk HPFS.

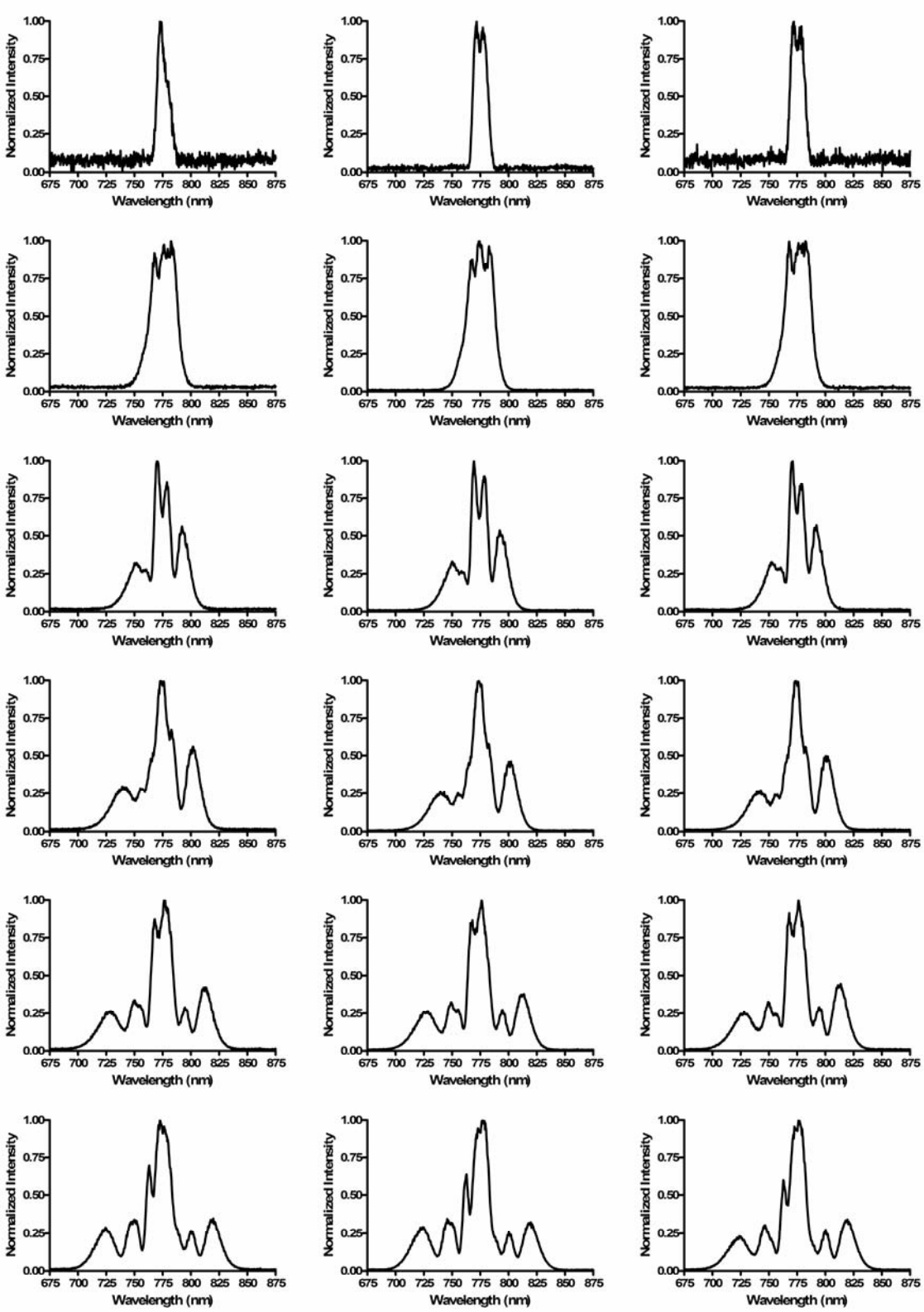

Figure 5-46. Output spectra for left: small, middle: medium and right: large core waveguides with input energies of 30, 400, 800, 1200, 1800 and 2200 nJ from top to bottom respectively.

The temporal dynamics as a function of input pulse energy were determined for the single-core waveguides over an input energy range from 125 nJ to 1500 nJ. Interferometric autocorrelations of the input pulses are shown in Figure 5-47. Before spatial filtering, the input pulse autocorrelation has the characteristic 8:1 peak:wing ratio. Spatially filtered pulses have a 6.5:1 ratio due to a slight misalignment in the autocorrelator. The FWHM pulse duration is estimated to be 100 fs, assuming a Gaussian pulse shape.

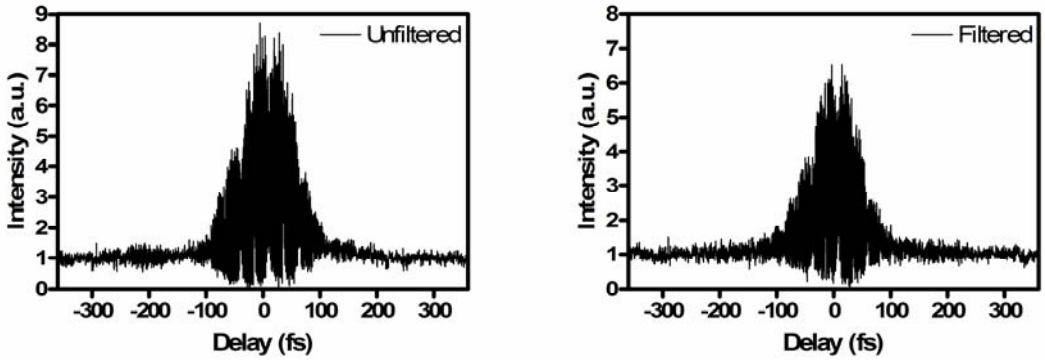

Figure 5-47. Interferometric autocorrelations of input beam without spatial filtering (left) and with spatial filtering (right)

Interferometric autocorrelations of the output pulses are plotted in Figure 5-48. In general, the autocorrelations are slightly asymmetric and have peak:wing ratios other than 8:1 due to minor alignment errors in the autocorrelator. Most notably, every autocorrelation over the entire range of energies recorded exhibited a broadened autocorrelation envelope and a narrowed interference pattern which is indicative of SPM-induced chirp. The envelope broadening was more significant than in the case of the solid-core PCF and increased with input pulse energy. Some of the more energetic input pulses have envelopes which extended over more than 700 fs in the wings.

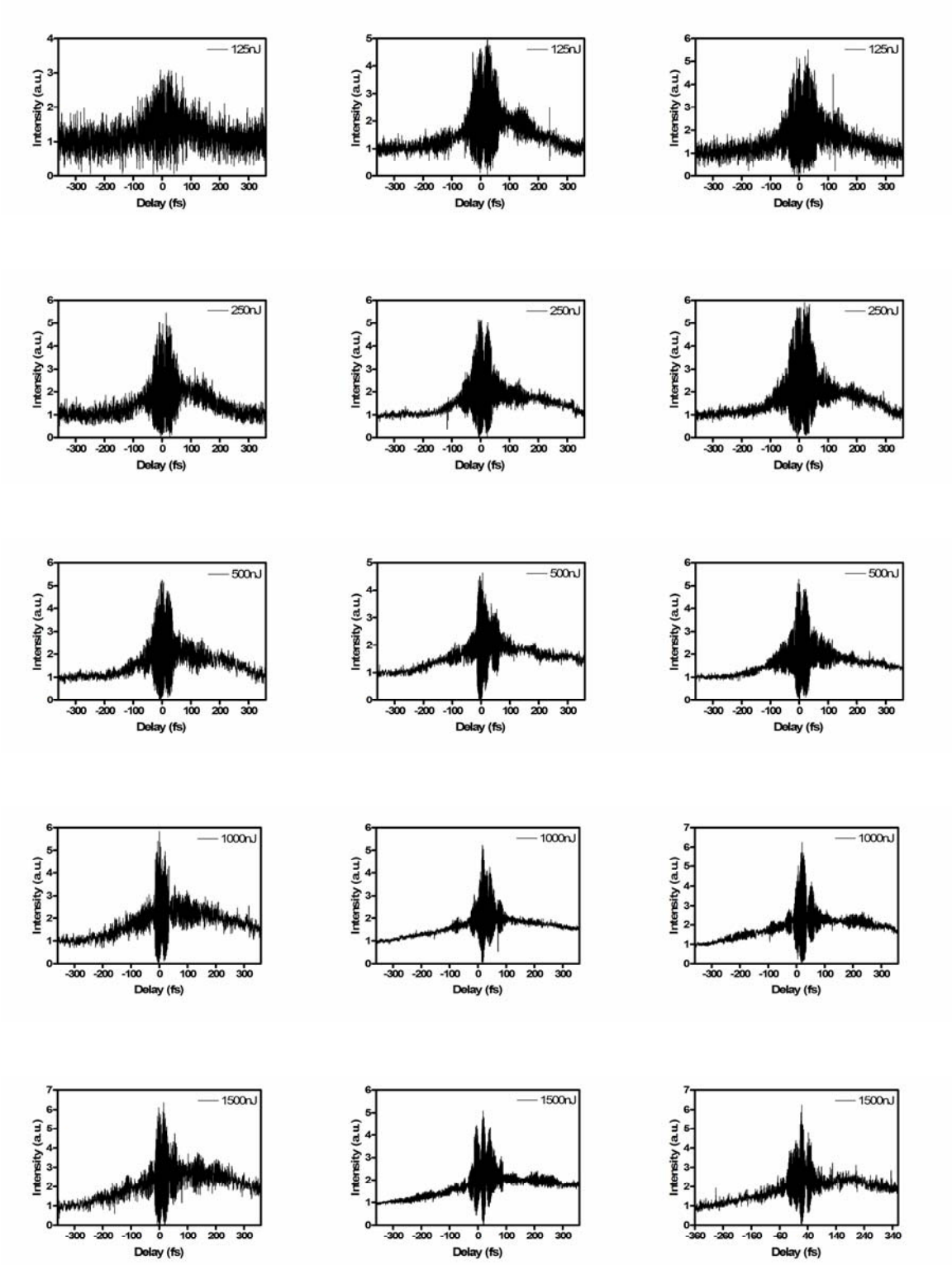

Figure 5-48. Interferometric autocorrelations of output from femtosecond-written single-core waveguides for given input pulse energies for 4.9 μm (left), 9.0 μm (middle) and 9.6 μm (right) core diameter waveguides

5.4.3.2 *Femtosecond Pulses in a 7-core Waveguide Array*

Three isometric 7-core arrays were written in 1 mm thick high-purity fused silica substrates with identical (9 μm) outer cores and either smaller (4.9 μm), equivalent (9 μm) or larger (9.6 μm) center cores. The outer cores were written with 1.15 μJ pulses, the smaller center core was written with 1.1 μJ pulses and the larger center core was written with 1.2 μJ pulses. All waveguides were written with a translation speed of 20 μm/s at a depth of 500 μm below the substrate surface using a focused astigmatic beam with Z_0 = 50 μm. The length of each array was 11 mm and the center-to-center waveguide spacing was 12 μm for each array.

The waveguide endfaces were polished and femtosecond pulses were endfire coupled into each of the arrays using the same experimental setup that was used in Section 4.1.2.1. The input beam was centered on the center core of each of the arrays and had a calculated diffraction limited waist diameter of 25 μm or roughly the array diameter. This provided excitation of all cores at the input, rather than the center core alone as was the case for the 3-core and 4-core arrays in Sections 5.4.2.1 and 5.4.2.2 respectively. By coupling to all cores simultaneously, preferential excitation of the in-phase, fundamental supermode can occur [36]. The near-field beam profiles, recorded at the output of each array for input pulse energies between 30 and 1000 nJ, are shown in Figure 5-49. For comparison, the fundamental supermodes, calculated from the SMM, are plotted in Figure 5-50. The experimental beam profiles are in good qualitative agreement with the theoretical profiles in that the power distributions are as predicted for the varying center core diameters and refractive indices.

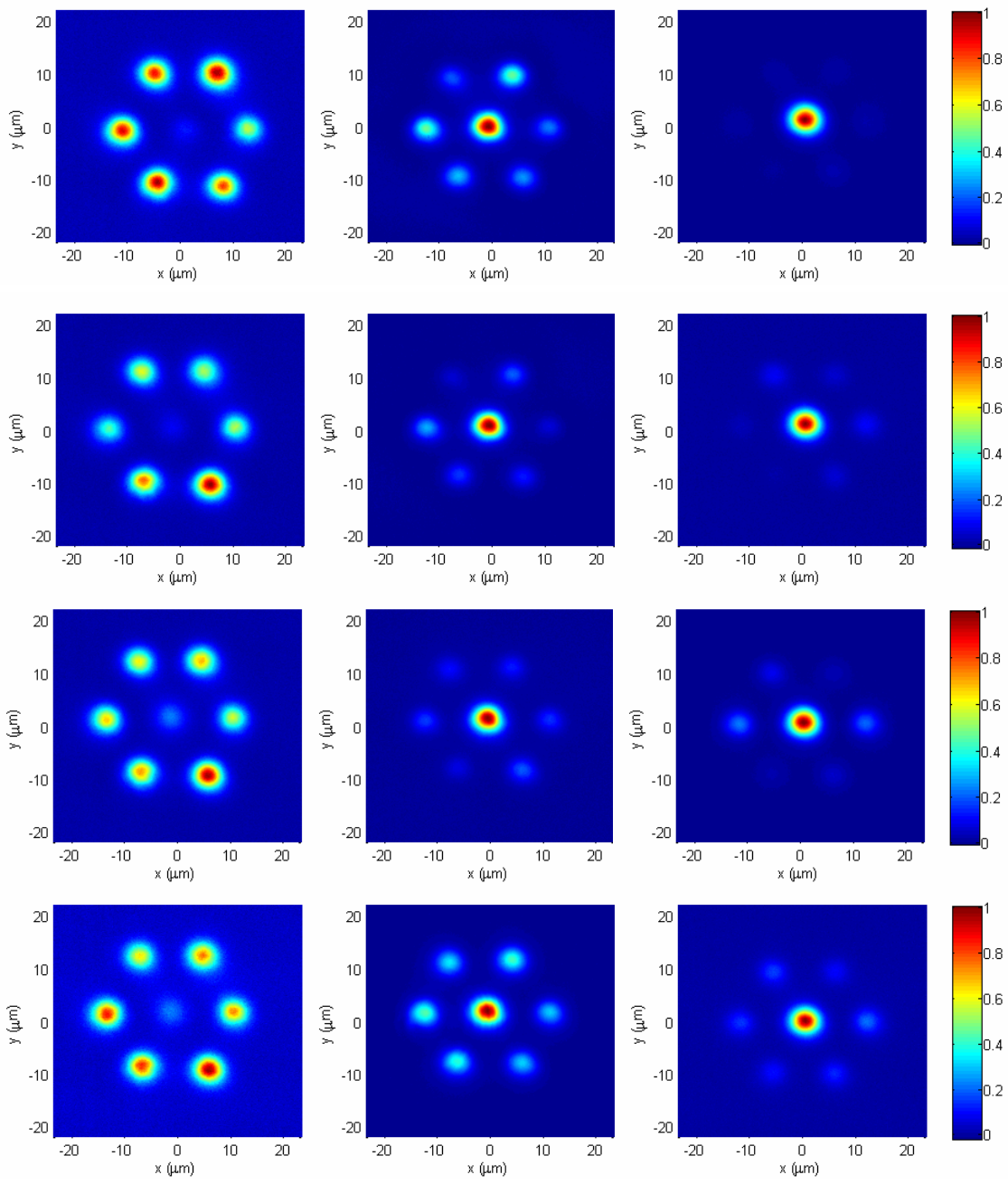

Figure 5-49. Output beam profiles for 7-core arrays with left: smaller center core, middle: all cores identical and right: larger center core with input pulse energies of 30, 200, 600 and 1000nJ from top to bottom respectively.

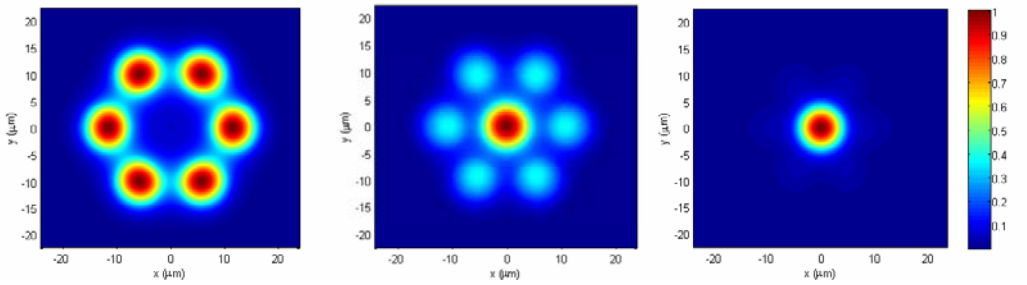

Figure 5-50. SMM simulated near-field output beam profiles of the fundamental supermode for the 7-core arrays. Left: smaller center core, Middle: all cores equivalent, Right: larger center core

The measured energy transmission through the three arrays as a function of input energy is plotted in Figure 5-51. The transmitted energy was linear over the range tested for each of the arrays, with the large center core array transmitting the most energy and the array with smaller center core transmitting the least. Since the same coupling conditions with the single waveguides resulted in similar transmission for all waveguides tested, the differences in transmission for the arrays are possibly due to variations in coupling efficiency to the array supermodes.

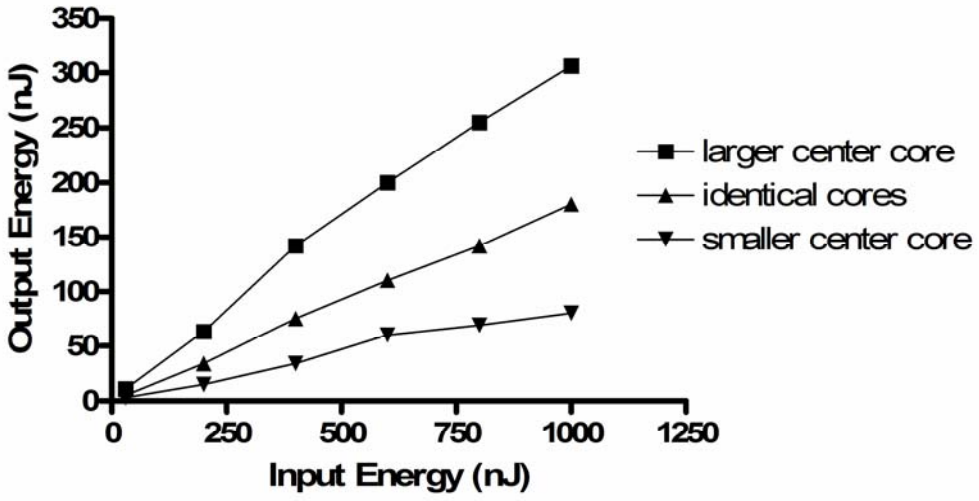

Figure 5-51. Transmission through femtosecond direct-written waveguide arrays

The output spectra for each of the 7-core waveguide arrays as a function of input energy are plotted in Figure 5-52. In general, the degree of SPM induced spectral broadening increases with input pulse energy as well as center core diameter and refractive index. This is as expected, since the amount of light confined to the center core in the fundamental supermode also increases with center core V-number. Since the array with the larger center core also transmitted the most power, it is reasonable to assume that it would also experience a higher nonlinearity than the other two cases. Compared to the single-core waveguides in Section 5.4.3.1, the 7-core array with larger center core had approximately three-fold higher transmission efficiency. For comparable delivered energy of 200 nJ, the spectra of both the single waveguide(s) and the 7-core array had roughly the same number of spectral peaks, though the depth of modulation was more pronounced for the single waveguide case. The broadening was also similar for both cases. The transmission efficiency for the 7-core array with all identical waveguides was less than a factor of two higher than the single waveguide case. However, for an output energy of 100 nJ, more spectral peaks were present than for single waveguides with the same output energy. This could be due to the difference in phase shifts experienced in the center core compared to the outer cores. The spectrum is essentially a summation of the spectral components and their associated phase from each of the individual waveguides in the array. Since the intensity in the center core is higher than it is in the outer cores, light propagating in it experiences a larger phase shift. Likewise, each of the outer cores is slightly different as is the intensity of the light propagating within them. Summing the SPM contributions from all cores of the array will yield a complex spectrum with multiple peaks that is sensitive to array defects. This effect is more

distinct for the all-cores-identical array because the outer cores have sufficient intensity to produce appreciable SPM. For the larger-center-core array, the outer waveguides had lower intensity and the power in the center core dominated the phase shift. The effect is also seen, to a lesser extent, in the array with smaller center core. For this case, the power is mainly in the outer cores and although the intensity in each of the outer cores varies, as observed in the profiles in Figure 5-49, the overall transmitted power is lower than the other two arrays as plotted in Figure 5-51, resulting in decreased SPM in each core.

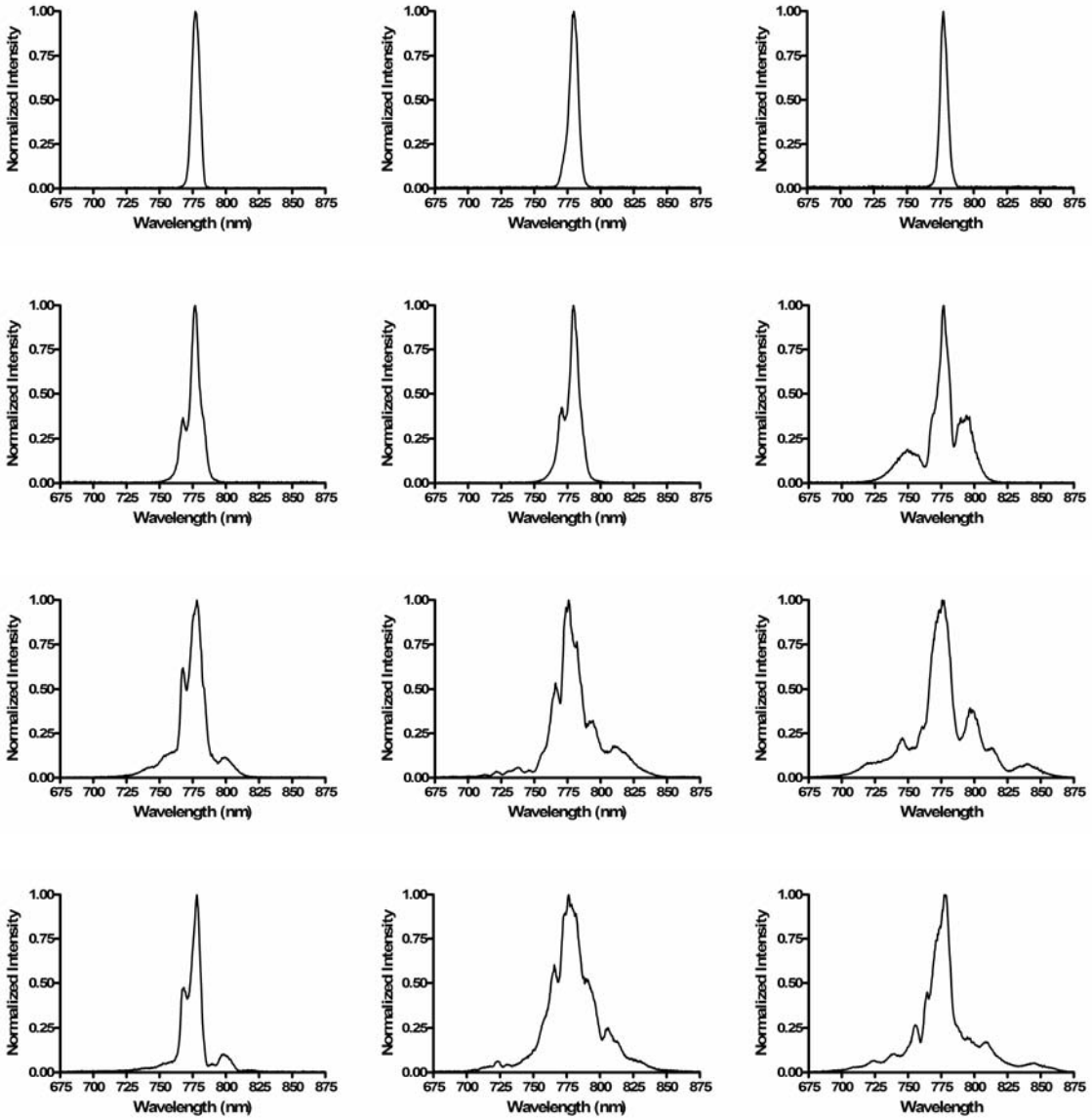

Figure 5-52. Output spectra for 7-core arrays with left: smaller center core, middle: all cores identical and right: larger center core with input energies of 30, 200, 600 and 1000nJ from top to bottom respectively.

5.4.3.3 ***Temporal Dynamics of 7-core Array***

The filtered pulses plotted in Figure 5-47 were used as input pulses for the 7-core arrays. In general, the temporal behavior as a function of input pulse energy was very similar to that of the single core waveguides. Interferometric autocorrelations of the array output pulses for input pulse energies from 125 nJ to 1500 nJ are plotted in Figure 5-53. Similar to the single-core waveguide autocorrelations, the array autocorrelations were slightly asymmetric and had peak:wing ratios other than 8:1 due to minor alignment errors in the autocorrelator. The autocorrelations also had broadened envelopes and narrowed interference patterns from SPM-induced chirp. The envelope broadening also increased with input pulse energy and extended over several hundred femtoseconds in the wings for the most energetic pulses.

5.4.3.4 ***Output Diffraction from 7-core Array***

In order to characterize the diffraction properties of the output from an array, beam profiles were taken at 50 μm increments away from the array end-face up to a distance of 500 μm for the 7-core array with smaller center core. The results were compared to a theoretical model using Fraunhofer's diffraction theory assuming all emitters had equal amplitude coefficients. The results are plotted in Figure 5-54. Asymmetry in the experimental profiles results from unequal power distribution among the cores at the output of the array. However, reasonable qualitative agreement is found between theory and experiment with the output forming an on-axis, high-intensity lobe in the far field.

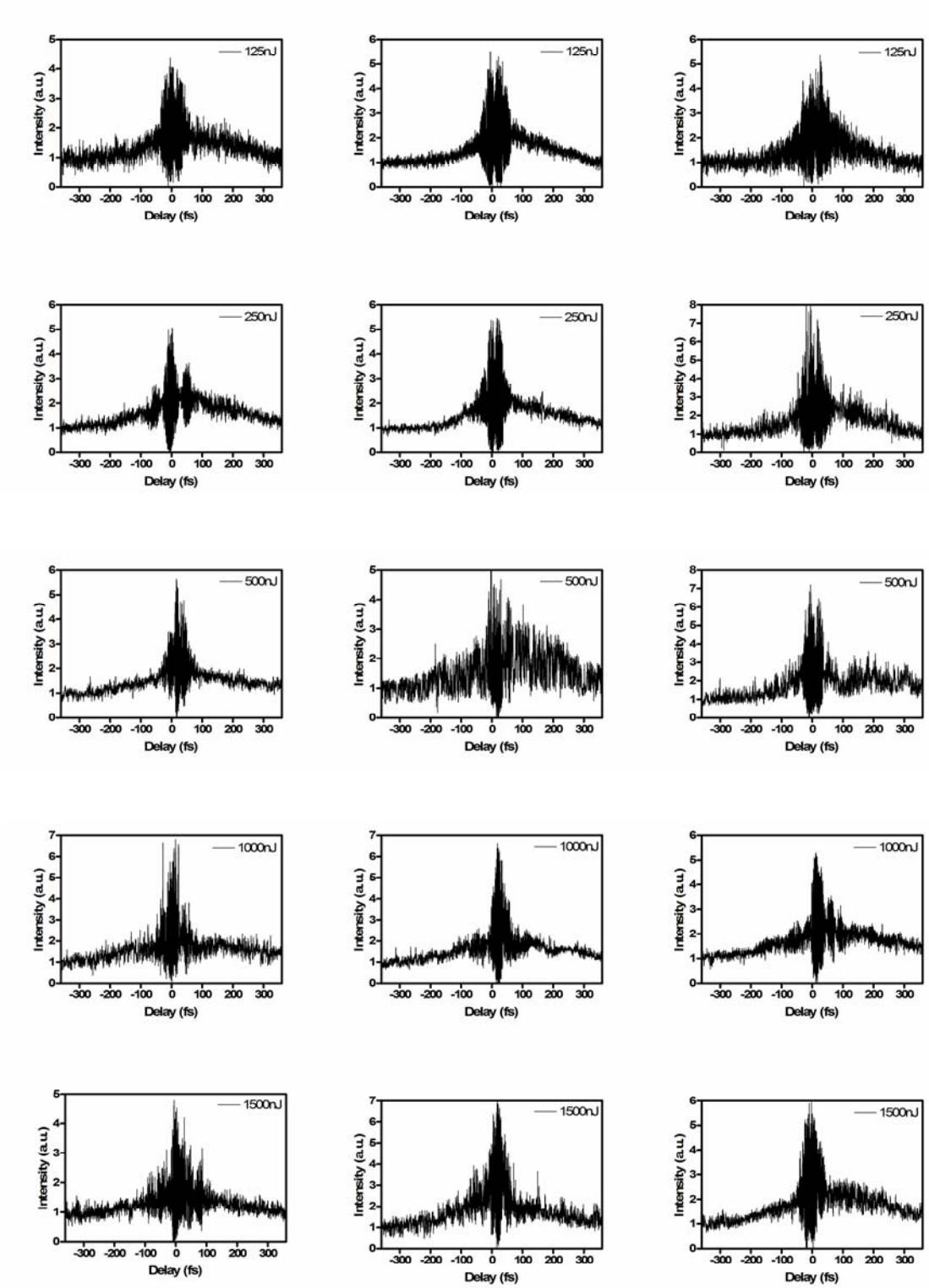

Figure 5-53. Interferometric autocorrelations of output from femtosecond-written 7-core waveguide arrays for given input pulse energies for smaller (left), identical (middle) and larger (right) center core diameters

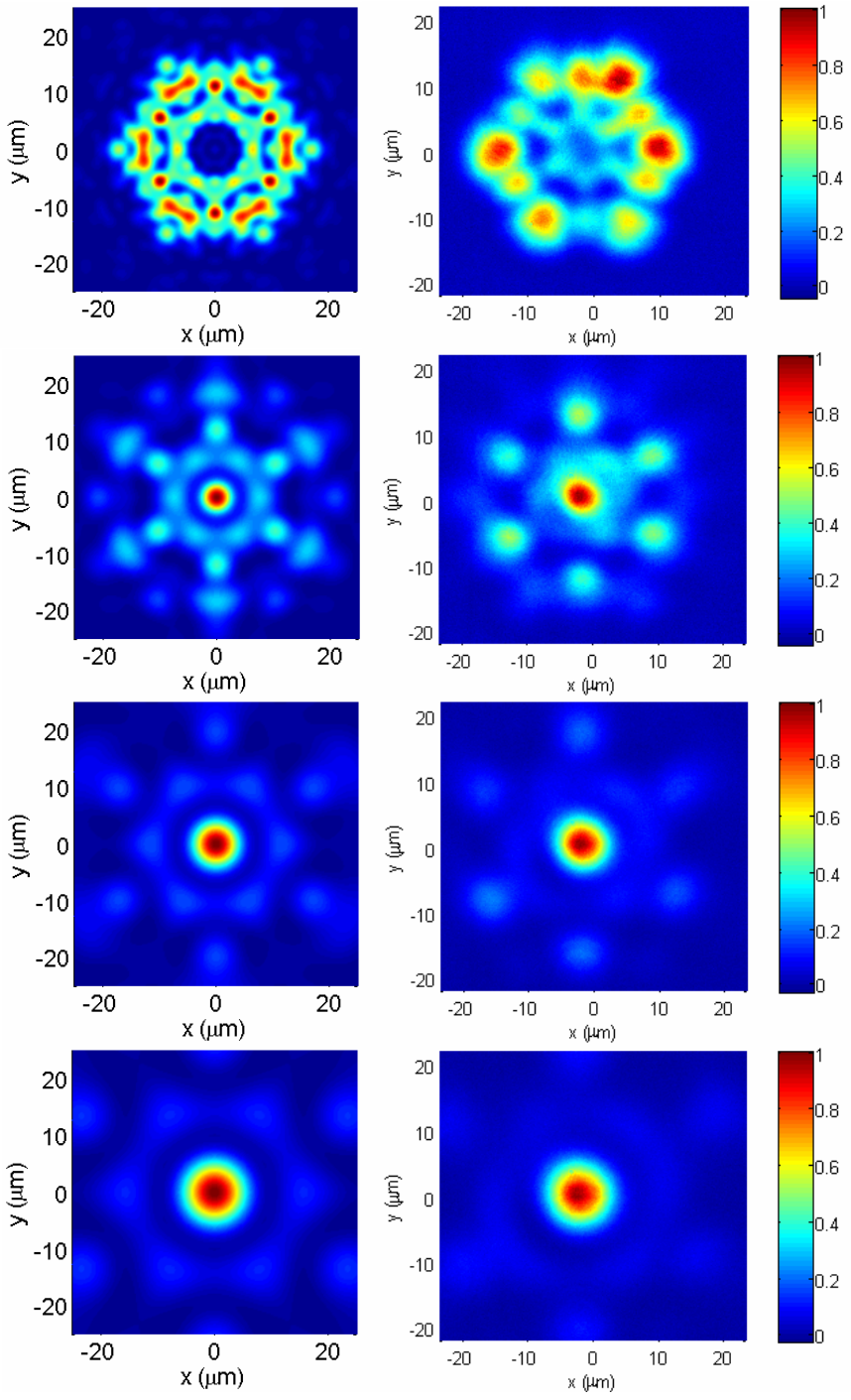

Figure 5-54. Theoretical (left) and experimental (right) diffraction patterns for the 7-core array with smaller center core at 100, 200, 300 and 400 μm away (from top to bottom respectively) from the array end face.

5.5 Conclusions

Circular, symmetric, single-mode waveguides were successfully written in soda-lime and fused silica glass substrates using the femtosecond direct-write technique. The soda-lime glass waveguides exhibited strong fluorescent color-center formation that increased as a function of writing pulse energy as determined through laser scanning confocal microscopy. Three-core and 7-core arrays with tailored supermodes were written in soda-lime glass. Output beam profiles of the 3-core arrays were in good qualitative agreement with SMM calculated profiles. The individual waveguides of the 7-core arrays in soda-lime glass were found to support the higher order LP_{11} mode due to a change in the writing conditions and were not useful for examining supermode tailoring. However, the far-field diffraction properties of short 7-core arrays were found to be in good agreement with theory.

Single femtosecond direct-written waveguides in fused silica were characterized to determine their numerical aperture, refractive index change, loss, and relative diameters as a function of writing pulse energy. Writing conditions which produced three different sizes of single-mode waveguides were then used to write arrays of 3-, 4- and 7-cores for evaluation of supermode tailoring. Evanescent coupling was verified in the 3-core array and was found to be in good agreement with a coupled mode analysis model. Propagation of femtosecond pulses was tested in the three single waveguides as well as in three 7-core arrays with different center cores. Beam profiles of the array outputs were in good qualitative agreement with SMM simulations of the fundamental supermode. Nonlinear and dispersive effects had appreciable consequences on the temporal dynamics of both the single waveguides and the 7-core arrays when guiding femtosecond pulses.

Spectral broadening was more symmetric for the single waveguides and the arrays generally had more spectral peaks as a result of unequal phase shifts in the individual cores of the array. The transmission was nearly the same for all three single waveguides, whereas the array transmission increased with increasing center core diameter and refractive index.

6 Summary and Applications

6.1 Summary of USP Delivery in Specialty Fibers

Four distinctly different types of specialty fibers and waveguides were evaluated in this dissertation: solid-core photonic crystal fiber, hollow-core photonic crystal fiber, hollow silica waveguide and waveguide arrays. The performance and limitations of each for delivery of high-peak-power ultrashort pulses were determined by recording output beam profiles, transmission, output spectra and output autocorrelations as a function of input pulse energy.

Solid-core photonic crystal fiber was evaluated in Section 4.1. Properties of the tested fiber which made it a good candidate for USP delivery included a large mode area, 23 μm diameter core and endlessly single-mode guidance due to its as-designed hole-to-pitch ratio of 0.29. A 710 mm long section of the fiber was capable of delivering up to 2.6 nJ output pulses with an undistorted spectra. As the output pulse energy was increased above 2.6 nJ, SPM caused broadening and multiple peak formation in the output spectrum. Interferometric autocorrelations of the output pulses had a narrowed interference region due to SPM-induced chirp and side-lobes appeared due to spectral structure. The maximum delivered energy was found to be limited by self-focusing-

induced damage. Above a peak delivered energy of 190 nJ the fiber was damaged by subsequent increases in input power.

Hollow-core photonic crystal fiber was evaluated in Section 4.2. In addition to having a large mode area, 27 μm diameter core, the HC-PCF guides primarily in air, reducing the effective nonlinear coefficient by several hundred times compared to solid-core fibers. A 60 mm long section of HC-PCF was shown to be an excellent candidate for delivery of μJ-level USPs with minimal spectral distortion due to SPM. Interferometric autocorrelations of the output confirmed that the temporal pulse duration was also conserved. A maximum pulse energy of 8 μJ was delivered (peak power of 73 MW), limited only by the energy available in the experimental setup. The output also had a high-quality, Gaussian single-mode profile.

Hollow silica waveguides were evaluated in Section 4.3. Similar to the HC-PCF, the HSW also guides primarily in air and therefore has a much lower nonlinear coefficient than silica. Four different waveguide bore diameters were tested: 300, 500, 750 and 1000 μm. Propagation of high energy USPs with minimal temporal, spectral and spatial distortion was demonstrated in all four waveguide sizes at distances up to a meter, when the waveguides were kept straight with preferential fundamental (HE_{11}) mode coupling. A maximum of 700 μJ (4 GW) was delivered through a straight, 0.92 m long 750 μm bore diameter waveguide. Bending the waveguides resulted in high-order mode excitation and increased inter-modal dispersion. Output beam profiles of bent waveguides had multiple peaks due to higher-order mode propagation. It was confirmed that temporal dispersion in the waveguides is proportional to the waveguide bore

diameter due to increased higher-order mode loss (and less inter-modal dispersion) as the bore diameter decreases.

Common-core waveguide arrays with tailored supermodes were numerically evaluated in Chapter 3 and experimentally evaluated in Chapter 5. Based on numerical results, it was predicted that the power distribution could be controlled in these arrays by changing the V-number of the center core. Proper selection of the center core V-number could therefore provide uniform power distribution among all cores of the array for the fundamental supermode, thereby reducing intensity in the array and nonlinear effects. In order to test the model, waveguide arrays with 3-, 4- and 7-cores were directly written in either soda-lime glass or high-purity fused silica using femtosecond pulses. Writing conditions were determined to produce symmetric, circular cylindrical waveguides that were also single mode for writing the arrays. Evanescent coupling was confirmed for a 3-core array in HPFS in Section 5.4.2.1 and was in good agreement with theory. Power distribution control was demonstrated for all arrays by varying the writing conditions (and V-number) of the center core. Ultrashort pulses were endfire coupled to 7-core arrays and their performance was compared to single direct-written waveguides. Array transmission increased with increasing center core diameter, likely due to higher coupling efficiency for larger center cores. Array output spectra were broadened with increasing input energy with the formation of multiple peaks, however the modulation was not as deep as for single waveguides. It was suggested that, due to slight differences in the individual waveguide intensities which could be caused by asymmetric coupling, higher-order supermode propagation and/or manufacturing variances, each waveguide in the array experiences a slightly different phase shift, resulting in the formation of more peaks

but reduced modulation depth. Temporal dynamics of the arrays were very similar to the single waveguides with a narrowed interference region in the interferometric autocorrelations combined with a broadened pedestal which is associated with SPM-induced chirp.

The properties of the specialty fibers and waveguides tested in this dissertation are summarized in Table 6-1. Properties for conventional single-mode fiber (SMF) are also listed for comparison.

Table 6-1. Properties of evaluated specialty fibers.

Fiber/Waveguide	SMF	PCF	7-core Array	HC-PCF	HSW-300	HSW-500	HSW-750	HSW-1000
Core Diameter (μm)	5	23	9 (outer), 9.6 (center)	27	300	500	750	1000
Core Area (μm^2)	20	415	454	573	70686	196349	441786	785398
Length (mm)	-	710	11	60	1000	500	920	980
Core Material	Fused Silica	Fused Silica	Fused Silica	Air	Air	Air	Air	Air
Cladding Material	Fused Silica	Fused Silica/Air Holes	Fused Silica	Fused Silica/Air Holes	Ag/AgI	Ag/AgI	Ag/AgI	Ag/AgI
Nonlinear coefficient (cm^2/W)	3×10^{-16}	3×10^{-16}	3×10^{-16}	$< 3 \times n_{2,air}$ # †	$\approx n_{2,air}$ †	$\approx n_{2,air}$ †	$\approx n_{2,air}$ †	$\approx n_{2,air}$ †
Loss (straight)	≈ 4db/km	< 10 dB/km *	0.45 dB/cm	> 1 dB/km ‡	2 dB/m	0.6 dB/m	0.5 dB/m	0.4 dB/m
Peak Power for Undistorted Pulse	200 W Δ	19 kW	80 kW	23.6 MW	3.1 GW	4.6 GW	4.1 GW	4 GW
Damage Threshold (straight)	-	1.7 MW	1.2 MW	> 23.6 MW	> 3.1 GW	> 4.6 GW	> 4.1 GW	> 4 GW
Guiding Mechanism	TIR	Modified TIR	TIR	Low Density of States	Grazing Incidence	Grazing Incidence	Grazing Incidence	Grazing Incidence
Modes Supported	1	1	14 (for ideal array)	Few	100's	100's	100's	100's
Modes Excited	-	1	1	1	2	4	13	35
Modes Excited, Bent	-	1	n/a	n/a	n/a	6	19	> 50

* Crystal Fiber A/S Specs.
\# From reference [62]
† $n_{2,air} = 3 \times 10^{-19}$ cm^2/W
‡ From reference [61]
Δ From reference [5]

6.2 Applications

6.2.1 Tissue Ablation with Guided Femtosecond Pulses

In recent years, research involving the use of ultrashort pulses for the ablation of various hard and soft biological tissues has shown improvement compared to ablation with pulses of longer duration. Since the ablation threshold is lower for ultrashort pulses, tissue may be vaporized with relatively low energy pulses and therefore less energy is available to the ensuing shock wave in the tissue, thereby reducing the extent of collateral damage.

Thermal damage is restricted to the optical penetration depth of the tissue since the duration of the pulse is much shorter than the thermal diffusion time. Ultrashort pulse ablation is especially ideal for transparent and low absorbing materials, due to the process of nonlinear absorption.

A mechanism for the delivery of ultrashort pulses *in vivo* would provide the means to use plasma-mediated ablation in minimally invasive surgical (MIS) procedures. Due to their demonstrated performance in delivering high-power ultrashort pulses with minimal distortion, hollow silica waveguides were chosen as a beam delivery mechanism for tissue ablation studies. In order to increase the fluence on the tissue, focusing of the output was also tested using Fresnel lenses as a way to minimize nonlinear pulse distortions that could occur in relatively thick refractive lenses.

6.2.2 Diffractive Optic Focusing of HSW Output

Although the fluence at the output of the hollow waveguide is sufficient to ablate tissues, the removal rate can be further increased by focusing. Additionally, MIS procedures would require that the hollow waveguide is sealed on the distal end to prevent waveguide contamination and to maintain waveguiding. Typical refractive lenses are thick and bulky and can adversely affect the high-intensity output pulses through nonlinear effects and can also become damaged through self-focusing. An alternative is to use a Fresnel lens that focuses by diffraction. Fresnel lenses can be made thin (1 mm or less) to stave off nonlinear effects and self-focusing and can also act as a window to seal the waveguide.

The output from a 1 m long, 300 μm bore diameter was focused using an eight phase level diffractive Fresnel lens on a 1 mm thick fused silica substrate (Figure 6-1) fabricated at The University of Central Florida, CREOL. The lens diameter was 2 mm and the focal length was approximately 11 mm. The lens was placed in a threaded end cap and attached to the waveguide end using an SMA connector. The focused spot diameter was estimated from beam profile measurements to be approximately 100 μm when used with a straight 300 μm waveguide.

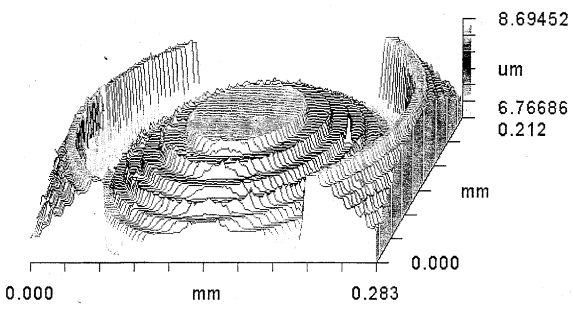

Figure 6-1. Eight-phase level diffractive Fresnel lens used to focus the output from a 300μm bore diameter hollow waveguide

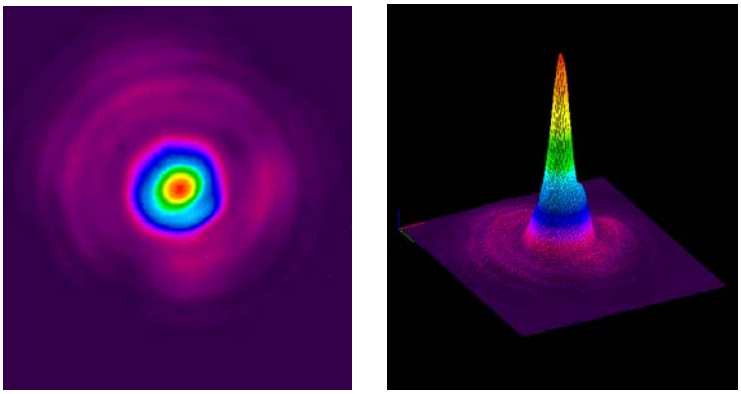

Figure 6-2. Fresnel lens focused beam from 300 μm bore diameter hollow waveguide

6.2.3 **Ablation of Porcine Tissues**

Fresh cadaveric porcine liver and heart tissues were obtained from a local abattoir and kept at 4ºC until laser targeted. The tissues were affixed to a motorized *x-y-z* translational stage and translated at 1 mm/s with respect to the waveguide end for ablation studies. The output of the 300 μm waveguide was focused onto the tissue using the diffractive lens above. Following ablation, the tissues were processed for histological examination by light microscopy (LM) and scanning electron microscopy (SEM). Samples for LM were 4μm thick paraffin embedded sections processed and stained with hematoxylin and eosin. Samples for SEM were prepared with modified Karnovsky's fixative, and then dehydrated, critical point dried, and sputter coated with approximately 600 Å of Au/Pd.

Scanning electron and light micrographs of the ablated porcine liver and cardiac muscle samples are shown in Figure 6-3 and Figure 6-4 respectively. The peak power transmission through the 300 μm waveguide and lens combination was 1.4 GW, with delivered pulse energy of 205 μJ. Given a focused spot diameter 100μm, this gives a fluence of 2.6 J/cm^2 on the tissue. The extent of cellular damage in the liver is seen as an increase in eosinophilic intensity. The ablation in the cardiac muscle extends well below the epicardium to a depth of approximately 275 μm. Compared to free-space ultrashort pulse ablation at similar fluences [92, 93], these results are very similar in terms of collateral damage and material removal and depth of cut.

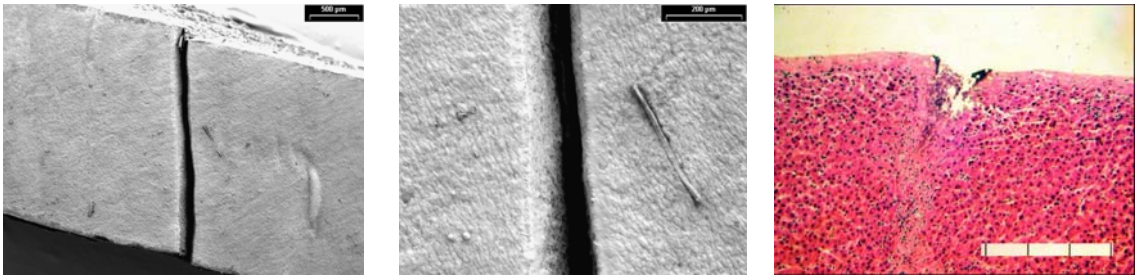

Figure 6-3. Porcine liver tissue ablated with output from 300 µm hollow waveguide - left, middle: SEM, right: LM (vertical bar spacing = 100 µm)

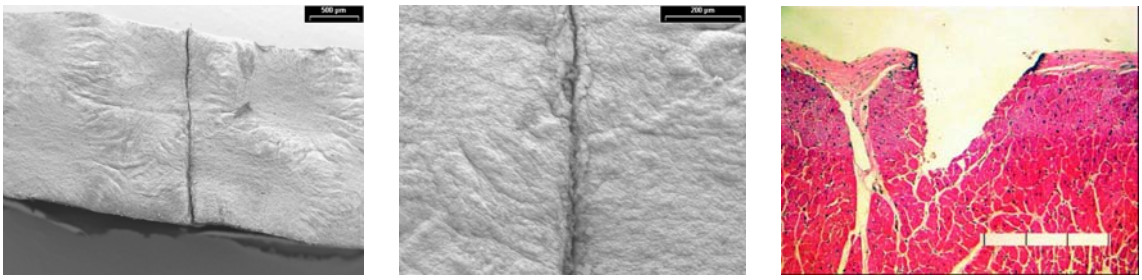

Figure 6-4. Porcine heart tissue ablated with output from 300 µm hollow waveguide. SEM (left and middle), LM (right) The vertical bar spacing is 100 µm.

6.2.4 **Conclusions**

The output from the 300µm waveguide was focused using a diffractive Fresnel lens and used to ablate fresh cadaveric porcine liver and heart tissues. Light and scanning electron microscopy of the tissues show minimal collateral damage and thermal effects, consistent with the results of ablation with free-space ultrashort pulses. It was shown that hollow waveguides can be used as a delivery mechanism of ultrashort pulses for tissue ablation and that sufficient energy is delivered for other machining applications.

6.3 Future Directions

This research has touched on a broad range of specialty fibers and waveguides. As the technologies and/or their uses as USP delivery mechanisms are relatively new, much work remains to be done in order to fully characterize and optimize their performance.

Output pulses from specialty fibers and waveguides were analyzed using a separate interferometric autocorrelator and spectrometer to determine the temporal pulse dynamics and spectra respectively as a function of pulse energy. While this data provided valuable information as to the behavior of the pulses as they propagated in these fibers and waveguides, it was not a complete characterization of the output pulses. Frequency resolved optical gating (FROG) is now widely accepted as being able to fully characterize ultrashort pulses in terms of not only their temporal and spectral intensities, but also the temporal and spectral phase. FROG would be especially useful in characterizing the complex output pulses from the solid-core PCF and femtosecond direct-written waveguide arrays and could offer more insight to their analysis.

The solid- and hollow-core photonic crystal fibers in this work were obtained more than five years ago. Since that time, manufacturing tolerances have improved, the commercially available selection of fibers has increased and the cost is now much lower. Given the demonstrated performance of the hollow-core photonic crystal fiber, it is of interest to evaluate longer lengths for consideration in real-world applications. The periodic defects that were present in longer lengths of the HC-PCF in this work may no longer be an issue with current fibers.

The hollow silica waveguides in this work were not optimized for delivery in the near-infrared. Although they did contain thin-film silver coatings to increase their

transmission upon bending compared to uncoated silica capillaries, the dielectric layer thickness was optimized for delivery of infrared light at 2.9 μm. While this had little effect on the transmission of straight fibers, bending losses are expected to improve with an optimized dielectric layer.

Femtosecond direct-writing of waveguides and waveguide arrays provides a tremendous amount of freedom when designing and fabricating practical devices. The array geometries considered in this work for tailoring array supermodes represent a possible solution for arrays with seven or fewer cores. However, the modeling and fabrication principles developed could be applied to much larger arrays comprising tens or even hundreds of cores with arbitrary refractive index, spacing and placement.

References

1. McClung, F.J. and R.W. Hellwarth, *Giant Optical Pulsations from Ruby.* Journal of Applied Physics, 1962. **33**(3): p. 828-829.

2. Migus, A., et al., *Amplification of subpicosecond optical pulses: theory and experiment.* IEEE Journal of Quantum Electronics, 1982. **QE-18**(101).

3. Shank, C.V. and E.P. Ippen, *Subpicosecond kilowatt pulses from a modelocked cw dye laser.* Applied Physics Letters, 1974. **24**: p. 373-375.

4. Morgner, U., et al., *Sub-two-cycle pulses from a Kerr-lens mode-locked Ti:sapphire laser.* Opt. Lett., 1999. **24**(6): p. 411-413.

5. Clark, S.W., F.O. Ilday, and F.W. Wise, *Fiber delivery of femtosecond pulses from a Ti:sapphire laser.* Optics Letters, 2001. **26**(17): p. 1320-1322.

6. Knight, J.C., et al., *All-silica single-mode optical fiber with photonic crystal cladding.* Optics Letters, 1996. **21**(19): p. 1547-1549.

7. Miyagi, M. and S. Kawakami, *Design Theory of Dielectric-Coated Circular Metallic Waveguides for Infrared Transmission.* IEEE Journal of Lightwave Technology, 1984. **LT-2**: p. 116-126.

8. Matsuura, Y., et al., *Hollow fibers for delivery of harmonic pulses of Q-switched Nd:YAG lasers.* Applied Optics, 2002. **41**(3): p. 445.

9. Matsuura, Y. and M. Miyagi, *Flexible hollow waveguides for delivery of excimer laser light.* Optics Letters, 1998. **23**(15): p. 1226.

10. Matsuura, Y., et al., *Delivery of femtosecond pulses by flexible hollow fibers.* Journal of Applied Physics, 2002. **91**(2): p. 887.

11. Glas, P., et al., *The multicore fiber – a novel design for a diode pumped fiber laser.* Optics Communications, 1998. **151**: p. 187-195.

12. Davis, K.M., et al., *Writing waveguides in glass with a femtosecond laser.* Optics Letters, 1996. **21**(21): p. 1729-1731.

13. Nguyen, M. and K. Church, *Tailoring Modal Power Distribution in Common-Core Waveguide Arrays.* Journal of Lightwave Technology, 2006. **24**(6): p. 2434-2441.

14. Nguyen, M. and K. Church. *Femtosecond Laser Written Waveguide Arrays with Tailored Supermodes*. in *Conference on Lasers and Electro-Optics*. 2007. Baltimore, MD.

15. Nguyen, M., et al. *Hollow waveguide delivery of ultrashort pulses for tissue ablation*. in *Optical Fibers and Sensors for Med Appl IV*. 2004. San Jose, CA: SPIE.

16. Ben-David, M., et al., *Pulse dispersion in hollow optical waveguides.* Optical Engineering, 2005. **44**(9): p. 095001 1-6.

17. Ashcom, J.B., et al., *Numerical aperture dependence of damage and supercontinuum generation from femtosecond laser pulses in bulk fused silica.* J. Opt. Soc. Am. B, 2006. **23**(11): p. 2317-2322.

18. Agrawal, G.P., *Nonlinear Fiber Optics 3rd Edition*. 1995: Academic Press.

19. Buck, J.A., *Fundamentals of Optical Fibers*. 1995: Wiley-Interscience.

20. Agrawal, G.P., *Fiber-Optic Communication Systems*. 1997: Wiley-Interscience.

21. Boyd, R.W., *Nonlinear Optics*. 1992: Academic Press.

22. Fermann, M.E., A. Galvanauskas, and G. Sucha, *Ultrafast Lasers Technology and Applications*. 2001: Marcel-Dekker.

23. Stuart, B.C., et al., *Nanosecond-to-femtosecond laser-induced breakdown in dielectrics.* Physical Review B, 1996. **53**(4): p. 1749.

24. Perry, M.D., et al., *Ultrashort-pulse laser machining of dielectric materials.* Journal of Applied Physics, 1999. **85**(9): p. 6803.

25. Chichkov, B.N., et al., *Femtosecond, picosecond, and nanosecond laser ablation of solids.* Appl. Phys. A, 1996. **63**: p. 109.

26. Dickinson, J.T., et al., *Color center formation in soda lime glass and NaCl single crystals with femtosecond laser pulses.* Applied Physics A, 2004. **79**: p. 859-864.

27. Miura, K., et al., *Photowritten optical waveguides in various glasses with ultrashort pulse laser.* Applied Physics Letters, 1997. **71**(23): p. 3329-3331.

28. Will, M., et al., *Optical properties of waveguides fabricated in fused silica by femtosecond laser pulses.* Applied Optics, 2002. **41**(21): p. 4360-4364.

29. Streltsov, A.M. and N.F. Borrelli, *Study of femtosecond-laser-written waveguides in glasses.* J. Opt. Soc. Am. B, 2002. **19**(10): p. 2496-2504.

30. Chan, J.W., et al., *Structural changes in fused silica after exposure to focused femtosecond laser pulses.* Optics Letters, 2001. **26**(21): p. 1726-1728.

31. Streltsov, A.M., C.W. Ponader, and J.F.S. III. *Refractive-Index Increase in Laser-Written Waveguides in Glasses*. in *High-Power Laser Ablation VI*. 2006: Proc. of SPIE.

32. Streltsov, A.M. and N.F. Borrelli, *Study of femtosecond-laser-written waveguides in glasses.* J. Opt. Soc. Am. B/, 2002. **19**(10): p. 2496-2504.

33. Glezer, E.N. and E. Mazura, *Ultrafast-laser driven micro-explosions in transparent materials.* Applied Physics Letters, 1997. **71**(7): p. 882-884.

34. Huang, W.P., *Coupled mode theory for optical waveguides: an overview.* J. Opt. Soc. Am. A, 1994. **11**(3): p. 963-983.

35. Bochove, E.J., P.K. Cheo, and G.G. King, *Self-organization in a multicore fiber laser array.* Optics Letters, 2003. **28**(14): p. 1200-1202.

36. Huo, Y., P.K. Cheo, and G.G. King, *Fundamental mode operation of a 19-core phaselocked Yb-doped fiber amplifier.* Optics Express, 2004. **12**(25): p. 6230-6239.

37. Yamashita, E., Y. Nishino, and K. Atsuki, *Analysis of multiple dielectric waveguide systems with extended point-matching method.* IEEE MTT-S Digest, 1983: p. 119-121.

38. Goell, J.E., *A circular-harmonic computer analysis if rectangular dielectric waveguides.* Bell Syst. Tech. J. , 1969. **48**: p. 2133-2160.

39. Wijngaard, W., *Guided normal modes of two parallel circular dielectric rods.* J. Opt. Soc. Am., 1973. **63**(8): p. 944-950.

40. Huang, H.S. and H.C. Chang, *Analysis of equilateral three-core fibers by circular harmonics expansion method.* Journal of Lightwave Technology, 1990. **8**(6): p. 945-952.

41. Lo, K.M., et al., *An electromagnetic theory of dielectric waveguides with multiple embedded cylinders.* Journal of Lightwave Technology, 1994. **12**(3): p. 396-410.

42. Felbacq, D., G. Tayeb, and D. Maystre, *Scattering by a random set of parallel cylinders.* J. Opt. Soc. Am. A, 1994. **11**(9): p. 2526-2538.

43. White, T.P., et al., *Multipole method for microstructured optical fibers. I. Formulation.* J. Opt. Soc. Am. B, 2002. **19**(10): p. 2322-2330.

44. Roberts, P.J. and T.J. Shepard, *The guidance properties of multi-core photonic crystal fibres.* J. Opt. A: Pure Appl. Opt., 2001. **3**: p. 133-140.

45. Mohammed, W.S., L. Vassie, and E.G. Johnson, *Hybrid mode calculations for novel photonic crystal fibers.* Optical Engineering, 2003. **42**(8): p. 2311-2317.

46. Tayeb, G. and D. Maystre, *Rigorous theoretical study of finite-size two-dimensional photonic crystals doped by microcavities.* J. Opt. Soc. Am. A, 1997. **14**(12): p. 3323-3332.

47. Kishi, N., E. Yamashita, and K. Atsuki, *Modal and Coupling Field Analysis of Optical Fibers with Circularly Distributed Multiple Cores and a Central Core.* Journal of Lightwave Technology, 1986. **LT-4**(8): p. 991-996.

48. McIsaac, P.R., *Symmetry-induced modal characteristics of uniform waveguides – I: summary of results.* IEEE Trans. Microwave Theory Tech., 1975. **MTT-23**(5): p. 421-429.

49. Broderick, N.G.R., et al., *Nonlinearity in holey optical fibers: measurement and future opportunities.* Optics Letters, 1999. **24**(20): p. 1395.

50. Birks, T.A., J.C. Knight, and P.S.J. Russell, *Endlessly single-mode photonic crystal fiber.* Optics Letters, 1997. **22**(13): p. 961.

51. Knight, J.C., et al., *Anomolous dispersion in photonic crystal fiber.* IEEE Phot. Tech. Lett., 2000. **12**(7): p. 807.

52. Knight, J.C., et al., *Large mode area photonic crystal fiber.* Electronics Letters, 1998. **34**(13): p. 1347.

53. Zeek, E., et al. *Measurement of the autocorrelation factor for common pulses*. in *Lasers and Electro-Optics, 1999. CLEO '99. Summaries of Papers Presented at the Conference on*. 1999.

54. Ouzounov, D.G., et al., *Delivery of nanojoule femtosecond pulses through large-core microstructured fibers.* Optics Letters, 2002. **27**(17): p. 1513.

55. Andy Chong, J.B., Will Renninger, Frank Wise, *All-normal-dispersion femtosecond fiber laser.* Optics Express, 2006. **14**(21): p. 10095-10100.

56. Marburrger, J. and W. Wagner, *Self-focusing as a pulse sharpening mechanism.* Quantum Electronics, IEEE Journal of, 1967. **3**(10): p. 415-416.

57. Farrow, R.L., et al. *Numerical modeling of self-focusing beams in fiber amplifiers*. in *Fiber Lasers IV: Technology, Systems, and Applications*. 2007. San Jose, CA, USA: SPIE.

58. Knight, J.C., et al., *Photonic bandgap guidance in optical fibers.* Science, 1998. **282**(5393): p. 1476.

59. Cregan, R.F., et al., *Single-mode photonic band gap guidance of light in air.* Science, 1999. **285**(3): p. 1537.

60. Russell, P.S.J., *Photonic-Crystal Fibers.* Journal of Lightwave Technology, 2006. **24**(12): p. 4729-4748.

61. Argyros, A. and J. Pla, *Hollow-core polymer fibres with a kagome lattice: potential for transmission in the infrared.* Optics Express, 2007. **15**(12): p. 7713-7719.

62. Couny, F., F. Benabid, and P.S. Light, *Large-pitch kagome-structured hollow-core photonic crystal fiber.* Optics Letters, 2006. **31**(24): p. 3574-3576.

63. Luan, F., et al., *Femtosecond soliton pulse delivery at 800nm wavelength in hollow-core photonic bandgap fibers.* Optics Express, 2004. **12**(5): p. 835-840.

64. Oberthaler, M. and R.A. Hopfel, *Special narrowing of ultrashort laser pulses by self-phase modulation in optical fibers.* Applied Physics Letters, 1993. **63**(8): p. 1017-1019.

65. Ouzounov, D.G., et al., *Generation of Megawatt Optical Solitons in Hollow-Core Photonic Band-Gap Fibers.* Science, 2003. **301**: p. 1702-1704.

66. Matsuura, Y., et al., *Small-bore hollow waveguide for delivery of near singlemode IR laser radiation.* Electronics Letters, 1994. **30**(20): p. 1688.

67. Mohebbi, M., et al., *Silver-coated hollow-glass waveguide for applications at 800nm.* Applied Optics, 2002. **41**(33): p. 7031.

68. *http://www.polymicro.com/products/opticalfibers/products_opticalfibers_spec9.htm*.

69. Nubling, R.K. and J.A. Harrington, *Launch conditions and mode coupling in hollow-glass waveguides.* Optical Engineering, 1998. **37**(9): p. 2454.

70. Abe, S. and M. Miyagi, *Transmission and attenuation of vector modes in uniformly bent circular hollow waveguides for the infrared.* IEEE Trans. Micro. Th. Tech., 1992. **40**(5): p. 903.

71. Sopori, B. and W. Chang, *Low-loss Na-glass waveguides.* Quantum Electronics, IEEE Journal of, 1978. **14**(5): p. 323-325.

72. Liu, J., et al., *Directly writing of 1-to-N optical waveguide power splitters in fused silica glass using a femtosecond laser.* Optics Communications, 2005. **253**: p. 315-319.

73. Minoshima, K., et al., *Fabrication of coupled mode photonic devices in glass by nonlinear femtosecond laser materials processing.* Optics Express, 2002. **10**(15): p. 645-652.

74. Florea, C. and K.A. Winick, *Fabrication and Characterization of Photonic Devices Directly Written in Glass Using Femtosecond Laser Pulses.* Journal of Lightwave Technology, 2003. **21**(1): p. 246-253.

75. Yang, P., et al., *Direct-write embedded waveguides and integrated optics in bulk glass by femtosecond laser pulses.* Optical Engineering, 2005. **44**(5): p. 051104.

76. Szameit, A., et al., *Hexagonal waveguide arrays written with fs-laser pulses.* Applied Physics B, 2006. **82**: p. 507-512.

77. Zoubir, A., et al., *Femtosecond laser fabrication of tubular waveguides in poly(methyl methacrylate).* Opt. Lett., 2004. **29**(16): p. 1840-1842.

78. Cerullo, G., et al., *Femtosecond micromachining of symmetric waveguides at 1.5 mm by astigmatic beam focusing.* Optics Letters, 2002. **27**(21): p. 1938-1940.

79. Herman, P.R., et al. *Writing Buried Optical Waveguides: Contrasts in Ultrafast and Ultraviolet Lasers*. in *Proc. International Congress on Applications of Lasers and Electro-Optics (ICALEO)*. 2002. Scottsdale AZ.

80. Zhang, H., S.M. Eaton, and P.R. Herman, *Low-loss Type II waveguide writing in fused silica with single picosecond laser pulses.* Optics Express, 2006. **14**(11): p. 4826-4834.

81. Moh, K.J., et al., *Influence of diffraction by a rectangular aperture on the aspect ratio of femtosecond direct-write waveguides.* Optics Express, 2005. **13**(19): p. 7288-7297.

82. Seiji Sowa, W.W., Takayuki Tamaki, Junji Nishii, Kazuyoshi Itoh, *Symmetric waveguides in poly(methylmethacrylate) fabricated by femtosecond laser pulses.* Optics Express, 2006. **14**(1): p. 291-297.

83. Osellame, R., et al., *Femtosecond writing of active optical waveguides with astigmatically shaped beams.* J. Opt. Soc. Am. B, 2003. **20**(7): p. 1559-1567.

84. Siiman, L.A. and L.B. Glebov. *Color center generation in sodium-calcium silicate glass by nanosecond and femtosecond laser pulses*. in *Laser-Induced Damage in Optical Materials*. 2005: Proc. of SPIE.

85. Yang, P., et al., *Direct-write embedded waveguides and integrated optics in bulk glass by femtosecond laser pulses.* Optical Engineering, 2005. **44**(5): p. 051104-1.

86. Marshall, G.D., M. Ams, and M.J. Withford, *Direct laser written waveguide-Bragg gratings in bulk fused silica.* Opt. Lett., 2006. **31**(18): p. 2690-2691.

87. Homoelle, D., et al., *Infrared photosensitivity in silica glasses exposed to femtosecond laser pulses.* Optics Letters, 1999. **24**(18): p. 1311-1313.

88. Cheo, P.K., A. Liu, and G.G. King, *A high-brightness laser beam from a phase-locked multicore Yb-doped fiber laser array.* IEEE Photonics Technology Letters, 2001. **13**(5): p. 439-441.

89. Corning, I. (2003) *HPFS® Fused Silica Standard Grade Product Sheet*. **Volume**,

90. Taylor, R.S., et al., *Ultra-high resolution index of refraction profiles of femtosecond laser modified silica structures.* Optics Express, 2003. **11**(7): p. 775-781.

91. Raoa, S.V., et al., *Measurements of optical loss in GaAs/Al2O3 nonlinear waveguides in the infrared using femtosecond scattering technique.* Optics Communications, 2002. **213**: p. 223-228.

92. Irwin, B.S., et al. *Temporal effects of femtosecond to nanosecond laser ablation of fresh porcine liver*. in *BiOS 2004: Laser Int. Tiss. Cells XV*. 2004. San Jose, California: SPIE.

93. Higbee, R., et al. *Ultrafast pulsed lasers: surgical wave of the future?* in *BiOS 2004: Lasers Biophot. Vet. Med.* San Jose, California: SPIE.

APPENDIX

Appendix A

Derivation of the Scattering Matrix

The boundary conditions are applied at the core-cladding interface ($r = a$). Continuity of the E_z components requires that

$$E_z^i + E_z^s = E_z^c . \tag{A.1}$$

Expanding, (A.1) becomes

$$a_m^E J_m\left(k_2 r\right) + b_m^E H_m^{(1)}\left(k_2 r\right) = c_m^E J_m\left(k_1 r\right). \tag{A.2}$$

Similarly, continuity of the H_z components gives

$$H_z^i + H_z^s = H_z^c \tag{A.3}$$

which is expanded as

$$a_m^H J_m\left(k_2 r\right) + b_m^H H_m^{(1)}\left(k_2 r\right) = c_m^H J_m\left(k_1 r\right). \tag{A.4}$$

Combining (A.2) and (A.4), we obtain

$$\begin{bmatrix} \dfrac{J_m(k_2 r)}{J_m(k_1 r)} & 0 \\ 0 & \dfrac{J_m(k_2 r)}{J_m(k_1 r)} \end{bmatrix} \begin{bmatrix} a_m^E \\ a_m^H \end{bmatrix} + \begin{bmatrix} \dfrac{H_m^{(1)}(k_2 r)}{J_m(k_1 r)} & 0 \\ 0 & \dfrac{H_m^{(1)}(k_2 r)}{J_m(k_1 r)} \end{bmatrix} \begin{bmatrix} b_m^E \\ b_m^H \end{bmatrix} = \begin{bmatrix} c_m^E \\ c_m^H \end{bmatrix} \tag{A.5}$$

Equation (A.5) can be written in vector form as

$$\overline{\overline{A}}_1 \begin{bmatrix} a_m^E \\ a_m^H \end{bmatrix} + \overline{\overline{B}}_1 \begin{bmatrix} b_m^E \\ b_m^H \end{bmatrix} = \begin{bmatrix} c_m^E \\ c_m^H \end{bmatrix}. \tag{A.6}$$

The F_ϕ fields can be written as

$$E_\phi = \frac{j}{\chi_i^2}\left(\omega\mu \frac{\partial H_z}{\partial r} - \frac{\beta}{r}\frac{\partial E_z}{\partial \phi} \right) \tag{A.7}$$

and

$$H_\phi = \frac{j}{\chi_i^2}\left(\omega\varepsilon \frac{\partial E_z}{\partial r} + \frac{\beta}{r}\frac{\partial H_z}{\partial \phi} \right). \tag{A.8}$$

Continuity of E_ϕ components requires that

$$E_\phi^i + E_\phi^s = E_\phi^c. \tag{A.9}$$

Equation (A.9) is expanded as

$$\frac{j}{k_2^2}\left[a_m^H k_2 \omega\mu J_m^{'}\left(k_2 r\right)+j\frac{\beta}{r}ma_m^E J_m\left(k_2 r\right)\right]$$
$$+\frac{j}{k_2^2}\left[b_m^H k_2 \omega\mu H_m^{(1)'}\left(k_2 r\right)+j\frac{\beta}{r}mb_m^E H_m^{(1)}\left(k_2 r\right)\right] \qquad \text{(A.10)}$$
$$=\frac{j}{k_1^2}\left[c_m^H k_1 \omega\mu J_m^{'}\left(k_1 r\right)+j\frac{\beta}{r}mc_m^E J_m\left(k_2 r\right)\right]$$

where $'$ denotes the derivative with respect to the argument.

Similarly, for the H_ϕ components,

$$H_\phi^i + H_\phi^s = H_\phi^c \qquad \text{(A.11)}$$

which can be expanded as

$$\frac{j}{k_2^2}\left[a_m^E k_2 \omega\varepsilon_2 J_m^{'}\left(k_2 r\right)+j\frac{\beta}{r}ma_m^H J_m\left(k_2 r\right)\right]$$
$$+\frac{j}{k_2^2}\left[b_m^E k_2 \omega\varepsilon_2 H_m^{(1)'}\left(k_2 r\right)+j\frac{\beta}{r}mb_m^H H_m^{(1)}\left(k_2 r\right)\right] \qquad \text{(A.12)}$$
$$=\frac{j}{k_1^2}\left[c_m^E k_1 \omega\varepsilon_1 J_m^{'}\left(k_1 r\right)+j\frac{\beta}{r}mc_m^H J_m\left(k_1 r\right)\right]$$

Combining (A.10) and (A.12) we obtain

$$\begin{bmatrix} \frac{\omega\varepsilon_2}{k_2^2} J_m'(k_2 r) & \frac{j\beta m}{k_2^2 r} J_m(k_2 r) \\ \frac{j\beta m}{k_2^2 r} J_m(k_2 r) & \frac{\omega\mu}{k_2^2} J_m'(k_2 r) \end{bmatrix} \begin{bmatrix} a_m^E \\ a_m^H \end{bmatrix}$$
$$+ \begin{bmatrix} \frac{\omega\varepsilon_2}{k_2^2} H_m^{(1)'}(k_2 r) & \frac{j\beta m}{k_2^2 r} H_m^{(1)}(k_2 r) \\ \frac{j\beta m}{k_2^2 r} H_m^{(1)}(k_2 r) & \frac{\omega\mu}{k_2^2} H_m^{(1)'}(k_2 r) \end{bmatrix} \begin{bmatrix} b_m^E \\ b_m^H \end{bmatrix} \tag{A.13}$$
$$= \begin{bmatrix} \frac{\omega\varepsilon_1}{k_1^2} J_m'(k_1 r) & \frac{j\beta m}{k_1^2 r} J_m(k_1 r) \\ \frac{j\beta m}{k_1^2 r} J_m(k_1 r) & \frac{\omega\mu}{k_1^2} J_m'(k_1 r) \end{bmatrix} \begin{bmatrix} c_m^E \\ c_m^H \end{bmatrix}$$

Writing in vector form, (A.13) becomes

$$\overline{\overline{A}}_2 \begin{bmatrix} a_m^E \\ a_m^H \end{bmatrix} + \overline{\overline{B}}_2 \begin{bmatrix} b_m^E \\ b_m^H \end{bmatrix} = \overline{\overline{C}}_2 \begin{bmatrix} c_m^E \\ c_m^H \end{bmatrix}. \tag{A.14}$$

Now, writing

$$\bar{a} = \begin{bmatrix} a_m^E \\ a_m^H \end{bmatrix}, \quad \bar{b} = \begin{bmatrix} b_m^E \\ b_m^H \end{bmatrix}, \quad \bar{c} = \begin{bmatrix} c_m^E \\ c_m^H \end{bmatrix}$$

we combine (A.6) and (A.14) to obtain

$$\overline{\overline{A}}_2 \cdot \bar{a} + \overline{\overline{B}}_2 \cdot \bar{b} = \overline{\overline{C}}_2 \left(\overline{\overline{A}}_1 \cdot \bar{a} + \overline{\overline{B}}_1 \cdot \bar{b} \right). \tag{A.15}$$

Rearranging, we get

$$\bar{a} \left(\overline{\overline{A}}_2 - \overline{\overline{C}}_2 \cdot \overline{\overline{A}}_1 \right) = \bar{b} \left(\overline{\overline{B}}_1 \cdot \overline{\overline{C}}_2 - \overline{\overline{B}}_2 \right). \tag{A.16}$$

We rewrite (A.16) to obtain

$$\bar{a} \cdot \overline{\overline{S}}_1 = \bar{b} \cdot \overline{\overline{S}}_2 \tag{A.17}$$

Now, defining

$$\overline{\overline{S}} = \overline{\overline{S}}_2^{-1} \cdot \overline{\overline{S}}_1, \tag{A.18}$$

we arrive at a relationship between the incident and scattered field coefficients

$$\bar{b} = \overline{\overline{S}} \cdot \bar{a}. \tag{A.19}$$

VITA

Michael N. Nguyen

Candidate for the Degree of

Doctor of Philosophy

Dissertation: EVALUATION OF SPECIALTY FIBERS AND WAVEGUIDES FOR ULTRASHORT LASER PULSE PROPAGATION

Major Field: Photonics

Biographical:

Personal Data: Born in Clinton, OK on June 30, 1978; wife, Megan and son, William.

Education: Graduated from Comanche High School, Comanche, OK in May 1996; received Bachelor of Science degree in Electrical Engineering from Oklahoma State University, Stillwater, OK in December 2000; completed the requirements for the degree of Doctor of Philosophy in Photonics from Oklahoma State University, Stillwater, OK in May 2008.

Experience: Engineer, VaxDesign Corporation, Orlando, FL from June 2004 to present; Engineer, Sciperio Incorporated, Stillwater, OK from July 2000 to June 2004;

Professional Memberships: Institute of Electrical and Electronics Engineers (IEEE); Society of Photo Instrumentation Engineers (SPIE), Optical Society of America (OSA), IEEE Lasers and Electro-Optics Society (LEOS).

Name: Michael Nguyen Date of Degree: May 2008

Institution: Oklahoma State University Location: Stillwater, Oklahoma

Title of Study: EVALUATION OF SPECIALTY FIBERS AND WAVEGUIDES FOR ULTRASHORT LASER PULSE PROPAGATION

Pages in Study: 171 Candidate for the Degree of Doctor of Philosophy

Major Field: Photonics

Ultrashort pulse lasers have become invaluable tools in many areas of science and technology. Optical waveguide or fiber delivery of ultrashort pulses would benefit numerous applications that require remote location of the laser or for addressing areas of low accessibility such as minimally invasive surgical procedures, multiphoton excitation microscopy, laser micromachining and high bandwidth telecommunications. However, the extremely high peak power and bandwidth associated with ultrashort pulses are prohibitive for most conventional waveguides that guide light in solid dielectric cores, the main drawbacks being dispersion, nonlinear effects, and damage via optical breakdown. The purpose of this study is to investigate the significant obstacles involved with implementing optical waveguides or fibers capable of delivering ultrashort pulses.

In recent years, specialty fibers such as large mode-area (LMA) photonic crystal and photonic bandgap fibers have been developed, which exhibit remarkable properties such as single-mode guidance that is independent of core size and guidance in an air core respectively. In this thesis, two early prototypes of each of these fibers are investigated for their ability to deliver ultrashort pulses. Another specialty fiber, silver coated hollow silica waveguide, which was originally developed for delivery of infrared light from CO_2 and Er:YAG lasers is shown to be a good candidate for single-mode delivery of gigawatt peak power pulses with minimal pulse distortion.

Another potential fiber is comprised of multiple evanescently-coupled single-mode cores. This so-called multi-core fiber has demonstrated increased power handling in fiber lasers and amplifiers and was selected as a candidate for delivery of ultrashort pulses due to its scalable large mode-area and increased nonlinear threshold. A design for multi-core fibers is proposed that allows tailoring of the supermode distribution to obtain equal power distribution among all cores, thereby maximizing power handling. The design is analyzed numerically using a Scattering Matrix Method (SMM) and coupled-mode analysis. Experimental verification of the proposed supermode tailoring method is achieved with femtosecond pulse direct-written waveguide arrays in soda-lime glass and high-purity fused silica. Experimental results of direct-written waveguide arrays are in excellent agreement with SMM and coupled-mode simulations and verify the ability to tailor supermodes in these structures by controlling a single variable during fabrication.

ADVISER'S APPROVAL: _____